



UNIVERSITÀ  
DEGLI STUDI  
DI PADOVA

UNIVERSITA' DEGLI STUDI DI PADOVA

**Department of Industrial Engineering DII**

Master's Degree Course in Mechanical Engineering

*Numerical and Experimental analysis  
of the torsional and impact behaviour  
of the shell of a ski touring boot*

Thesis Supervisor: Prof. Nicola Petrone

Company Supervisor: Eng. Michele Botteon – Tecnica Group

Student: Stefano Giroto 1236443

Academic Year 2021/2022



## Abstract

At the production level, it is very important for a company to be able to numerically simulate the behaviour of a new product. This is because, once one has the geometric model of the part and knows the material with which it will be produced, it will already be possible to know its behaviour and identify any critical points, with the possibility of correcting them, proceeding by successive iterations, without having the need to always have to produce prototypes to test experimentally, with all the associated costs and time.

For this reason, this thesis carried out in collaboration with Tecnica Group focused on the numerical simulation of the behaviour of the shells of the Markab ski boot. In particular, the aim of this work is to numerically simulate the behaviour of the shells during torsion and impact tests and to carry out experimental tests in order to derive quantities to validate the simulations. The focus was on torsional behaviour because torsional stiffness is an important parameter describing the performance of ski boots, and on impact resistance because shells must pass a standard tip impact test for safety.

The thesis work was therefore structured as follows:

- 1) A brief introduction to explain what ski mountaineering and downhill skiing consist of and to introduce the Markab shell under study.
- 2) Correction of the CAD model of the shell, inserts and soles to obtain solid bodies.
- 3) Experimental torsion tests and analysis of the results obtained.
- 4) Numerical simulations of torsion and comparison of results obtained with experimental tests.
- 5) Experimental impact tests with an instrumented stem and analysis of the results obtained.
- 6) Characterisation of shell materials at low temperatures and high strain rates to then implement their properties in numerical impact simulations.



# Table of Contents

Chapter 1: Introduction .....	1
1.1 Ski touring and downhill skiing.....	1
1.1.1 Ski touring.....	1
1.1.2 Downhill skiing .....	2
1.2 Markab ski boots .....	3
1.3 Study objectives and thesis structure .....	4
Chapter 2: CAD Modelling .....	7
2.1 Import problems .....	7
2.1.1 IGES file format.....	7
2.1.2 STEP file format.....	8
2.1.3 STL file format .....	10
2.1.4 Rhino 3D Model file format.....	13
2.2 Modelling with Rhinoceros.....	14
2.2.1 Model correction .....	14
2.2.2 Introduction of functional elements into the model.....	20
2.2.3 Importing the boot shell model into Ansys SpaceClaim .....	22
2.2.4 Modelling of the anterior insert and its seat on the boot shell .....	23
2.2.5 Modelling of the posterior insert and its seat on the boot shell .....	24
2.2.6 Correction of sole models .....	25
2.2.7 Model correction process with Rhinoceros .....	26
Chapter 3: Experimental torsion bench tests.....	27
3.1 Torsion test bench.....	27
3.1.1 Pre-existing grips simulating ski bindings.....	27
3.1.2 Ski touring posterior grip .....	29
3.2 Torsion test bench.....	30
3.2.1 Data analysis with Matlab .....	31
3.2.2 Testing with hybrid ski bindings configuration .....	32

3.2.3 Testing with ski touring bindings configuration.....	37
3.2.4 Comparison of results for the two ski binding configurations.....	40
3.3 Conclusions .....	44
Chapter 4: Numerical simulations of shell torsion tests.....	47
4.1 Numerical simulations of shell torsion with hybrid ski binding configuration.....	47
4.1.1 Setting materials in Engineering data .....	47
4.1.2 Creating an assembly on Ansys SpaceClaim .....	49
4.1.3 Assembly management on Ansys Mechanical.....	52
4.1.4 Convergence of numerical simulation .....	55
4.1.5 Result of numerical torsion simulations.....	57
4.2 Numerical simulations of shell torsion with ski touring binding configuration .....	60
4.2.1 Creating an assembly on Ansys SpaceClaim .....	60
4.2.2 Assembly management on Ansys Mechanical.....	62
4.2.3 Convergence of numerical simulation .....	63
4.2.4 Result of numerical torsion simulations.....	64
4.2.5 Comments on the results of numerical torsion simulations .....	68
4.3 Torsion numerical simulations with updated elastic moduli .....	69
4.3.1 Company testing of material properties .....	69
4.3.2 Torsion numerical simulations with updated average elastic flexural moduli ....	71
4.3.3 Conclusions.....	73
Chapter 5: Shell tip impact test.....	77
5.1 Company standard for shell tip impact resistance .....	77
5.2 Instrumented impact tests on Fractovis.....	81
5.2.1 Instrumented stem.....	81
5.2.2 Shell breaking impact tests.....	84
5.2.3 Analysis of data from impact tests .....	87
5.2.3 Conclusions.....	94
Chapter 6: Introduction to numerical impact simulations.....	97
6.1 Characterisation of polymeric materials at high strain rates and low temperatures.	97

6.1.1 Charpy impact tests on specimens .....	97
6.1.2 Three-point bending tests at high strain rates .....	99
6.2 Static impact simulations .....	102
6.2.1 Assembly management on Rhinoceros .....	102
6.2.2 Static impact simulations on Ansys Workbench .....	103
6.2.2 Conclusions and future developments of the work .....	104
Appendix A: CAD drawings of torsion test bench grips .....	107
A.1 Grip simulating the anterior ski touring binding.....	107
A.2 Grip simulating the posterior downhill skiing binding .....	108
A.3 Grip simulating the posterior ski touring binding.....	110
Appendix B: Scripts used for data analysis with Matlab .....	113
B.1 Script for data analysis of torsion bench tests .....	113
B.2 Script for impact test data analysis.....	117
Appendix C: Influence of the steel front insert in the torsional stiffness of the shell obtained from numerical simulations .....	121
Appendix D: photos of shells broken during impact tests .....	123
Bibliografia.....	127





# Chapter 1: Introduction

This chapter will explain the differences between ski touring and downhill skiing and, consequently, the different bindings that are used to fasten the boots to the skis. Then the boot model, on the shell of which the work of this thesis is focused, will be presented and, finally, the objectives of this work and how the thesis was structured in the various chapters will be explained.

## 1.1 Ski touring and downhill skiing

To begin with, it will be explained what the disciplines of ski touring and downhill skiing consist of and the different ski bindings that are used.

### 1.1.1 Ski touring

Ski mountaineering refers to the practice of skiing off-piste, and therefore on untracked snow, which involves walking uphill on skis and then skiing downhill. For ascents, skins are attached to the bottom surface of the skis in order to have grip on the snow; in addition, the heel of the boot is released from the rear binding of the ski, and is therefore free to rise during the initial phase of strides, and the boot is equipped with a rear lever (*figure 1.1*) that allows the shell and cuff to be released to further increase comfort during walking. Once the ascent phase is complete, the skins are removed, the rear lever of the boot is closed to switch to skiing mode, and the heel of the boot is bound to the rear binding; these last two operations allow for greater rigidity of the boot-ski system, which allows for better control of the skis on the descent.



Figure 1.1: rear view of a ski touring boot [1]

The skis are fitted with Dynafit bindings, which use pins to bind the boot to the ski. Since the boot is made of polymer material, the shell contains a steel front insert (figure 1.2) and a steel rear insert (figure 1.1) that couple with the pins of the Dynafit bindings to make this coupling effective, rigid and durable.



Figure 1.2: side view of a ski touring boot [1]

As can be seen in figure 1.3, the front binding consists of two pins that insert into the seats provided by the front insert on either side of the toe of the boot. The rear binding (figure 1.4), on the other hand, consists of two pins that insert at the rear into the insert provided on the heel of the boot. When walking, the rear binding can be rotated in order to give support to the heel of the boot for ascents of a significant slope.



Figures 1.3-1.4: front and rear Dynafit ski touring bindings

### 1.1.2 Downhill skiing

Downhill skiing refers to all those disciplines that involve using ski lifts to make the ascent phase, and then skiing solely downhill, on slopes where the snow has been

groomed. Usually, the boots do not have rear levers to assist the walking phase without skis and the heel of the boot is always bound to the ski while skiing.

In this discipline, since only the downhill phase has to be performed, the boots are rigidly bound to the ski at the tip and heel, in order to have greater control of the skis during skiing, which, being performed on more compact snow and at higher speeds, involves greater loads than in ski touring.



Figure 1.5: bindings used in downhill skiing to fasten the boot to the ski

At the toe and heel areas where the boot is bound to the bindings, its thicknesses increase and there are no inserts.

## 1.2 Markab ski boots

In this thesis, the boot that was studied is Tecnica's Markab model, which is a hybrid boot that is used 60% for downhill skiing and 40% for ski touring. Consequently, this boot is equipped with both the necessary geometry to be bound to downhill ski bindings and the necessary inserts to bind it to ski touring bindings. In particular, the study will focus on the Markab boot shell, which is produced with the same geometry in three different materials:

- Laripur 6650 (*figure 1.6*): is a modified polyester based TPU by Coim Spa.
- Grilamid (*figure 1.7*): is a polyamide by EMS-GRIVORY.
- Elastollan (*figure 1.8*): is a thermoplastic polyether-polyurethane by BASF.



Figures 1.6-1.7-1.8: Markab shells in Laripur (purple), Grilamid (black) and Elastollan (green)

These three materials have different mechanical properties but, since the shell is produced by injection moulding, the same mould geometry is used for all three in order to reduce costs.

### 1.3 Study objectives and thesis structure

The aim of this thesis is to numerically simulate the behaviour of the Markab shell in torsion and impact tests, in the three different materials, and to validate these simulations by means of experimental tests.

Since no numerical simulations were ever carried out in the company, the only CAD models available of the shells were those used to produce the mould geometries for injection moulding. However, when trying to import these models into the software used for numerical simulations (Ansys Workbench), errors were detected that made it impossible to obtain a solid model of the shell. The first part of the work was therefore focused on correcting the CAD models of the shell, inserts and soles in Rhinoceros.

The first simulations that were carried out concerned the torsional behaviour of the shell because torsional stiffness is an important performance parameter for ski boots (the stiffer a boot is, the more quickly one is able to change direction and handle high loads from the skis). It is therefore important to be able to evaluate this parameter numerically for a new shell, because if the torsional stiffness obtained is not the desired one, it is possible to modify the geometry and perform new simulations until the desired value is obtained. The torsion tests involve simple loading conditions, but once the simulations have been validated, it will also be possible to apply the forces and moments measured on the track (using load cells placed between the boots and skis) to the shell, to see how it behaves in real conditions and what its critical points may be.

Then impact simulations will have to be carried out because before putting a new shell on the market, its impact resistance must be tested. So far, these tests are only carried out experimentally via a drop tower where an impactor hits the tip of the shell with an impact energy defined by the company standard. These are pass or fail tests whereby if a certain number of prototypes of the new shell withstand the fixed impact energy, the model is type-approved, otherwise it will be necessary

to modify the geometry by increasing the thickness. This means that if a new shell does not pass the test, the CAD model must be updated, the geometry of the injection moulding moulds must be changed, and new prototypes must be produced for testing. This procedure is very costly both in terms of time and cost, which is why the idea of numerically simulating these tests was born, in order to already have an estimate of the impact resistance of the new shell once we have the CAD model of the shell itself.

The thesis work is therefore divided into chapters in the following way:

- Chapter 2: presentation of the problems encountered when trying to import the CAD model of the shell into Ansys Workbench and how the errors in the model were corrected in Rhinoceros; Then the addition of further functional elements that were missing from the initial shell model, such as the insert seats, and the correction of the CAD models of boot inserts and soles will be exposed.
- Chapter 3: the experimental tests performed on the torsion test bench at the university laboratory will be described; then it will be explained what the test output data are and how they were analysed in order to derive the torsional stiffnesses of the shells.
- Chapter 4: numerical simulations of shell torsion are presented, explaining how the material properties were handled and how the analysis was set up in Ansys Workbench; the results obtained will then be displayed and compared with the torsional stiffnesses obtained from experimental tests.
- Chapter 5: the company's standard for the resistance to tip impacts of shells will be presented; then the tests performed with the instrumented stem will be exposed, trying to obtain as much information as possible from tests performed in the proximity of the impact energy that causes shells to break.
- Chapter 6: the tests that have been carried out to try to characterise the behaviour of shell materials at high strain rates and low temperatures are presented; then it will be explained how the work is to be continued by numerically simulating impact tests.



## Chapter 2: CAD Modelling

This chapter will present the problems encountered when importing the CAD model of the boot shell in Ansys Workbench and how these problems were resolved by correcting the model in Rhinoceros. Then the addition of further functional elements that were missing from the initial boot shell model, such as the insert seats, and the correction of the CAD models of boot inserts and soles will be exposed.

### 2.1 Import problems

Some attempts were made to export the boot shell model from Rhinoceros (the modelling software used in the company) in a format that allow it to be correctly imported into Ansys SpaceClaim (a solid modelling CAD software integrated In Ansys Workbench), but some problems were encountered in doing so. The file formats that have been used to export the model are IGES, STEP, STL and Rhino 3D Model.

#### 2.1.1 IGES file format

Importing the model into Ansys SpaceClaim, it consists of many separate shells, as can be seen in *figure 2.1*, and this is a problem because, in order to execute FEM analysis, a solid model is required.

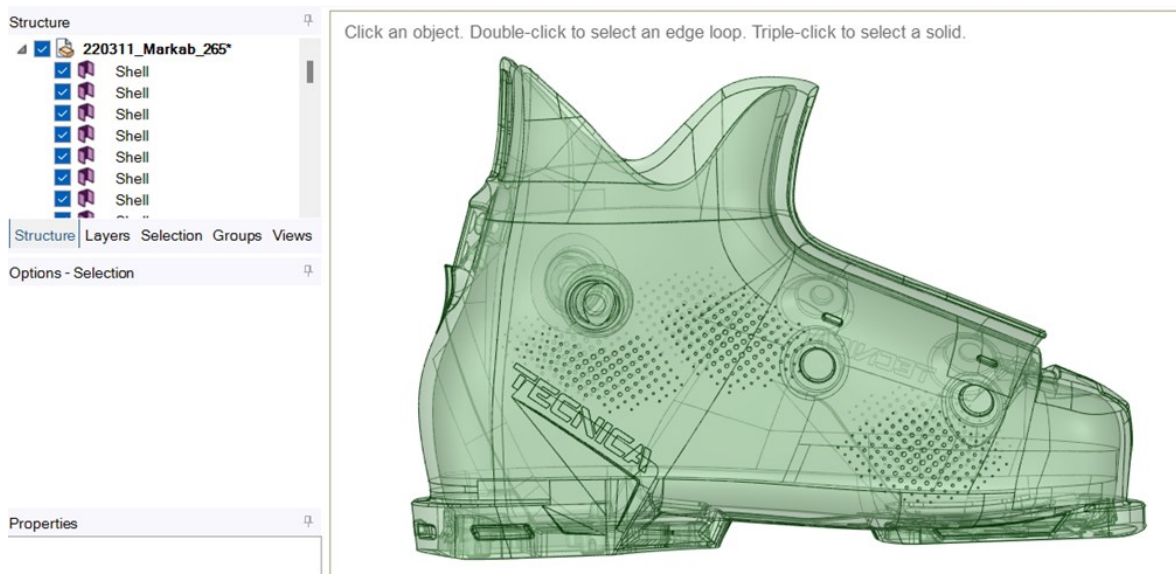


Figure 2.1: imported geometry of the boot shell in Ansys SpaceClaim from IGES file format

Using the 'Stitch' command (stitch surfaces into a single body), in the 'Repair' window, SpaceClaim manages to join several surfaces into a few surfaces, but fails to create a solid as can be seen from the ghosted display mode of the model in *figure 2.2*: the boot shell is semi-transparent and it is possible to see the inside and this means that we are still working with surfaces and not with a solid model.

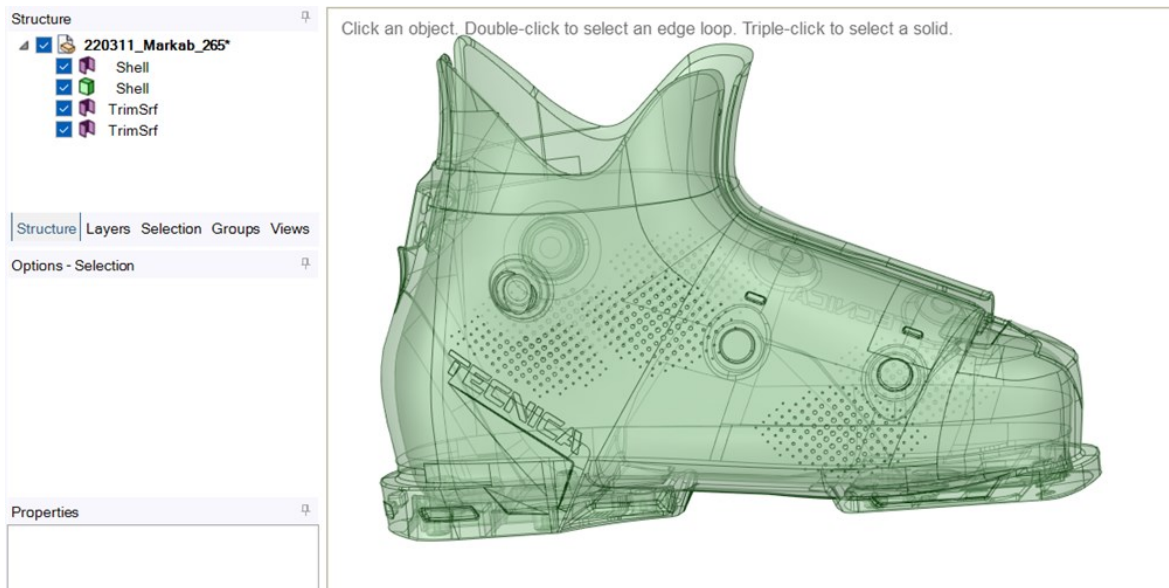


Figure 2.2: ghosted display mode of the boot shell and reduction of the number of surfaces which constitute the model with respect to the previous figure

We were unable to solve this problem, so a different file format was taken into account.

### 2.1.2 STEP file format

Importing the STEP file into SpaceClaim the model consists of two solids and a series of surfaces as can be seen in *figure 2.3*.

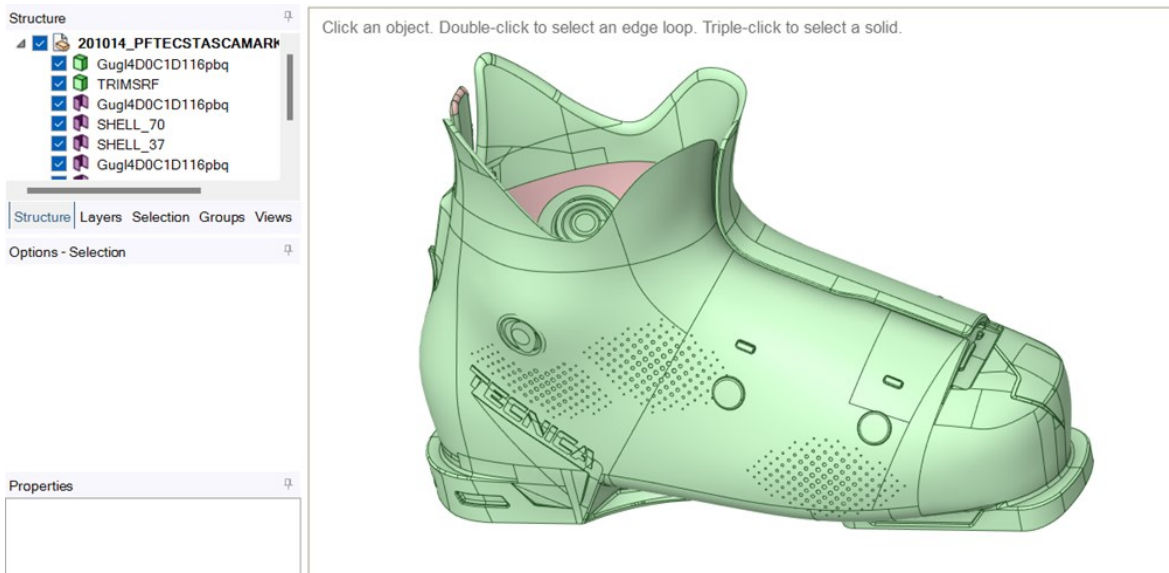


Figure 2.3: imported geometry of the boot shell in Ansys SpaceClaim from STEP file format

The first solid constitutes almost the entire geometry of the boot shell, while the second solid and the various subsequent surfaces relate to geometric details that can be neglected for the analysis we are interested in doing and therefore have been eliminated.



Passing this solid model to Ansys Mechanical (Ansys finite element solver) gives a warning: “Invalid face geometry was encountered that could not be successfully translated”. Trying to create the mesh results in a series of error messages and the mesh is then not generated:

- Error 1: “One or more entities failed to mesh. The mesh of the bodies containing these entities may not be up to date. However, meshing might be successful on the other entities”.
- Error 2: “A mesh could not be generated using the current meshing options and settings”.
- Error 3: “One or more surfaces cannot be meshed with acceptable quality. Try using a different element size or virtual topology”.

We then went back into SpaceClaim environment and tried to correct the surfaces that were indicated as problematic by Ansys Mechanical and to remove some surface elements that made mesh creation more complicated. The resulting geometry is shown in *figure 2.4*.



Figure 2.4: resulting geometry after the operations in Ansys SpaceClaim

Returning to the Mechanical environment with the new geometry results in warnings:

- Warning 1: “Invalid face geometry was encountered that could not be successfully translated”;
- Warning 2: “A body was processed that had faces with no facets. Mesh generation and mass property calculations may be impacted”.

Trying to generate the mesh we obtain the error “The mesh generation did not complete due to poor quality elements or incorreccted input. Please try meshing with

another mesh method or different mesh options". So, we were again unable to generate the mesh and we switched to another file format.

### 2.1.3 STL file format

In a STL file the surface of the boot shell is discretized into triangles; information on the geometry of the model then consists of the coordinates X, Y and Z of each of the three vertices of each triangle and a vector describing the orientation of the normal to the surface. Obviously, as a result of the discretization of the surface into triangles, the shell geometry in the STL file format is approximated to that of the CAD model (which we had with IGES and STEP file formats) [2].

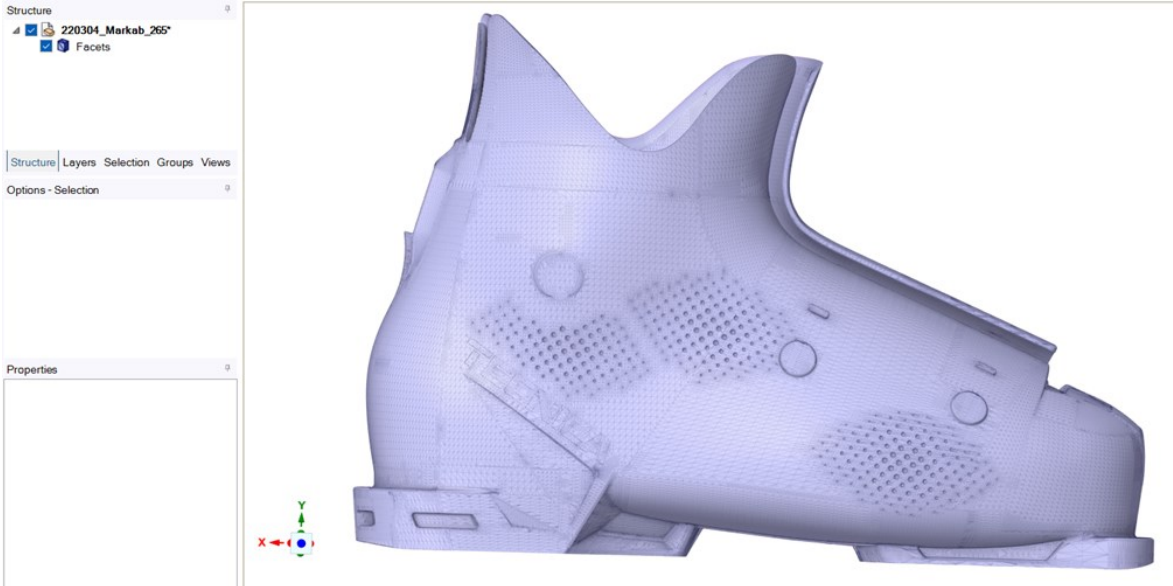


Figure 2.5: boot shell surface geometry discretized in triangles in STL file format

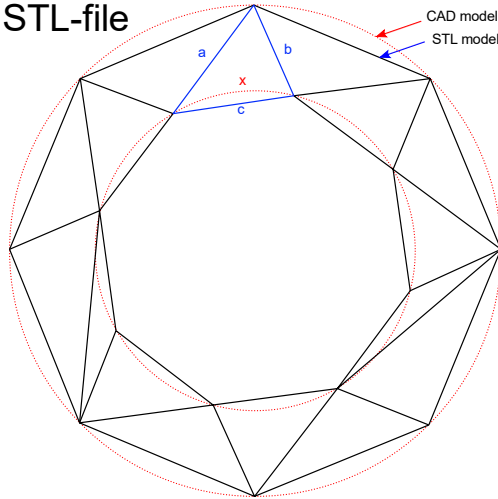


Figure 2.6: approximation introduced when switching from a CAD model to an STL model [3]

As can be seen in *figure 2.7*, the triangle mesh is denser close to geometric features of the boot shell.

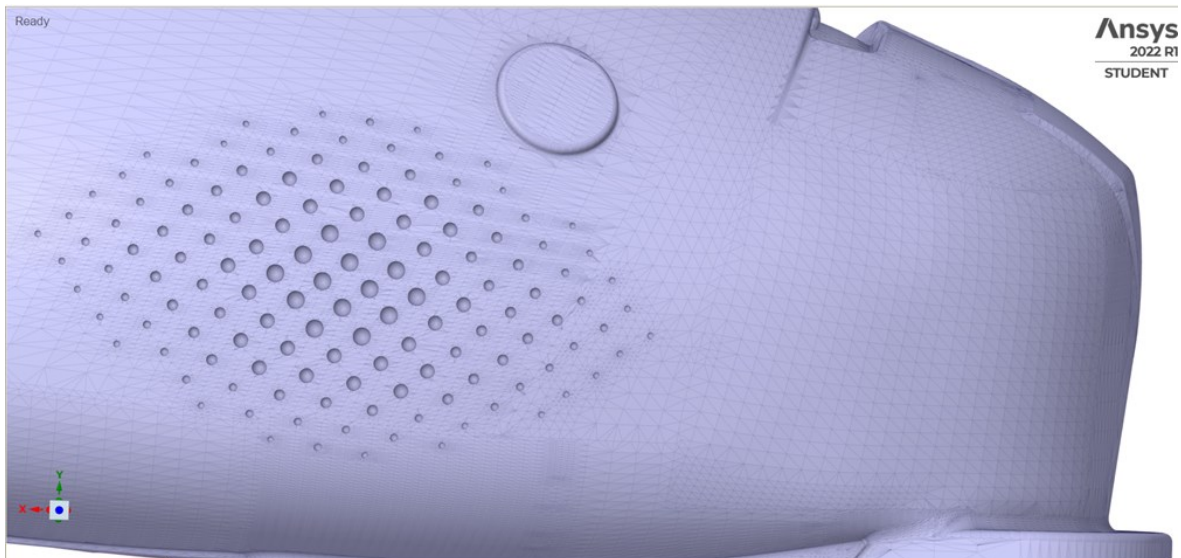


Figure 2.7: the mesh is denser near geometric features

As this initial geometric mesh will later become the structural mesh for FEM simulation in Ansys Mechanical, it is necessary to make it homogenous using the 'Shrinkwrap' command. The parameters of this command must be set appropriately in order to obtain a mesh that is not overly dense (which would make the model heavier and the elaboration of the structural solution longer), but also not excessively coarse (to avoid over-simplifications of the shell geometry, losing geometric features useful for applying constraints and loads). In particular, in this case, a size of 1,5 millimetres, an angle threshold of 20° and a secondary size of 3 millimetres were set and the result obtained is as presented in *figure 2.8*.

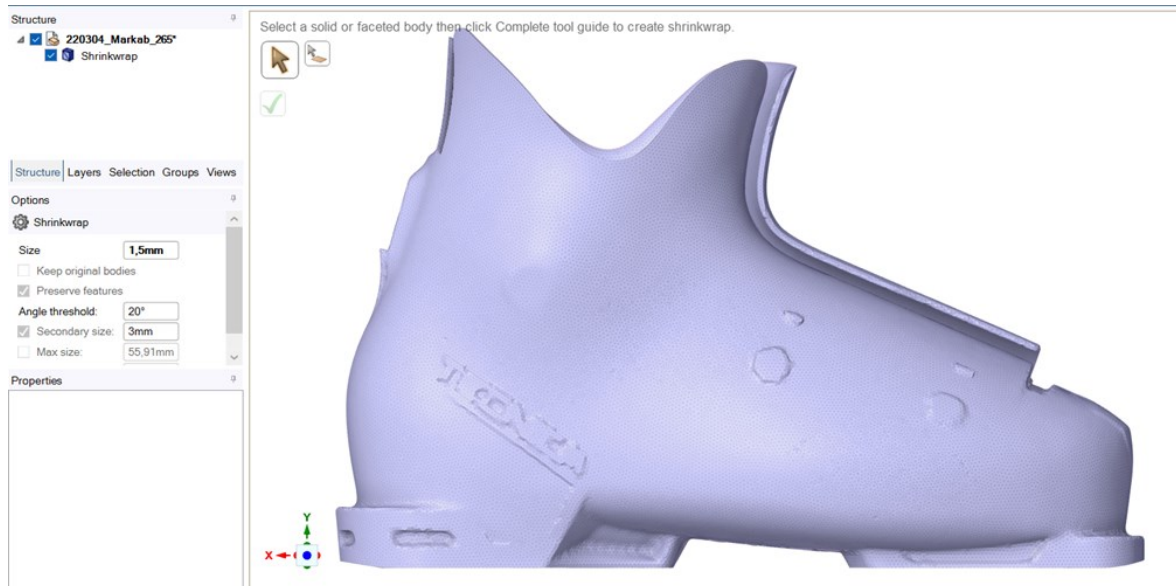


Figure 2.8: new mesh of the boot shell after the 'Shrinkwrap' command

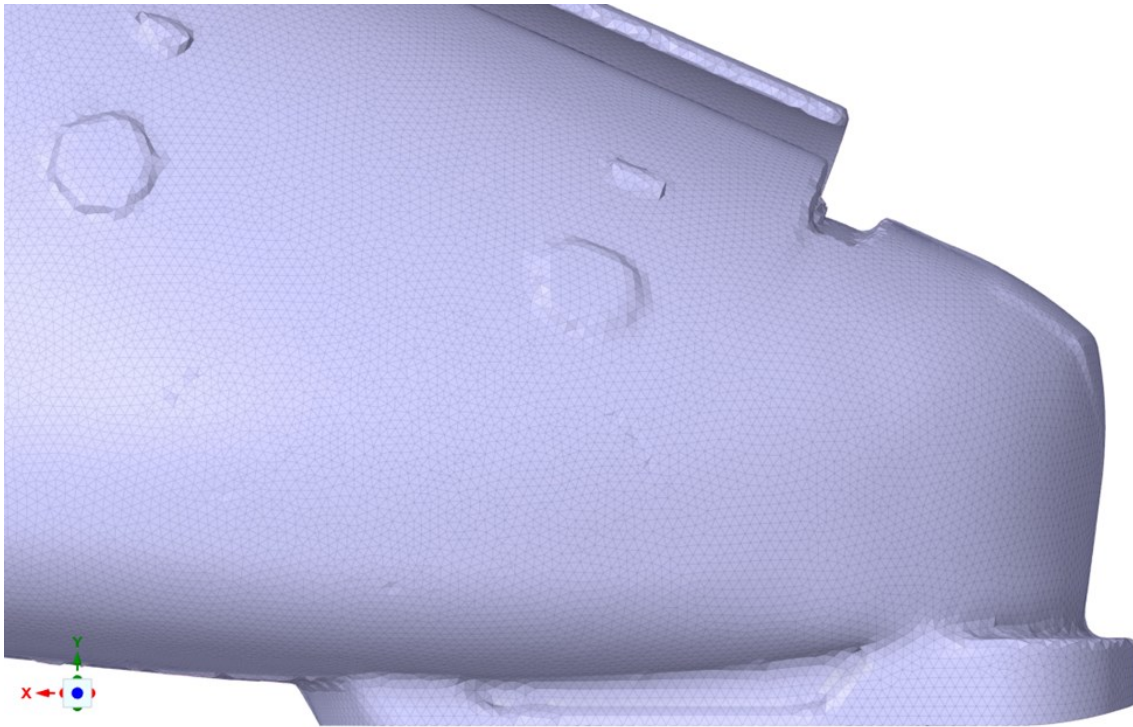


Figure 2.9: uniform mesh and simplified geometry of the boot shell after the shrinkwrap command

At this point, it is necessary to switch from a model describing only surfaces to a solid model (with a full thickness), using the 'Convert to solid' command. When executing this command, a message appears: "Converting a facets body can greatly increase the size of the model file. Are you sure you want to continue?" and clicking "Yes" the command is executed correctly. This conversion makes the model very heavy and takes about two hours.

By switching from the SpaceClaim environment to Ansys Mechanical, the structural mesh can be generated, but there are difficulties when it comes to applying constraints and loads: by having a mesh as the starting geometry, the definition of surfaces that was originally present in the CAD model was lost and consequently, to select the surfaces to be constrained, one must select all the faces of the mesh elements corresponding to the area of interest (*figure 2.10*); to select all these element faces the 'Select → Adjacent' command can be used.

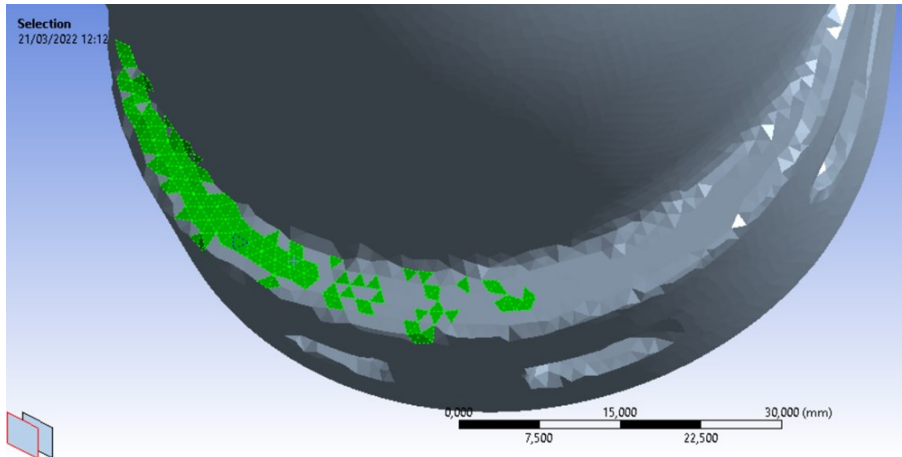


Figure 2.10: the definition of surfaces has been lost and all element faces must be selected to constrain the desired area

Using this file format, it is possible to create a structural mesh and perform a FEM simulation, but considerable processing time is required and, anyway, it is not possible to easily modify the geometry to add, for example, anterior and posterior inserts. This consideration led to the search for an alternative solution.

#### 2.1.4 Rhino 3D Model file format

Since SpaceClaim also allows the import of Rhino 3D Model format files, another possibility was to directly import the model in this format. Trying to import the original Rhino file of the boot shell results in 4133 separate bodies, as can be seen in *figure 2.11*.

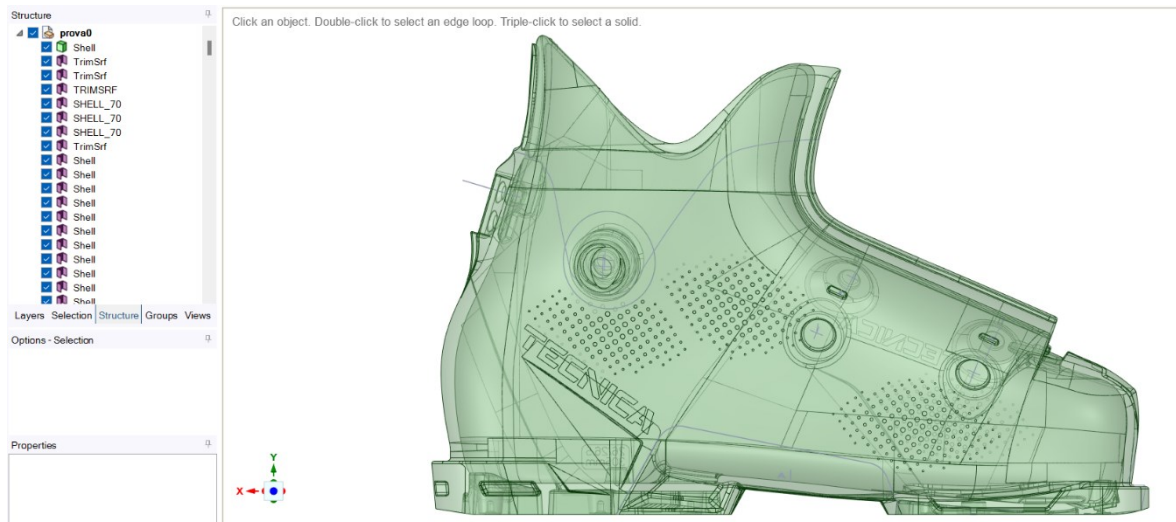


Figure 2.11: imported geometry of the boot shell in Ansys SpaceClaim from Rhino file format

An attempt can be made to merge these bodies using the 'Stitch' command again, but as a result of the operation, 8 separate bodies are obtained. Even using other *'Repair'* commands such as *'Missing Faces'* (detect and fix missing faces on a surface body), *'Gaps'* (detect and fix gaps in a surface body) and *'Extra Edges'*

(detect and remove edges that are not needed to define the shape of the model) we still cannot obtain a single solid body.

## 2.2 Modelling with Rhinoceros

Taking advantage of the possibility to import Rhino 3D Model files, I took a course on the use of Rhinoceros in order to correct the CAD model already within the programme used to design the boot shell and then import the model into SpaceClaim.

### 2.2.1 Model correction

Opening the Markab model with Rhinoceros shows that the boot shell consists of 4133 separate surfaces (*figure 2.12*); one must then select them all and try to merge them using the *'Join'* command: the result is a large polysurface representing most of the boot shell geometry, 11 surfaces and 14 other polysurfaces that Rhinoceros was unable to merge with the main polysurface. Then one can select the polysurface and, using the *'Gumball'* command, move it 500 millimetres in the X direction. This makes easier to select and eliminate all construction lines and surfaces that the software had failed to join to the main polysurface; then the polysurface can be returned to its initial location.

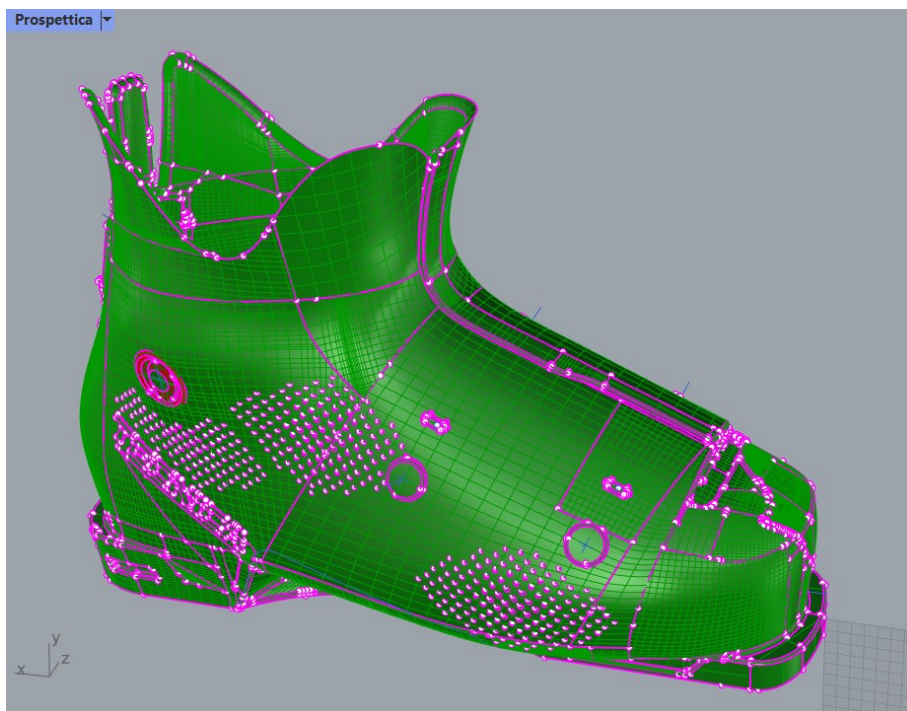


Figure 2.12: the original model consisted of 4133 separate surfaces

With the *'ShowEdges'* command, the 108 naked edges (*a surface, polysurface, or mesh edge that is not connected to another edge; solid objects have no naked edges [4]*) present can be highlighted in magenta (*figure 2.13*) and the model can then be corrected.

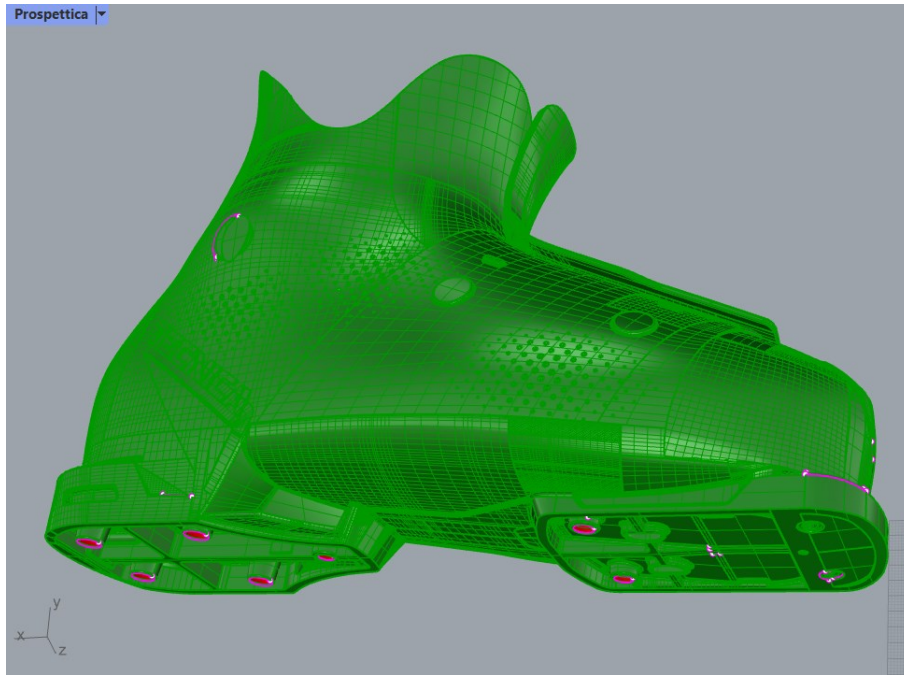


Figure 2.13: naked edges present in the polysurface

As surfaces were removed because they did not join the main polysurface, to begin the correction of the model, the polysurface can be selected and the **'Cap'** command used in order to fill all the planar holes. Where there are non-planar missing faces it is possible to close them with the **'NetworkSrf'** command (*creates a surface from a network of crossing curves [5]*) by selecting the edges of the surface to be created and choosing appropriate parameters (*figure 2.14*); specifically as **'Edge matching'** (*determines how the edges match the input geometry*) was chosen **'Position'** (G0 continuity) in order to achieve good continuity but, at the same time, not make the model too heavy. Once the surface has been created it is possible to use the **'Join'** command to merge it to the polysurface.

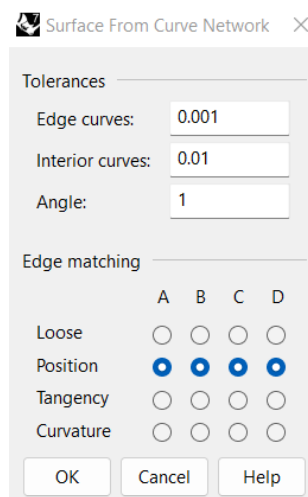
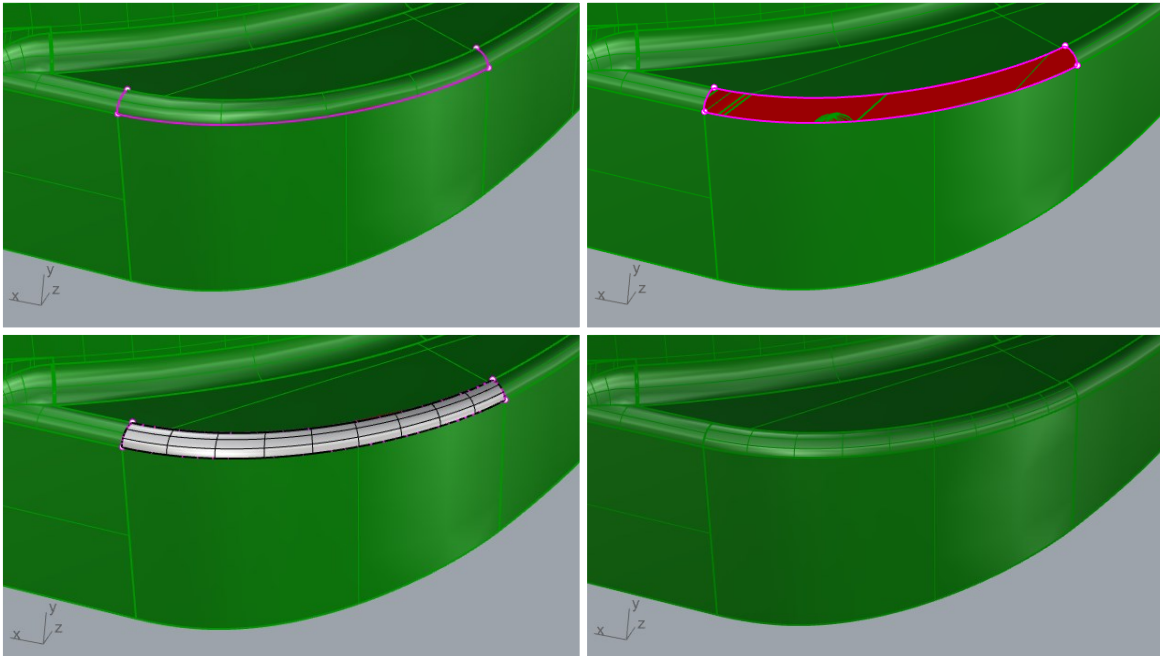


Figure 2.14: parameters selected for the **'NetworkSrf'** command

A first simple example of a problematic surface is presented in *figure 2.15*: a surface with three naked edges. Using the **'ExtractSrf'** command, the problematic surface is

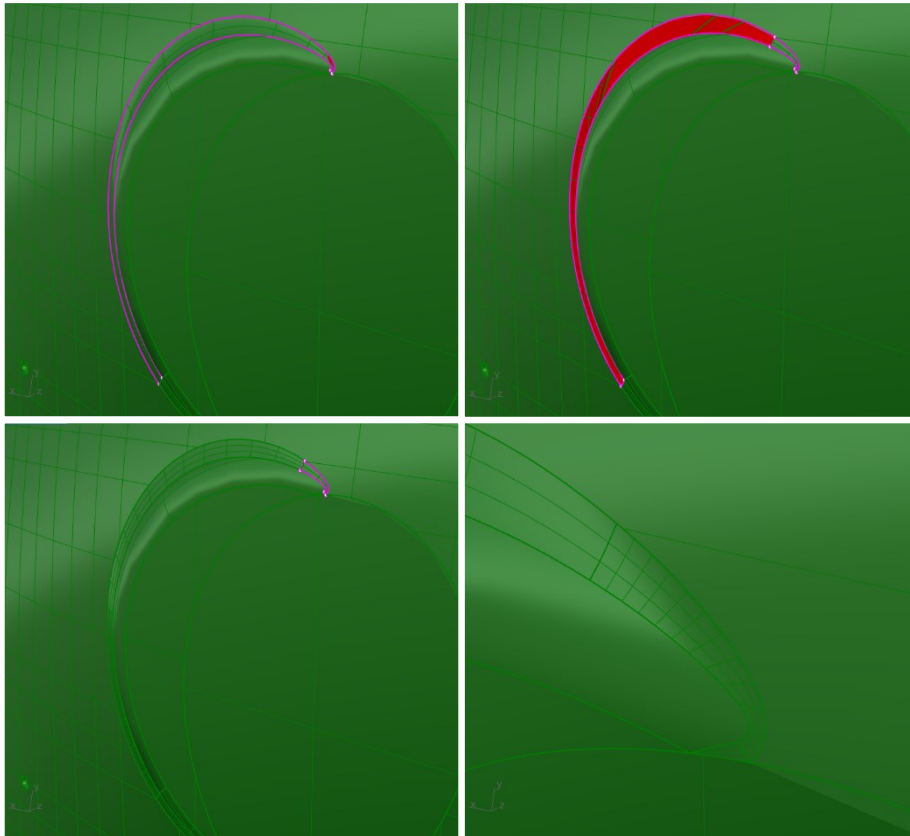
extracted from the polysurface (*figure 2.16*), then removed with the *'Delete'* command (*figure 2.17*), then create a new surface with *'NetworkSrf'* and use *'Join'* to merge it to the polysurface; as a result, there are no more naked edges (*figure 2.18*).



Figures 2.15-2.16-2.17-2.18: correction of a simple problematic surface by removing it and recreating it

A second example of problematic surface is presented in *figure 2.19*: a surface with two naked edges; in this case it is not possible to follow the previous procedure because after the final *'Join'* command, would still result in a surface with two naked edges. This problem may be related to the fact that the surface is very large and has a curvature that becomes more pronounced in the upper right end zone. What can be done is to extract the surface with the *'ExtractSrf'* command and then extract an isocurve near the upper right end zone with the *'ExtractIsocurve'* command (*creates curves that duplicate surface isoparametric curves at specified locations on the surface* [6]); in particular, for this case, the vertical direction (*'Direction=V'*) must be set to extract the isocurve as desired. The *'Split'* command is used to divide the surface with the isocurve just extracted and thus the larger of the two generated surfaces is eliminated (*figure 2.20*). Then with *'NetworkSrf'* and *'Join'* it is possible to recreate the larger surface, selecting its three edges and the extracted isocurve, and to join it to the polysurface (*figure 2.21*). Finally, the small surface is deleted, recreated and joined to the polysurface with the command already seen and so there are no more naked edges (*figure 2.22*).





Figures 2.19-2.20-2.21-2.22: correction of a problematic surface by splitting it in two surfaces and recreating them one at a time

In other cases, naked edges are present because two or more surfaces do not share the same vertex, as in the case of *figure 2.23*. After extracting the two surfaces, it can be seen (*figure 2.24*) that they have different vertices and that neither of them corresponds with the correct one and, consequently, both surfaces must be removed.

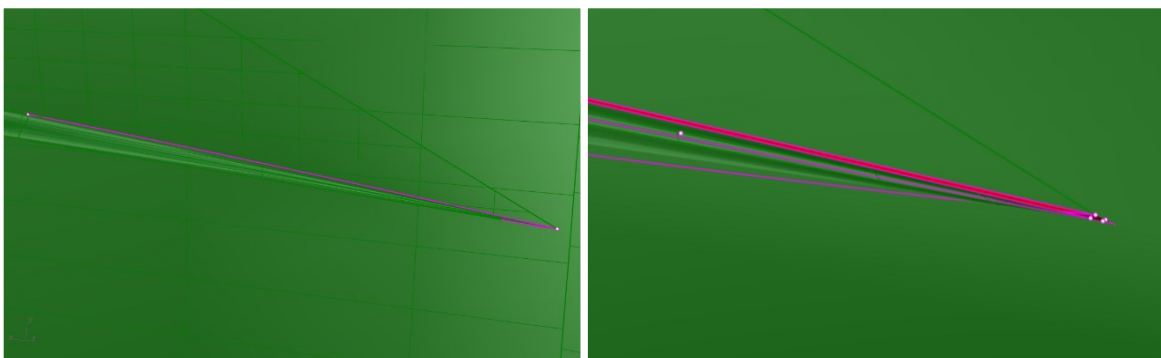
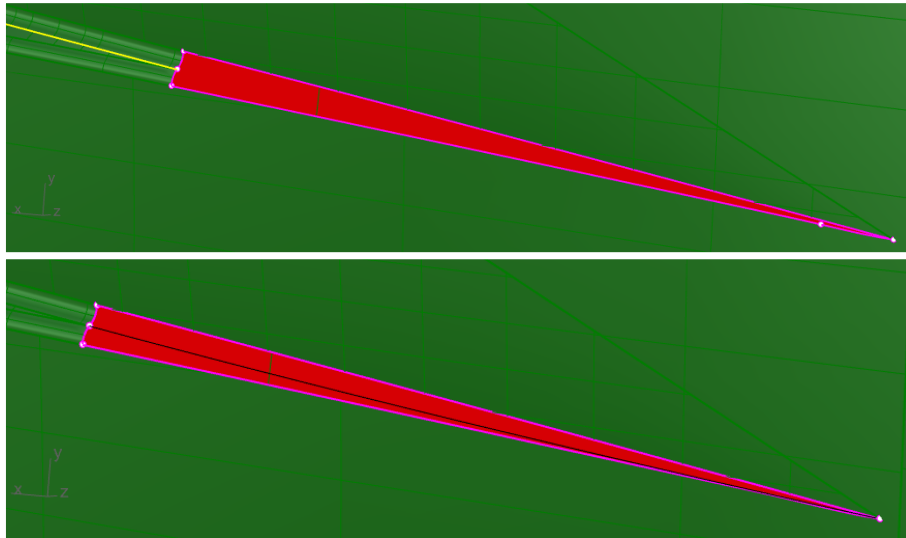


Figure 2.23-2.24: naked edges caused by surfaces with non-coincident vertices

At this point the surfaces are to be recreated but the edge that should separate them is missing; to create the curve that will form this border, the *'BlendCrv'* command can be used: the curve to be blended (yellow in *figure 2.25*) must be selected and then, acting on the commands settings, instead of selecting a second curve, a point corresponding to the vertex on the right is selected; as continuity of the curve with

the one on the left we choose 'tangency' (G1 continuity) and the curve is generated (figure 2.26).

Figure 2.25 shows that the lower naked edge is split in two by a point; before creating a new surface, these two edges must be joined with the 'MergeEdge' command (combines adjacent edges of the same simple surface into one edge) (figure 2.26). Then the two new surfaces can be created with 'NetworkSrf' and joined to the main polysurface.



Figures 2.25-2.26: creation of the border that will separate the two new surfaces to be created and unification of the lower naked edge

Going to the left side of the boot we can find a large red surface with a green piece (figure 2.27). According to the Rhino settings chosen, if a face is green it means that we are looking at the outer side of the surface, whereas if a face is red we are looking at the inner side of it; in this case, therefore, some error has occurred so that the surface is partly correctly oriented and partly not.

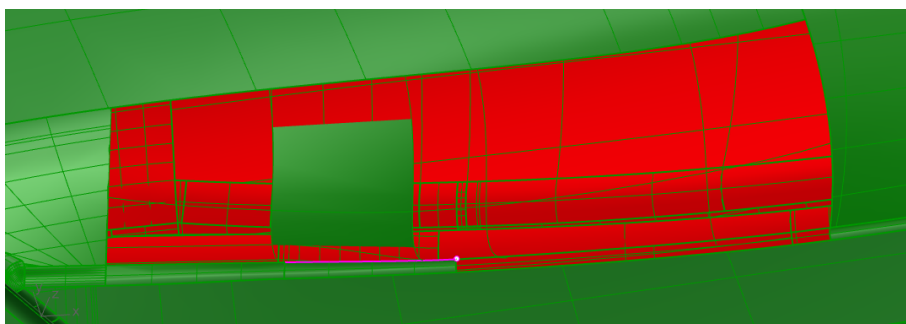


Figure 2.27: two incorrectly oriented surfaces

To solve this problem, the two problematic surfaces must be removed and recreated. To fix the bottom surface, simply reconstruct its top edge with 'BlendCrv' and then create the surface and join it to the polysurface. As can be seen in figure 2.28 in this case, a naked edge remains, which can be fixed using the 'JoinEdge' command and by selecting the two naked edges that should theoretically coincide

[7] (*figure 2.29*). So, it remains to recreate the upper surface; since this surface was very large and there are significant curvature variation in this area it is preferable to create several new surfaces using construction lines to ensure some continuity with the surrounding ones. To duplicate the two yellow edges in the bottom left-hand corner (*figure 2.28*) the command *'DupEdges'* (*creates curves from the selected surface or mesh edges*) can be used; to extract a curve in the centre of the newly created surface, one can use the *'ExtractIsocurve'* command and the *'Osnap'* tool set in *'Mid'* (*the object snaps constrain the marker to an exact location on an object such as the end of a line or the centre of a circle*). Then, using the *'ExtractIsocurve'* command and the *'Osnap'* tool set in *'End'*, three isocurves (in yellow in *figure 2.28*), corresponding to the three bottom curves just obtained, are extracted from the top surface.

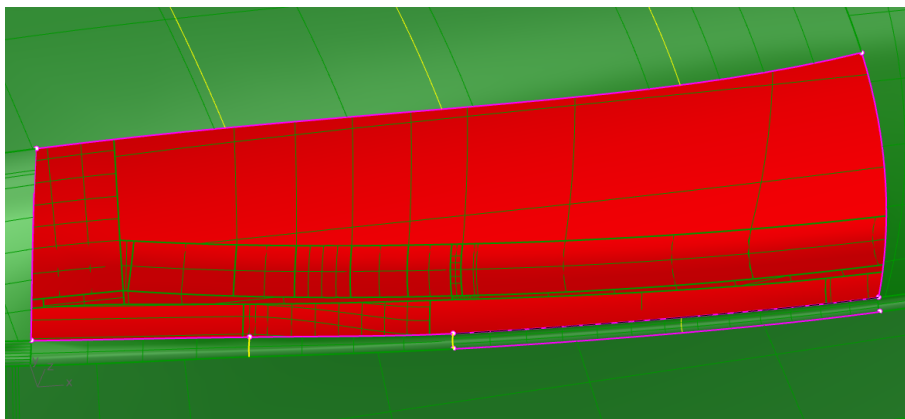


Figure 2.28: in red below we can see a naked edge that remained after the creation of the new surface; in yellow we can see the six curves that will be used to create the construction lines of the new surfaces

To create the construction lines for the new surfaces, the *'BlendCrv'* command is used and the yellow curves in *figure 2.28* are selected in pairs; this produces the three white curves in *figure 2.29* and the four new surfaces can then be created and joined to the main polysurface. In this way the surfaces are correctly oriented and there are no more naked edges (*figure 2.29*).

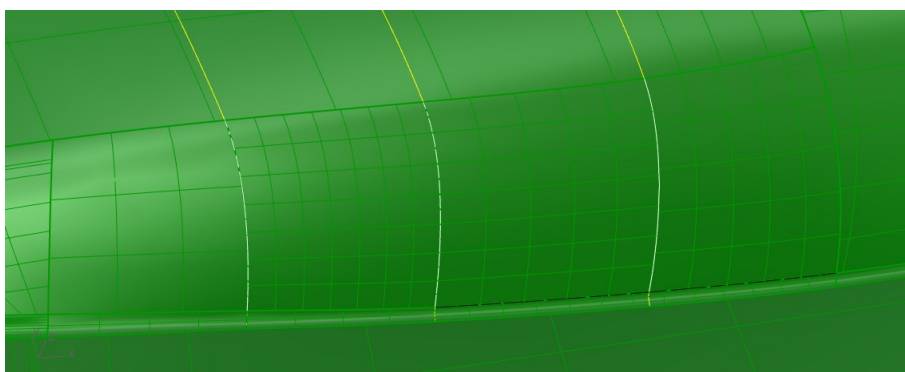


Figure 2.29: using the *'JoinEdge'* command the naked edge at the bottom in *figure 2.28* was fixed; four surfaces were created and joined correctly to the main polysurface

Sometimes, when building new surfaces and joining them to the polysurface, naked micro-edges are formed that can be removed with the *'RemoveAllNakedMicroEdges'* command (*removes very small single naked edges, which are edges that fold or loop back on themselves and have no matching edge to which they can be joined* [8]).

As mentioned above, when there are two naked edges close together, they can be removed with the *'JoinEdge'* command (*joins two naked edges that are out of tolerance* [7]). This command should be used with care because:

- When surfaces do not join that's an indication that more time should be spent on making the surfaces more accurate, in order to fix the gap, overlap or other problem between them.
- If the surface edges are not close to each other, you may have problems later on, depending on what you do with the model [7].

Once all naked edges have been eliminated using procedures similar or analogous to the examples above, by going to the *'Properties → Object'* window and selecting the boot shell geometry, in *'Type'* this will be classified as a *'closed solid polysurface'* and no longer as a *'open polysurface'* (figure 2.30).



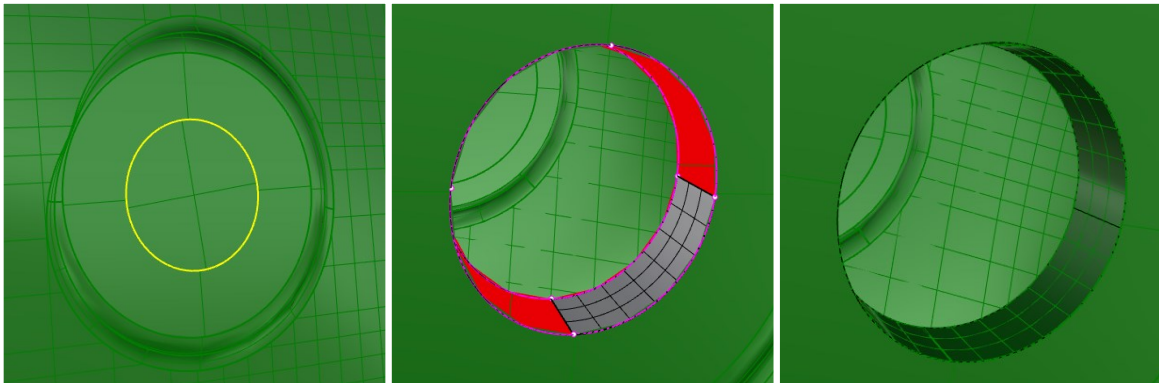
Figure 2.30: after correcting all the naked edges, the boot shell geometry results in a *'closed solid polysurface'*

Saving the model in Rhino 3D Model file format and importing it into SpaceClaim it is finally recognised as a solid body.

### 2.2.2 Introduction of functional elements into the model

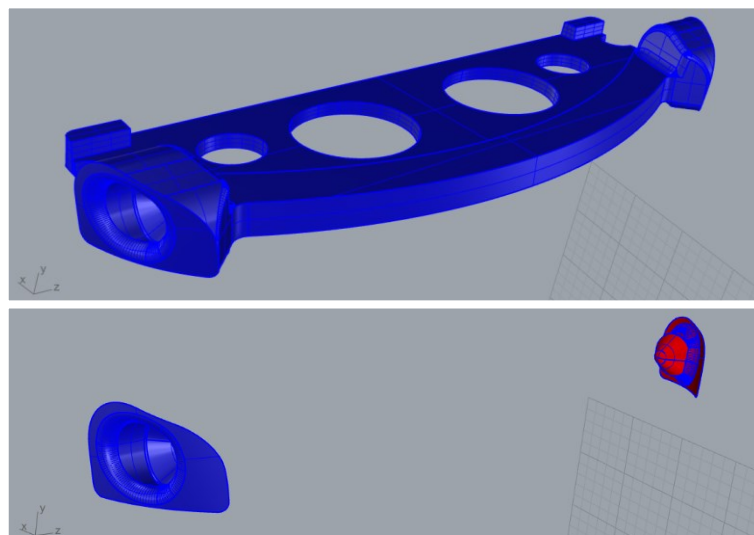
To perform FEM simulations of the ski boot's behaviour on the ski slope, the holes of the connection studs between shell and cuff and the mating seats of the anterior pins must be present in the model.

The stud holes are not present in the model but there are two 9 millimetres diameter circles (one for each stud) that can be used to create them (*figure 2.31*). To create the first stud hole, the surface within the circumference is extracted and then removed; therefore, use the *'Project'* command to project the circumference onto the corresponding inner surface of the boot shell and, at this point, using the *'Trim'* command, this projected circumference is used to open a hole on the inner surface. Then, using the *'Line'* command, we draw construction lines that will be used to create the through-hole surfaces (*figure 2.32*). Finally, we join these surfaces to the main polysurface and obtain the first stud hole (*figure 2.33*). To obtain the hole of the other stud, proceed in a similar way.



Figures 2.31-2.32-2.33: creation of a stud hole

For the creation of the anterior pin seats, the company provided the Rhinoceros model of the anterior insert (*figure 2.34*). For our purpose, we simply keep the outer surfaces of the insert and then eliminate all the rest of its geometry (*figure 2.35*).



Figures 2.34-2.35: anterior insert and surfaces that will be used to create the anterior pin seats

Returning to the boot shell model, the surfaces at the anterior pin seats are removed and we import the file containing the anterior pin seats. Using the *'Extract/socurve'* and *'BlendCrv'* commands, construction lines are drawn to create surfaces that

connect the geometry of the boot shell to that of the anterior pin seats as smoothly as possible. Then, using the *'MergeEdge'* and *'SplitEdge'* commands, we arrange what will be the edges of the new surfaces (figure 2.36). Finally, the new surfaces are created and joined to the rest of the model geometry.

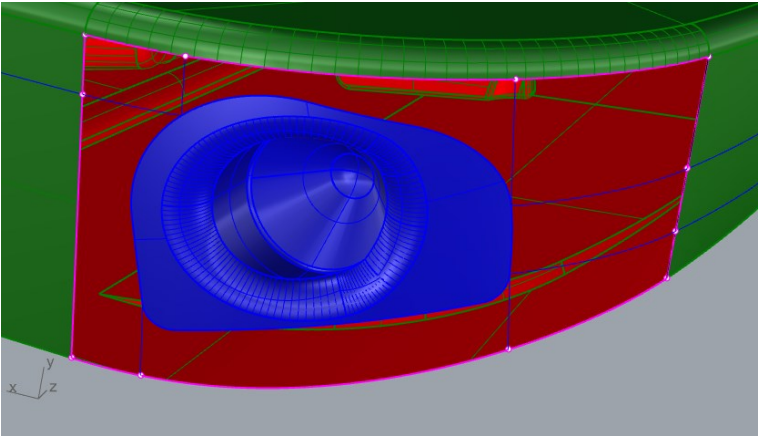
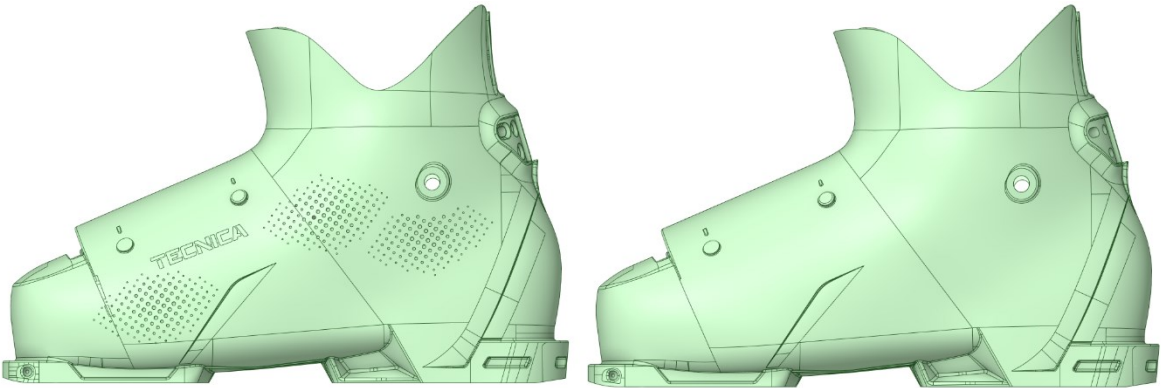


Figure 2.36: creation of the anterior pin seats

After making these changes, check that we still have a *'closed solid polysurface'* and save the new model.

### 2.2.3 Importing the boot shell model into Ansys SpaceClaim

After these functional elements have been added, the model is imported into Ansys SpaceClaim and some defeaturing operations can be performed on non-functional elements in order to make the subsequent meshing of the model easier (figure 2.37-2.38). In particular, the Tecnica logos on the sides and the CAS (*the Customer Adaptive System, which allows further customization of the shell to the shape of the foot to provide more comfort and better performance* [9]) have been eliminated using the *'Fill'* command in the *'Sketch'* window.



Figures 2.37-2.38: defeaturing operations performed in Ansys SpaceClaim with the *'Fill'* command

If this new model is transferred to Ansys Mechanical an *Information Message* appears saying: *'The following faces have high order NURBS surfaces. These may take longer than usual to mesh'* (figure 2.39). To show these faces, right-click on the message (in the *'Message'* window) and select *'Show problematic geometry'*. Once

the surfaces to be simplified have been identified, one goes back to Rhinoceros, deletes these surfaces and recreates them with the steps and the commands already explained above.

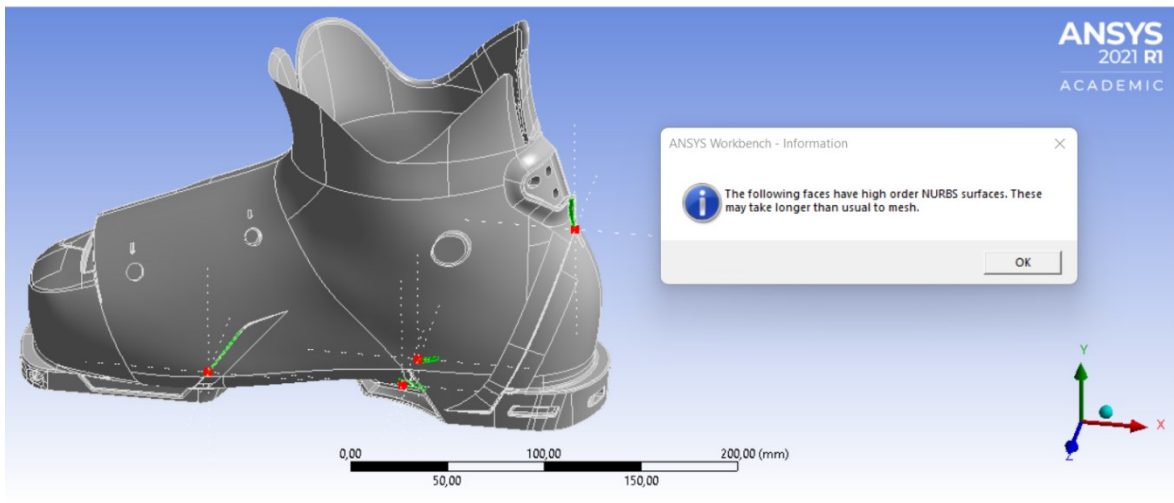


Figure 2.39: faces with high order NURBS surfaces

Then we have to repeat the defeaturing operation and, at this point, we obtain a model that does not give any warning or error messages in Ansys Mechanical and that can be meshed correctly and used to perform a FEM simulation.

#### 2.2.4 Modelling of the anterior insert and its seat on the boot shell

As mentioned in *paragraph 2.2.2*, to model the anterior pin seats, the company provided the geometry of the entire anterior insert. This made it possible to model the boot shell with an anterior cavity having exactly the shape of the insert to then build an assembly in SpaceClaim with boot shell and anterior insert; by managing the boot shell and insert as two separate bodies, it is possible to assign the correct material to each one and thus perform a more realistic FEM simulation. First of all, the anterior insert model must be opened in Rhinoceros and all naked edges must be highlighted and corrected, following a similar procedure to that set out for the boot shell in *paragraph 2.2.1*. Once this was done, we get a 'closed solid polysurface' model of the anterior insert.

To dig up the cavity in the boot shell we have to start from the anterior insert solid model, where we have to extract and delete the outer surfaces of the insert (*figure 2.35*), resulting in an open polysurface. Using the '*Flip*' command, we reverse the normal direction of the polysurface, obtaining the geometry of the boot shell cavity that houses the anterior insert (*figure 2.40*).

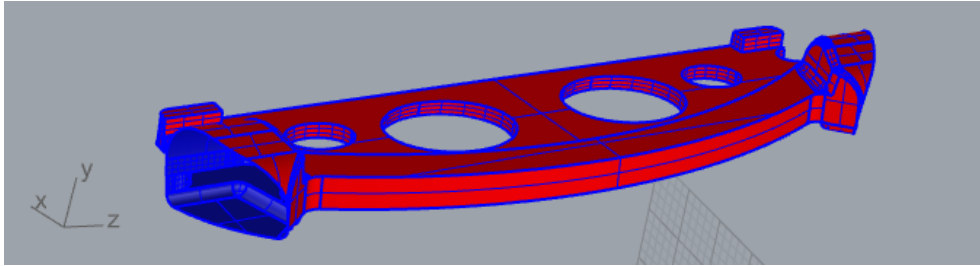


Figure 2.40: geometry of the boot shell cavity that houses the anterior insert

Then we proceed to the boot shell model with the anterior pin seats, obtained at the end of the 2.2.2 *paragraph*; the surfaces corresponding to the anterior pin seats (in blue in *figure 2.36*) must be extracted and removed, obtaining an open polysurface. Then the model of the internal cavity can be imported (*figure 2.41*) and joined to the polysurface of the boot shell, obtaining a ‘closed solid polysurface’ model.

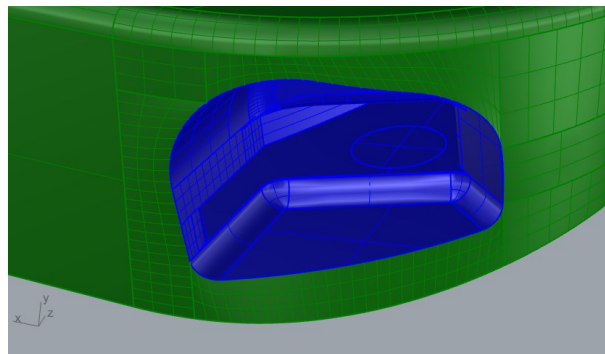


Figure 2.41: importing of anterior insert cavity geometry

### 2.2.5 Modelling of the posterior insert and its seat on the boot shell

With regard to the posterior insert, the company’s designer provided the model of the insert itself and the heel surface of the boot shell in that area (*figure 2.42*). After removing all naked edges from the insert geometry, its solid model was saved in a separate file so that it could then be imported into the SpaceClaim assembly with its material properties.

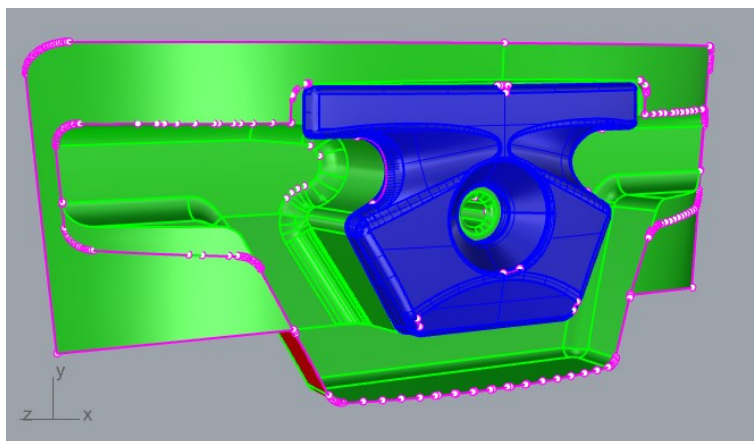
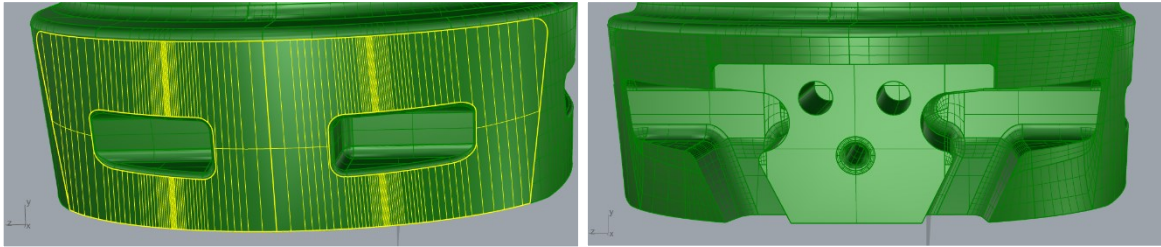


Figure 2.42: posterior insert and associated boot shell surface

With regard to the heel of the boot shell, the surfaces provided must be corrected and all naked edges removed. Then we have to open the boot shell model and



remove the corresponding old surfaces (*figure 2.43*), import the new ones and join them to the rest of the geometry, in order to obtain a closed model (*figure 2.44*).



Figures 2.43-2.44: updating of the heel geometry of the boot shell at the rear insert joint

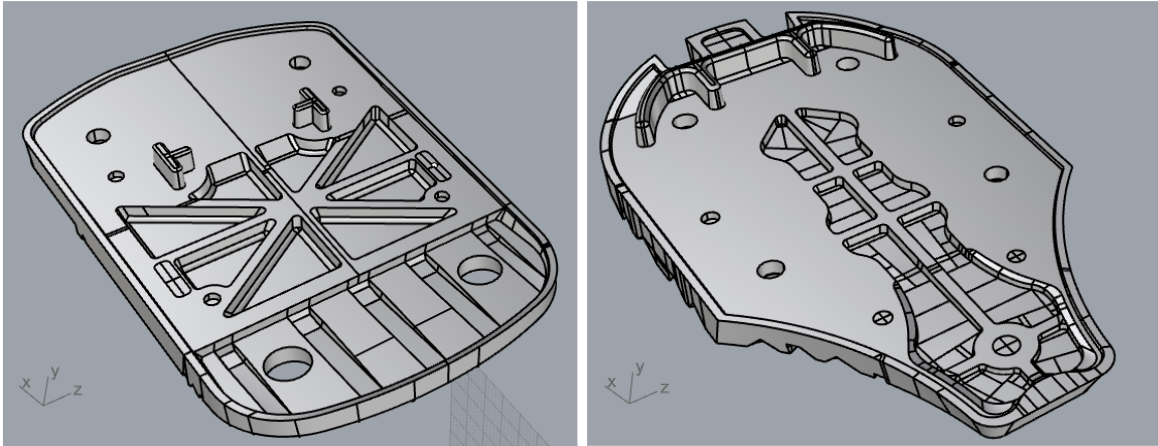
### 2.2.6 Correction of sole models

The company's designer also provided models of the boot shell soles; for each model, a correction process similar to that in *paragraph 2.2.1* was carried out, until closed models were obtained. Some simplifications of the geometries were also made on these models and, in particular, the intermediate surface separating the two different materials was removed. In fact, soles are made of two materials (*figures 2.45 and 2.46*) but the surface separating them had many missing surfaces and it would have been complicated to fix it.



Figures 2.45-2.46: the two different colours correspond to the two different materials of the soles

Given these problems and the fact that the two materials have similar mechanical properties, it was decided to make a simplification and consider the soles as consisting of a single material. As already seen in *paragraph 2.2.2* for the boot shell, also for soles when importing models into Ansys Mechanical, some faces with high order NURBS surfaces were reported and were therefore deleted and rebuilt on Rhinoceros. The final models are shown in *figures 2.47 and 2.48*.



Figures 2.47-2.48: corrected models of the boot soles

### 2.2.7 Model correction process with Rhinoceros

To conclude, when we want to correct a model with Rhinoceros, the process is as follows:

1. Using the 'ShowEdges' command, all naked edges in the model are highlighted.
2. If the surfaces that constitute the model are all separate, they are joined into a single polysurface with the 'Join' command; the surfaces that the software cannot join to the main polysurface are deleted with 'Delete'.
3. With the 'Cap' command, all flat holes can be closed and with 'NetworkSrf', all non-planar missing surfaces can be closed.
4. Problem surfaces are identified that lead to the presence of naked edges because there are gaps or overlaps with the edges of adjacent surfaces; these surfaces are extracted with 'ExtractSrf' and deleted with 'Delete'.
5. Construction lines for new surfaces are created using the 'ExtractIsocurve', 'DupEdges' and 'BlendCrv' commands; if there are edges to be joined, this can be done using the 'MergeEdge' command.
6. Using the 'NetworkSrf' command, new surfaces are created and joined to the main one with 'Join'.
7. With the commands 'JoinEdge' and 'RemoveAllNakedMicroEdges', any naked edges on the edges of the newly created surfaces are removed.
8. Once all naked edges have been corrected, a closed solid polysurface model is obtained.

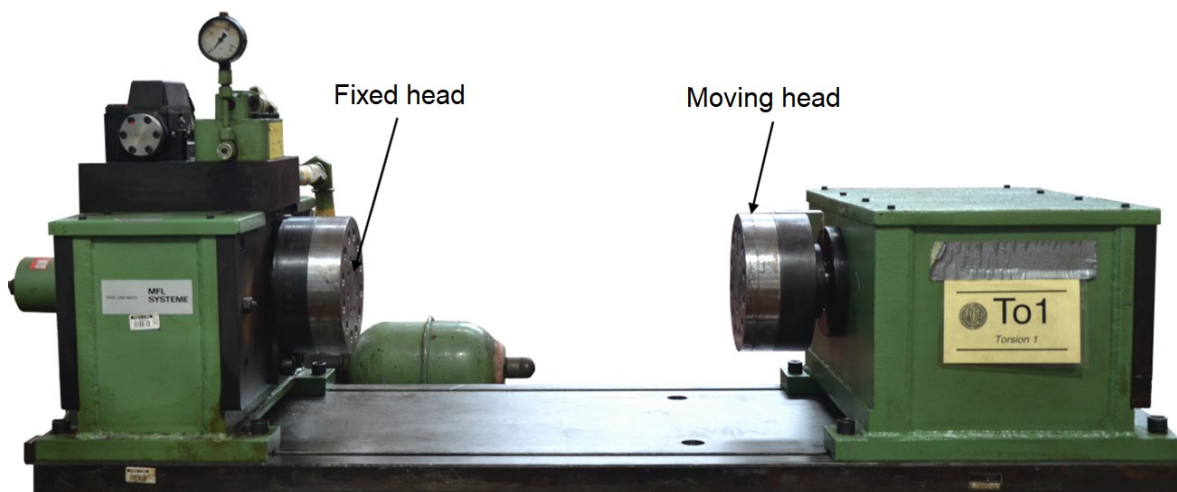
It took about two weeks of work to correct the shell model by introducing the functional elements that were missing, plus another week to correct the models of the soles and inserts.

## Chapter 3: Experimental torsion bench tests

This chapter will first present the test machine used to perform the torsion tests and the grips that were designed to simulate downhill and ski touring bindings. Then it will be explained how the torsion tests are performed, what the output file of the machine is and how it is processed through a Matlab script. Finally, the average hysteresis cycle, torsional stiffness and dissipated energies obtained for each test will be presented and compared.

### 3.1 Torsion test bench

The MFL torsional testing machine was used to perform torsional tests on the shells; the characteristics of this machine are a torsional load capability of 1100 *newton – metres*, a full rotation range of 120 *degrees* and a maximum test space of 2000 millimetres. The torsion machine consists of a fixed head and a moving head, which can be moved horizontally to adapt to the length of the part to be tested (*figure 3.1*).



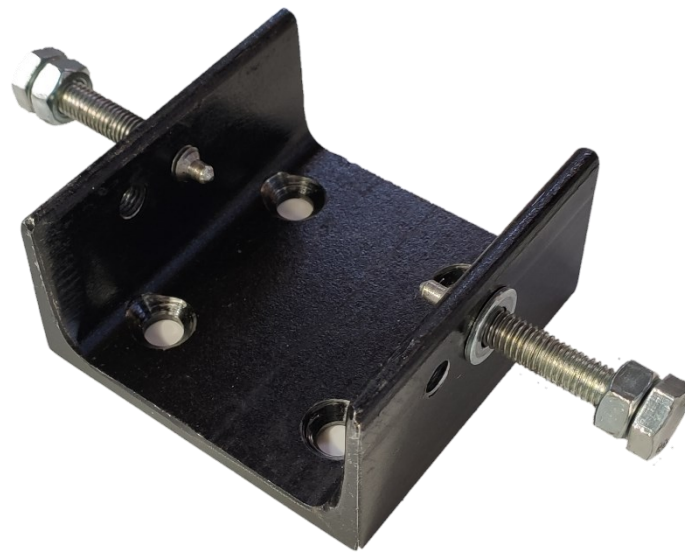
Figures 3.1: MFL torsional testing machine

The fixed head is the one that rotates and is equipped with an angle sensor, while the moving head does not rotate and is equipped with a load cell to obtain the torque applied to the component. The servo-hydraulics test bench is equipped with a master pc that allows the machine to be set up and, subsequently, controlled via the MTS station manager software. A torsion test can be performed in angle or torque control, and via the sensors, MTS software and servo-valve, it is checked that the real angle (or to the real torque) corresponds to the virtual angle (or to the real torque) set in the software.

#### 3.1.1 Pre-existing grips simulating ski bindings

Grips must be mounted on the heads of the torsion machine to simulate the anterior and posterior bindings with which ski boots are tied to skis. In an earlier work by Giuseppe Zullo (in which other Tecnica ski touring shells had been fatigue-tested)

two grips were designed: an anterior grip simulating a Dynafit ski touring connection and a posterior grip simulating a downhill skiing binding. The anterior grip was designed in Dynafit style, because the boots that were tested were ski touring boots, and it consists of a c-section beam on which four front and two side holes have been drilled: the first four were made in order to fasten the grip to the fixed head of the machine, while the last two serve to house the two screws simulating the anterior ski touring binding (*figure 3.2*).



Figures 3.2: grip simulating the anterior ski touring binding

To simulate Dynafit binding pins, the screw ends were machined on the lathe to obtain the geometry shown in the *figure 3.3*.



Figures 3.3: geometry of the screws used to simulate the anterior ski touring pins

CAD drawings of the ski touring anterior grip can be found in *appendix A.1*.

The posterior grip was designed in the style of downhill skiing to have a binding that constrains the shell more tightly, in order to obtain its mechanical fatigue properties. This grip consists of a c-beam section, on which the heel of the shell rests, welded to a vertical plate that is fixed to the machine moving head with three screws (*figure 3.4*).



Figure 3.4: welded structure consisting of the vertical plate and the c-beam

The c-section beam has two holes that allow the heel of the shell to be fixed with a plate (*figure 3.5*), which simulates the downhill ski binding required by the ISO 23223 standard. The parallelepiped welded to the rear end of the plate serves as a support and has been dimensioned in such a way as to keep the plate horizontal when the screws are tightened on the shell.



Figure 3.5: plate welded to a parallelepiped used to fasten the shell heel

CAD drawings of the posterior downhill ski grip can be found in *appendix A.2*.

### **3.1.2 Ski touring posterior grip**

In order to evaluate how the shell behaviour varies, a ski touring posterior grip was designed with Giuseppe and the students of group 7 of the 'Sports engineering and rehabilitation devices' course. This will make it possible to simulate the behaviour of the shell when bound with ski touring bindings and to evaluate how it varies compared to the case with the posterior downhill skiing binding. To realise this rear

constraint, an L-beam was used, which was fixed to the welded structure of the downhill skiing grip by means of two screws (*figure 3.6*).

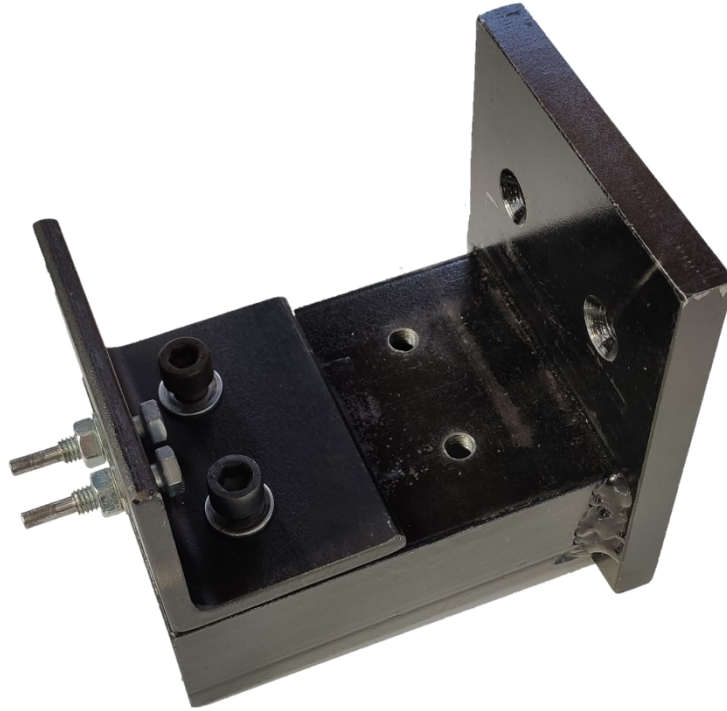


Figure 3.6: L-beam forming the posterior ski touring grip positioned above the welded structure of *figure 3.4* that will be fixed to the head of the torsion machine

Two M8 holes were drilled in the front plane of the L-beam to fasten two lathe-machined screws simulating Dynafit ski touring posterior bindings (*figure 3.7*).



Figure 3.7: geometry of the screws used to simulate the posterior ski touring pins

CAD drawings of the ski touring posterior grip can be found in *appendix A.3*.

### 3.2 Torsion test bench

The aim of our bench torsion tests is to determine the torsional stiffness of the shells by applying a known rotation and measuring the torque required to achieve that rotation. Specifically, the torsion machine was programmed to perform twenty cycles at a frequency of one hertz first between  $+5^\circ$  and  $-5^\circ$  and then between  $+10^\circ$  and  $-10^\circ$ . This type of test was performed for each of the three materials by first imposing the hybrid binding configuration (using the anterior ski touring grip and the posterior downhill ski grip) and then the ski touring configuration (using both ski touring grips). For each of the three materials a right shell was chosen from those provided and used for all tests, in order not to introduce possible variation in behaviour from one shell to another.

During the test, applied angles and torques are acquired at a frequency of 100 *hertz* and, at the end of the test, a DAT file is generated containing the acquired data in three columns: 'Time', 'MFLtorsion Angle' and 'MFLtorsion Torque'. These data were then processed with a Matlab script in order to obtain the torsional stiffness of the shell and the energy dissipated in an average cycle.

### **3.2.1 Data analysis with Matlab**

To analyse the DAT file generated by the torsion machine, a Matlab script was written, which can be found in *appendix B.1*. The script is divided into several sections:

- The first section serves to clean the environment: the command used delete all text from the 'Command Window', remove all variables from the 'Workspace' and close all open figure windows.
- The second section serves to set import options and to import data: it is indicated how data is to be imported, the column names and the type of variables they contain, and finally the data is imported into a table, which is then converted into a matrix.
- The third section serves to create an average vector of angles between the various cycles: first, an 'Angle' vector is created containing data for a certain integer number of load cycles, then the angles are corrected (because the initial position of the angle sensor has not been reset, but the rotation is set between  $+5^\circ$  and  $-5^\circ$  or  $+10^\circ$  and  $-10^\circ$ ) and finally a vector of angles is calculated for an average cycle.
- The fourth section serves to create an average vector of torques between the various cycles: a vector 'Torque' is created with all the values corresponding to those of the vector 'Angle' and then a vector of torques is calculated for an average cycle (in this case, no correction to the 'Torque' vector are necessary because the torque sensor was reset at the start of each test).
- The fifth section serves to create a graph of all the hysteresis cycles, which is useful for checking that the various cycles are overlapping and that no problems occurred during the test.
- The sixth section serves to analyse the average hysteresis cycle: the linear regression and the area of the mean hysteresis cycle are calculated and, finally, the graph of the mean hysteresis cycle and its regression line is created.
- In the seventh section, the output on the 'Command Window' is managed: the torsional stiffness of the shell, in the configuration considered, and the dissipated energy of the average hysteresis cycle are written. In particular,

torsional stiffness and dissipated energy are respectively the slope of the regression line and the area of the mean hysteresis cycle.

### 3.2.2 Testing with hybrid ski bindings configuration

The hybrid configuration of ski bindings was mounted on the torsion machine: the anterior touring ski grip and the posterior downhill ski grip. Then the movable head of the machine was shifted to fit the length of the shell and fixed to the base by means of four bolts. A Laripur shell was taken and fastened first on the front grip and then on the rear grip (*figure 3.8*).



Figure 3.8: Laripur shell mounted on hybrid ski binding configuration

After performing the test between  $+5^\circ$  and  $-5^\circ$  and analysing the output DAT file with the Matlab script, the graphs shown in *figures 3.9* and *3.10* are obtained.



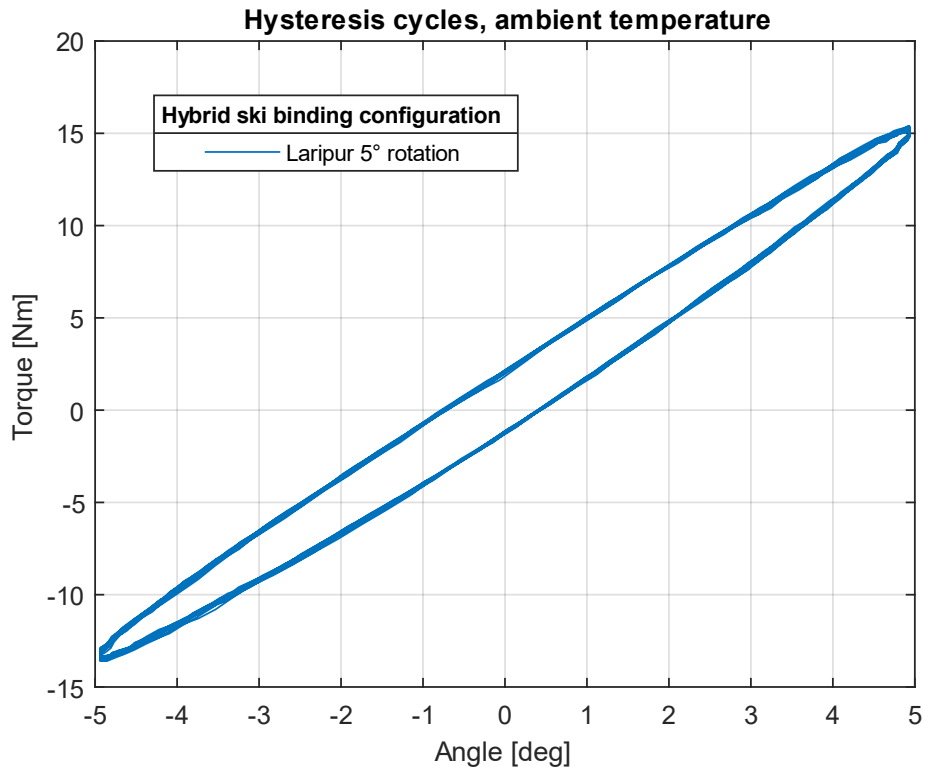


Figure 3.9: hysteresis cycles of the Laripur shell, imposing a rotation of five degrees clockwise and then anticlockwise, with the hybrid configuration of ski bindings, at ambient temperature

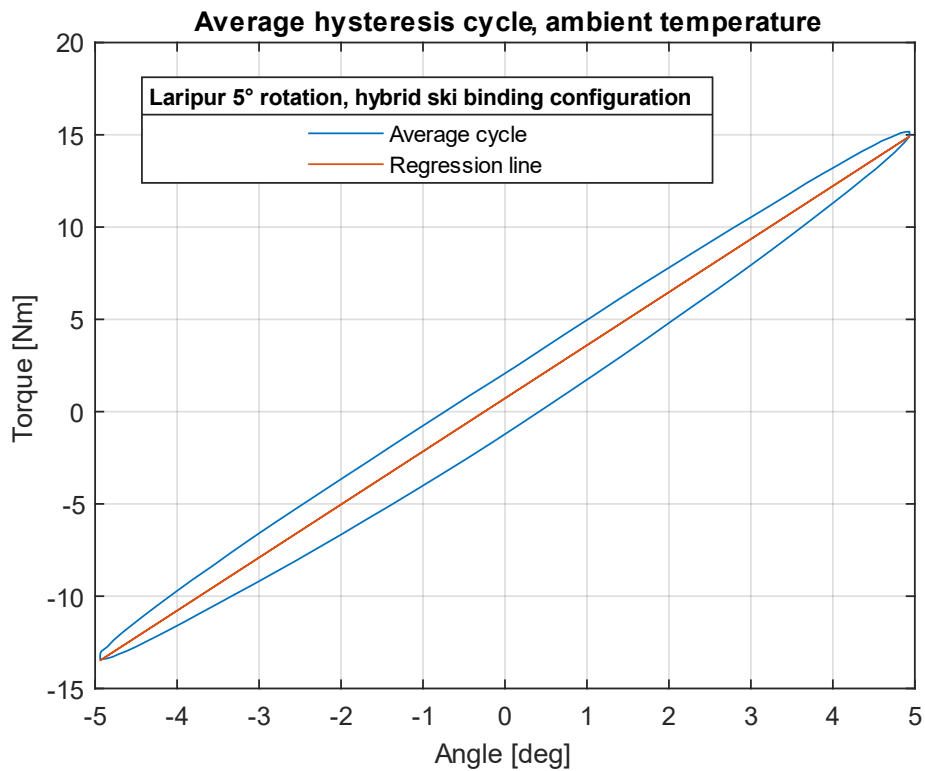


Figure 3.10: average hysteresis cycle and regression line of the Laripur shell, imposing a rotation of five degrees clockwise and then anticlockwise, with the hybrid configuration of ski bindings, at ambient temperature

On the 'Command Window' we can read that the torsional stiffness is  $2.8758 \text{ Nm/deg}$  and the energy dissipated in an average cycle is  $25.4751 \text{ J} \cdot \text{deg}$ .

Then, the test was performed by imposing ten degrees of rotation on the Laripur shell and a torsional stiffness of  $2.6695 \text{ Nm/deg}$  and an average cycle energy dissipation of  $110.6247 \text{ J} \cdot \text{deg}$  were obtained. The average hysteresis cycle graph with its regression line is shown in *figure 3.11*. Looking at the two graph (*figure 3.10* and *figure 3.11*) it can be seen that, with the change from five to ten degrees of rotation, the behaviour of the Laripur shell is less linear.

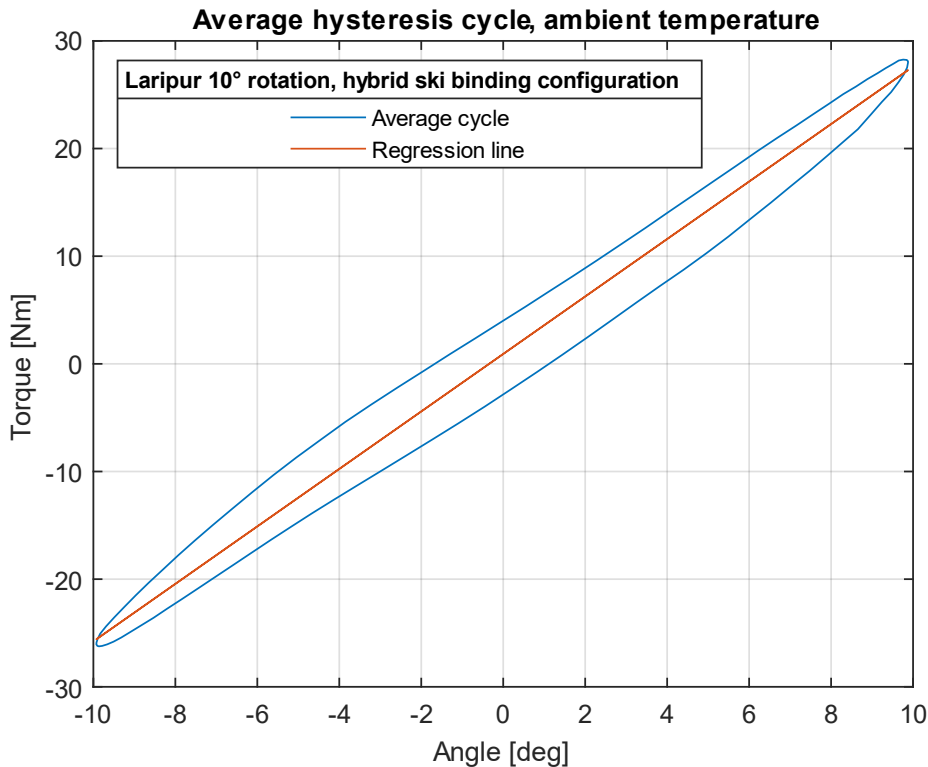


Figure 3.11: average hysteresis cycle and regression line of the Laripur shell, imposing a rotation of ten degrees clockwise and then anticlockwise, with the hybrid configuration of ski bindings, at ambient temperature

Subsequently, Grilamid and Elastollan shells were also tested and in *figures 3.12* and *3.13* we can see the comparison of the average hysteresis cycles obtained for five and ten degrees of rotation respectively. Henceforth in this paper, a concise nomenclature will be used in the graphs to identify the test conditions for each curve shown: 'ab-xyz-n', where the first two letters identify the shell material ('la'=Laripur, 'gr'=Grilamid, 'el'=Elastollan), the next three indicate the configuration of ski bindings applied ('hyb'=hybrid, 'tou'=touring) and the final number is the rotation imposed by the torsion machine, expressed in degrees (which can be of 5 or 10 degrees). Thus, for example, the test performed on the shell in Laripur, with the hybrid configuration of ski bindings and imposing a rotation of five degrees first clockwise and then anticlockwise, will be identified as: 'la-hyb-5'.

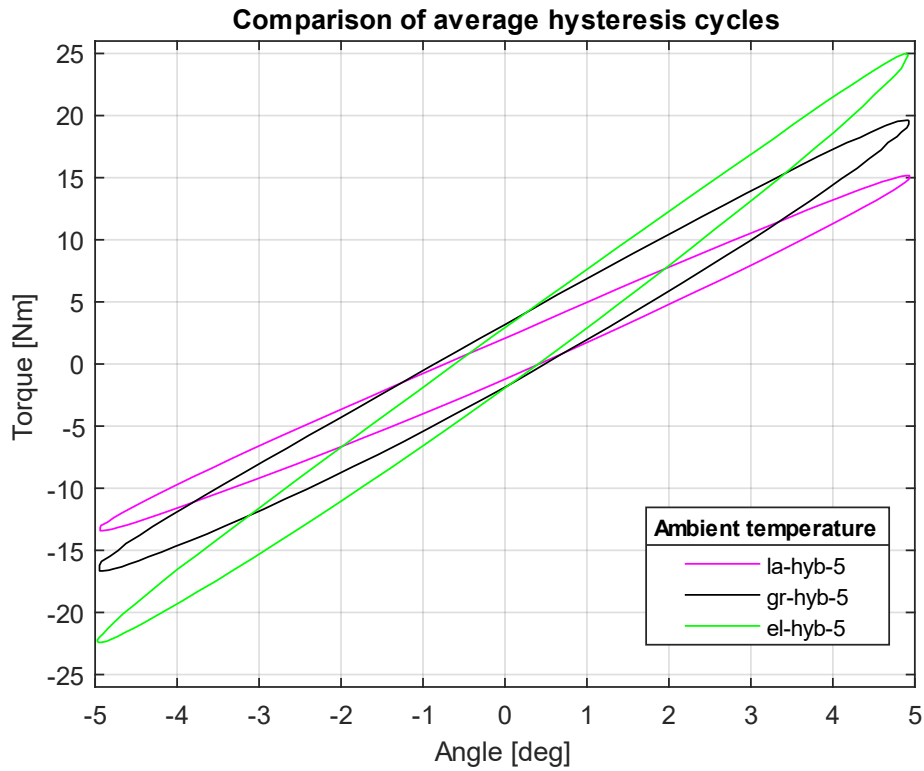


Figure 3.12: comparison of the average hysteresis cycles of Laripur, Grilamid and Elastollan shells, imposing a rotation of five degrees, with the hybrid of ski bindings configuration

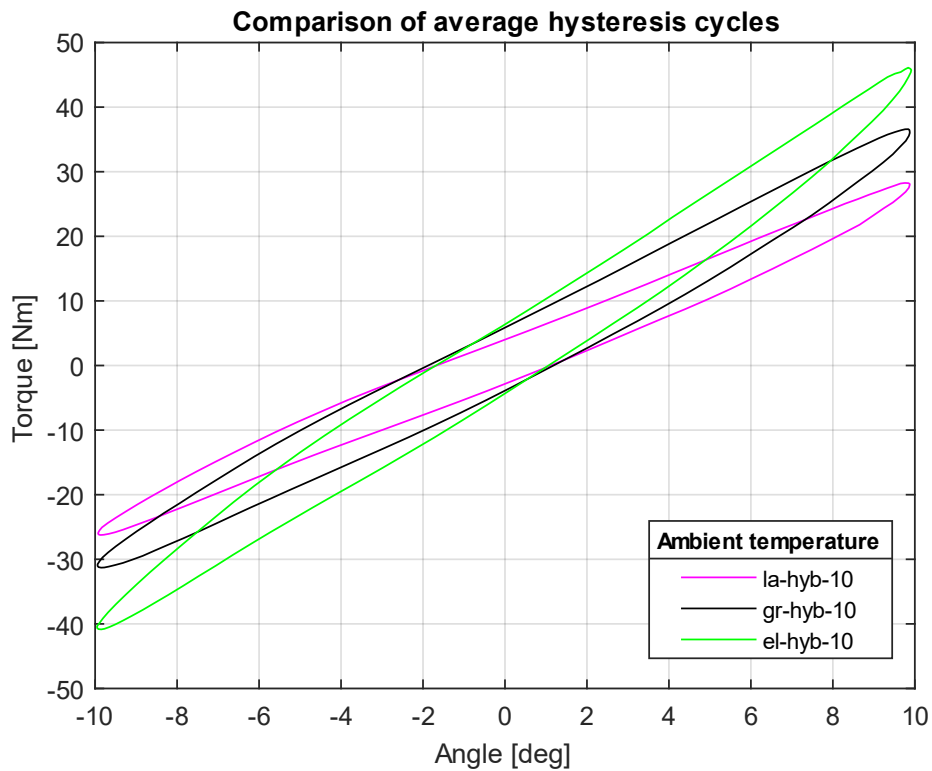


Figure 3.13: comparison of the average hysteresis cycles of Laripur, Grilamid and Elastollan shells, imposing a rotation of ten degrees, with the hybrid of ski bindings configuration

For each test, torsional stiffness ( $k_{hyb}$ ) is calculated as the slope of the regression line of the average hysteresis cycle, while the energy dissipated ( $E [J \cdot deg]$ ) is calculated as the area of the average hysteresis cycles. In order to have a comparison quantity between tests performed with different imposed rotations, the normalised dissipated energy is calculated by dividing the dissipated energy by the imposed rotation range  $\Delta\theta$  in degrees ( $\Delta\theta = 10^\circ$  for an imposed rotation of  $5^\circ$  rotation, while  $\Delta\theta = 20^\circ$  for an imposed rotation of  $10^\circ$  rotation).

$$\text{Normalized dissipated energy (N.E.)} = \frac{E}{\Delta\theta} [J] \quad \text{Formula (3.1)}$$

Table 3.1 shows the torsional stiffness and the normalised dissipated energy obtained for each test. For both the torsional stiffness and normalized dissipated energy, a column with the ratio to the Laripur shell test, with an imposed rotation of five degrees, is also shown, allowing a quicker understanding of the data.

$$\text{Ratio (Laripur } 5^\circ) = \frac{k}{k_{la-5^\circ}} \quad \text{Formula (3.2)}$$

Hybrid ski binding configuration, ambient temperature						
Material	Rotation	Peak Torque	Torsional stiffness		Normalized dissipated energy	
		Measured	Measured	Ratio (Laripur 5°)	Measured	Ratio (Laripur 5°)
Laripur	5	15,171	2,876	1	2,548	1
	10	28,261	2,670	0,93	5,531	2,17
Grilamid	5	19,629	3,658	1,27	3,823	1,50
	10	36,588	3,349	1,16	7,732	3,03
Elastollan	5	24,975	4,772	1,66	3,706	1,45
	10	46,107	4,255	1,48	8,680	3,41
	deg	Nm	Nm/deg		J	

Table 3.1: torsional stiffness and normalized dissipated energy obtained for each test with the hybrid ski binding configuration, at ambient temperature

It can already be deduced from figures 3.12 and 3.13 that Laripur is the softest material and Elastollan is the most rigid, as the torsional stiffness of the shells will be higher the greater the slope of the average hysteresis cycle. This is confirmed by the data analysis shown in table 3.1 where, for an imposed rotation of five degrees, it can be observed that: the Laripur shell stiffness is the lowest, the Grilamid shell stiffness is intermediate and 1.27 times that of Laripur. And the Elastollan shell stiffness is the highest and 1.66 times that of Laripur.

Looking at the table 3.1, it can be seen that in the transition from an imposed rotation of five degrees to one of ten degrees, the torsional stiffness decreases for all three materials (by 7.2% for Laripur, 8.4% for Grilamid and 10.8% for Elastollan). These decreases in stiffness mean that the three materials are stressed beyond their linear elasticity and thus for ten degrees of rotation the material behaviour is more markedly non-linear, which is also confirmed by the increase in normalised dissipated energies (table 3.1). In particular, the normalised dissipated energy

double from five to ten degrees of rotation, which means that the hysteresis cycles are much larger, as can be seen in the comparison in *figure 3.14*.

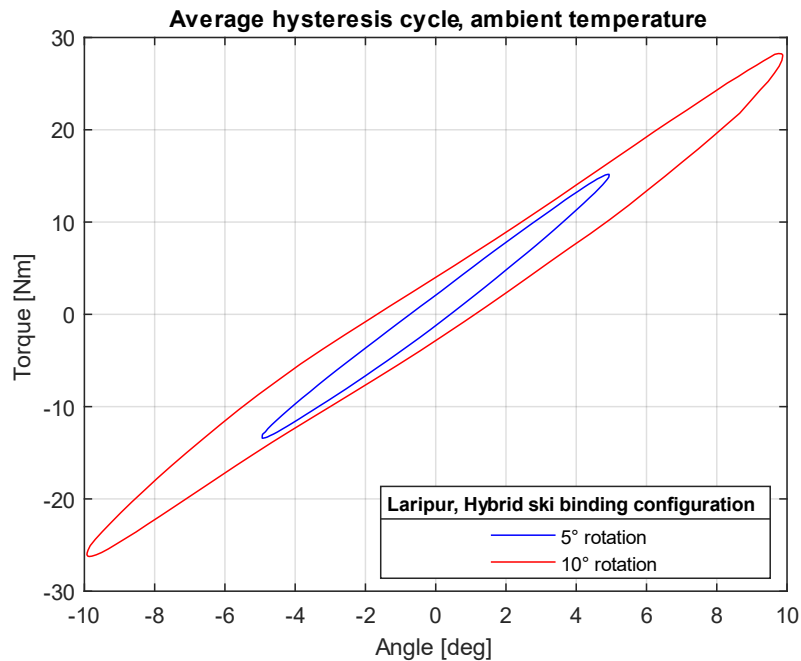


Figure 3.14: comparison of average hysteresis cycle of the Laripur shell for five and ten degrees of imposed rotation, with the hybrid configuration of ski bindings, at ambient temperature

### 3.2.3 Testing with ski touring bindings configuration

The rear downhill ski binding was removed and the ski touring posterior grip was mounted, completing the configuration of ski touring bindings. The movable head of the machine was adjusted to fit the new pair of grips and then re-fixed. One at a time, the three shells (the same ones that had been tested with the hybrid configuration) were taken and mounted in the torsion machine (firstly by fixing them on the front grip and then on the rear one) (*figure 3.15*) and tested by imposing five and ten degrees of rotation.



Figure 3.15: Laripur shell mounted on ski touring binding configuration

The graphs obtained from the test at five and ten degrees of imposed rotation are shown in *figures 3.16 and 3.17*.

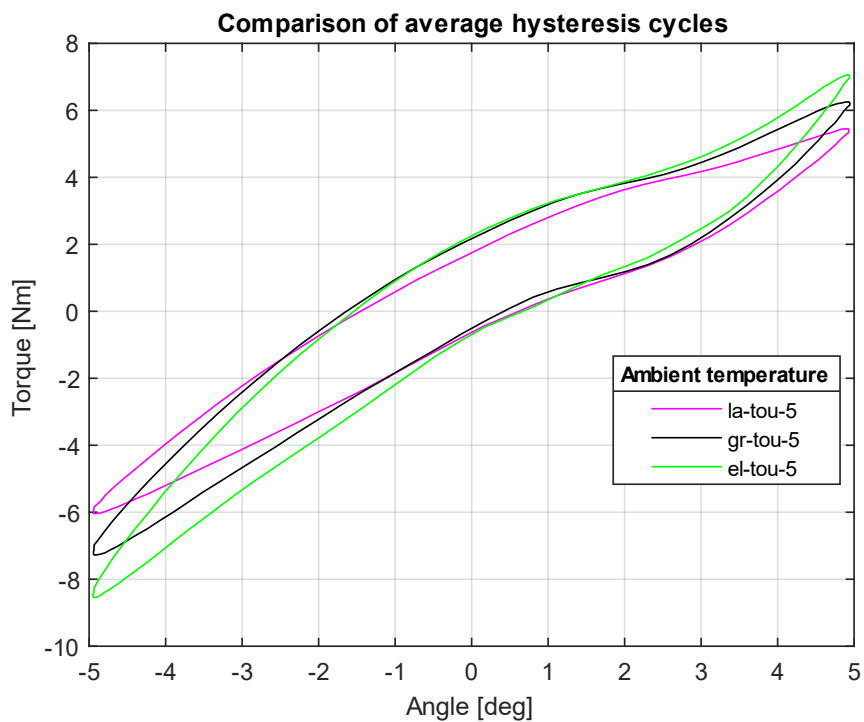


Figure 3.16: comparison of the average hysteresis cycles of Laripur, Grilamid and Elastollan shells, imposing a rotation of five degrees, with the ski touring bindings configuration

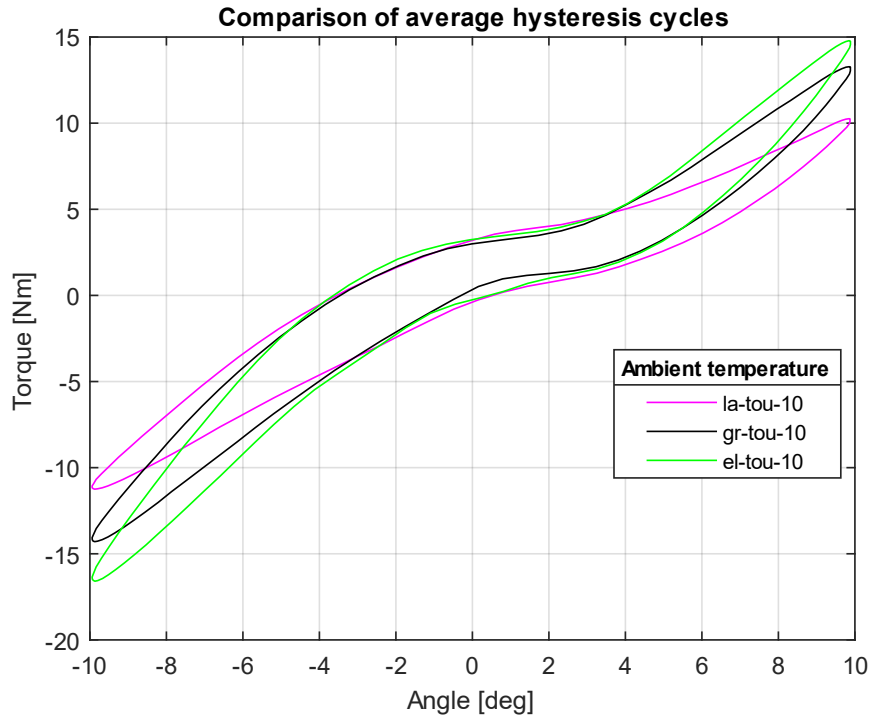


Figure 3.17: comparison of the average hysteresis cycles of Laripur, Grilamid and Elastollan shells, imposing a rotation of ten degrees, with the ski touring bindings configuration

Table 3.2 shows the torsional and the normalised dissipated energy obtained (formula 3.1) for each test. For both the torsional stiffness and normalized dissipated energy, a column with the ratio to the Laripur shell test, with an imposed rotation of five degrees (formula 3.2), is also shown, allowing a quicker understanding of the data.

Ski touring binding configuration, ambient temperature						
Material	Rotation	Peak Torque	Torsional stiffness		Normalized dissipated energy	
		Measured	Measured	Ratio (Laripur 5°)	Measured	Ratio (Laripur 5°)
Laripur	5	5,452	1,125	1	1,883	1
	10	10,259	1,003	0,89	2,999	1,59
Grilamid	5	6,253	1,292	1,15	2,139	1,14
	10	13,277	1,264	1,12	3,001	1,59
Elastollan	5	7,063	1,471	1,31	2,261	1,20
	10	14,789	1,423	1,26	3,405	1,81
	deg	Nm	Nm/deg		J	

Table 3.2: torsional stiffness and normalized dissipated energy obtained for each test with the ski touring bindings configuration, at ambient temperature

Figures 3.15 and 3.16 and table 3.2 confirm that even in the case of the ski touring binding configuration, the Laripur shell is the most deformable and the Elastollan shell is the most rigid. The remarks made in the previous paragraph also apply to these tests: in the transition from five to ten degrees of imposed rotation, it is observed that for all three materials, torsional stiffness decrease, and normalised dissipated energy increase due to more pronounced non-linear behaviour.

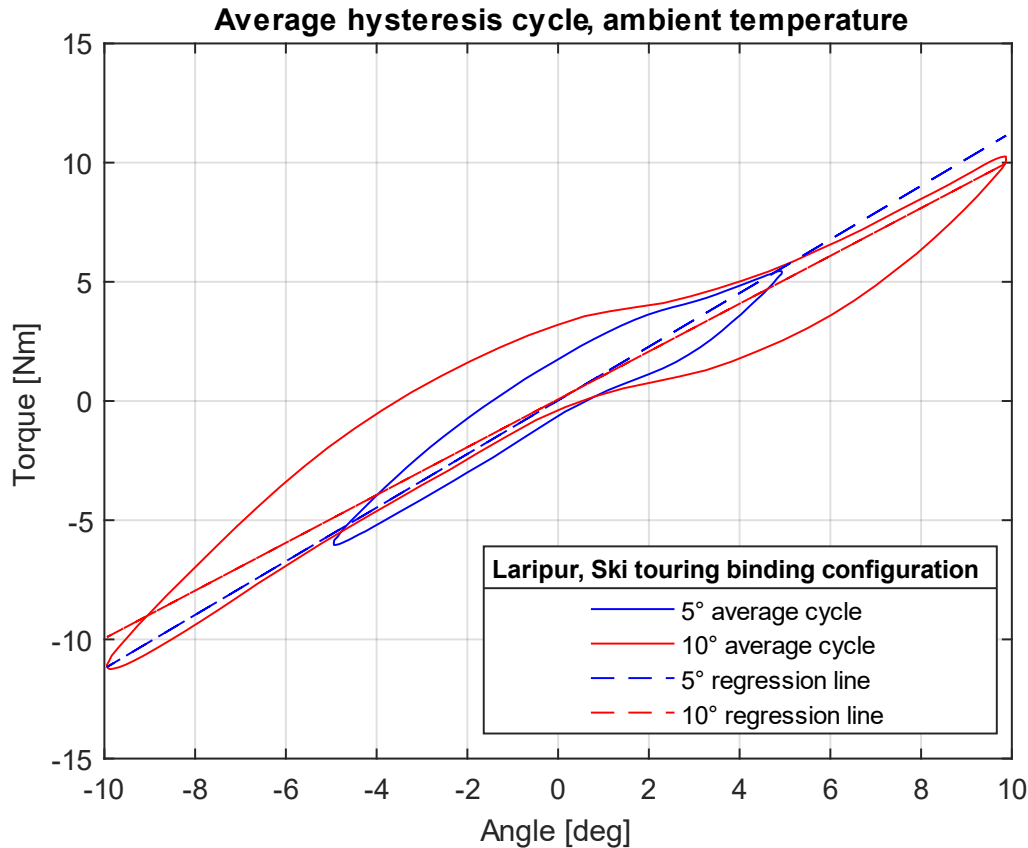


Figure 3.18: comparison of average hysteresis cycle of the Laripur shell for five and ten degrees of imposed rotation, with the ski touring binding configuration,

Observing the hysteresis cycles in *figure 3.15*, and even more accentuated in *figure 3.16*, it can be seen that the hysteresis cycles with the ski touring binding configuration have a more complex form than those seen for the hybrid configuration. In particular, the central area (low angles) has a little slope and is almost horizontal, and then the slope increases as the angles increase (for both positive and negative angles). This is due to the fact that on the heel the shell is only bounded by the two screws simulating the Dynafit binding pins in the rear insert; it is therefore a very localised constraint and dependent on the forces exchanged between the posterior insert and the rear ‘pins’. There is probably a little clearance so that for low angles the rear insert can rotate a little without putting tension on the rear ‘pins’ and so basically, we have an almost rigid rotation of the shell and a low detected stiffness. When rotation angles are higher, the insert and rear ‘pins’ make full contact and the ‘pins’ begin to constrain the shell more effectively; as the torsion angle grows, the forces exchanged between the insert and the rear ‘pins’ intensify and consequently the measured stiffness increases.

### 3.2.4 Comparison of results for the two ski binding configurations

Observing the tests, it can be seen that with the ski touring configuration, the shell deforms much less than when the hybrid configuration is applied (*figures 3.19* and *3.20*).





Figures 3.19: Laripur shell deformation for a rotation of ten degrees when the hybrid ski binding configuration is applied



Figure 3.20: deformation of the Laripur shell for a rotation of ten degrees when the hybrid ski touring binding configuration is applied; as can be seen with the help of the arrows, the shell deformation is less than with the hybrid configuration of ski bindings (*figure 3.18*)

This is because, in addition to the initial phenomena of rigid rotation of the shell, there is a much less rigid constraint at the rear. In fact, in the ski touring rear grip, the constraint consists of two five-millimetre diameter ‘pins’ (which behave like two beams interlocked in the L-beam) and can therefore deform much more than the plate that fixes the heel in the downhill rear grip. Thus, in the ski touring configuration, the heel of the shell will not be prevented from rotating but will rotate

by a certain angle as a result of the deformability of the ‘pins’. In conclusion, therefore, we can say that while with the hybrid configuration only the shell is stressed, with the ski touring configuration the whole set consisting of the shell and rear pins is stressed.

As can be seen in comparison *table 3.3*, there is a reduction in torsional stiffness of between sixty and seventy per cent when switching from the hybrid to the ski-touring configuration. Such marked differences are due to the fact that the rear ski touring binding is much less constraining than the downhill binding.

$$Pct. var. 5^\circ - 10^\circ = \frac{k_{10} - k_5}{k_5} \cdot 100 \quad \text{Formula (3.3)}$$

$$Comparison\ hyb - tou = \frac{k_{tou} - k_{hyb}}{k_{hyb}} \cdot 100 \quad \text{Formula (3.4)}$$

Comparison of torsional stiffness, ambient temperature						
Material	Rotation	Hybrid configuration		Touring configuration		Comparison hyb-tou
		Measured	Pct var 5°-10°	Measured	Pct var 5°-10°	
Laripur	5	2,876		1,125		-60,9%
	10	2,670	-7,2%	1,003	-10,8%	-62,4%
Grilamid	5	3,658		1,292		-64,7%
	10	3,349	-8,4%	1,264	-2,2%	-62,3%
Elastollan	5	4,772		1,471		-69,2%
	10	4,255	-10,8%	1,423	-3,2%	-66,6%
	deg	Nm/deg		Nm/deg		

Table 3.3: comparison of torsional stiffnesses obtained with the hybrid and ski touring configuration, at room temperature

In particular, it can be seen that the reduction in stiffness becomes more pronounced when moving from the more deformable to the more rigid material. This is because with the ski touring configuration the imposed torsion angle is divided between the shell and rear ‘pins’, which, having a very small diameter, will be the least rigid element of the series and will therefore deform the most. So, the stiffer the shell, the more deformation will be concentrated on the rear ‘pins’, lowering the stiffness of the system more. This reduces the differences between the torsional stiffness of the various material shells; in fact, for an imposed rotation of five degrees, while with the hybrid configuration the rigidity of the Elastollan shell was 1.66 times that of the Laripur shell (*table 3.1*), with the ski touring configuration it becomes 1.31 times that of Laripur shell (*table 3.2*). This mean that if different materials of the shells, or possible different shell geometries, affect torsional stiffness to a certain extent with downhill bindings, these differences become much less relevant when switching to ski touring bindings (reminding that the shell analysed belongs to a hybrid ski boot, which is used 60% on the ski slope and 40% for ski touring).

As can be seen in *table 3.4*, in the tests with the ski touring configuration, there is a marked reduction in normalised dissipated energies (NE) compared to the hybrid

configuration: for five degrees of imposed rotation, the differences range between 26.1% and 39.0%, while for ten degrees they range between 45.8% and 61.2%.

$$\text{Comparison hyb - tou} = \frac{NE_{tou} - NE_{hyb}}{NE_{hyb}} \cdot 100 \quad \text{Formula (3.5)}$$

Comparison normalized dissipated energy, ambient temperature						
Material	Rotation	Hybrid configuration		Touring configuration		Comparison hyb-tou
		Measured	Pct var 5°-10°	Measured	Pct var 5°-10°	
Laripur	5	2,548		1,883		-26,1%
	10	5,531	117,1%	2,999	59,3%	-45,8%
Grilamid	5	3,823		2,139		-44,0%
	10	7,732	102,3%	3,001	40,3%	-61,2%
Elastollan	5	3,706		2,261		-39,0%
	10	8,680	134,2%	3,405	50,6%	-60,8%
	deg	J		J		

Table 3.4: comparison of normalised dissipated energies obtained with the hybrid and ski touring configuration, at room temperature

This reduction in normalised dissipated energy is due to a reduction in the area of the hysteresis cycles, as can be seen in *figure 3.21* from a comparison of the average cycles obtained for the Elastollan by imposing a rotation of ten degrees, with the two different ski binding configurations.

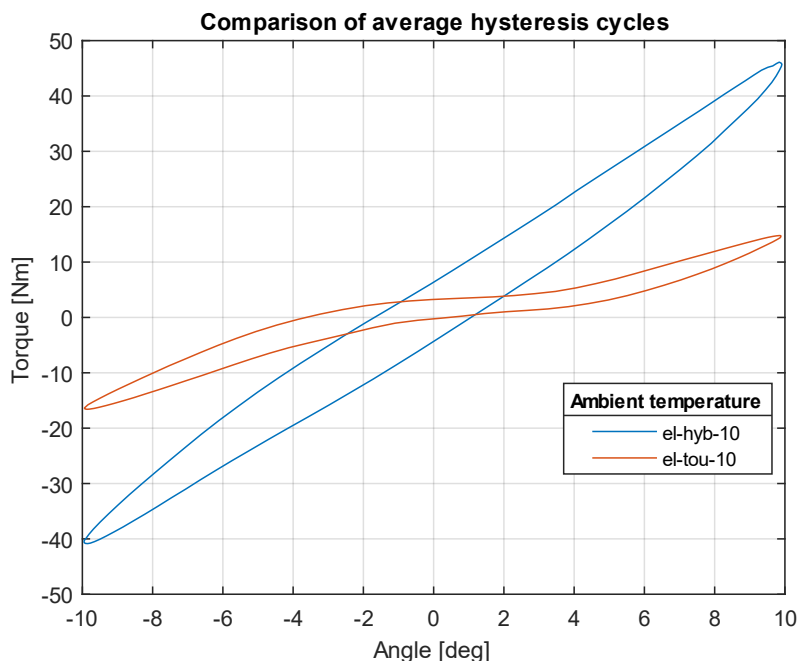


Figure 3.21: comparison of average hysteresis cycle of the Elastollan shell ten degrees of imposed rotation, with the two different ski binding configurations, at ambient temperature

These reductions in the area of the average hysteresis cycles are due to the fact that, as can be seen in *figure 3.21*, with the ski touring configuration, the applied torques are much lower and therefore the shell materials behave more linearly. The fact that shells materials are stressed with lower tension and therefore behave more

linearly also explains the smaller variations in normalised dissipated energies between test at five and ten degrees of rotation imposed with ski touring bindings (*table 3.4*).

The fact that shells materials behave more linearly also explains the fact that, in the transition from five to ten degrees of imposed rotation, the reduction in torsional stiffness is much less with the ski touring configuration, where it is between 2.2 and 3.2% (except for the Laripur), than with the hybrid configuration, where reductions were between 7.2 and 10.8%.

The test at ten degrees of imposed rotation performed on the Laripur shell with ski touring binding gives a torsional stiffness that differs by 10.8% from that obtained for five degrees of imposed rotation (*table 3.3*). Probably in this test the shell was not constrained well at the rear 'pins' and therefore the stiffness obtained is lower than expected. In favour of this hypothesis, we can observe the comparison column between five and ten degrees of imposed rotation of the hybrid configuration, where Laripur is the material with the lowest percentage variation, and we would therefore expect a similar trend for the hybrid configuration. Another point in favour of this hypothesis is the fact that in the final column comparing the stiffnesses with hybrid and ski touring configurations, Laripur is the only material for which, when going from five to ten degrees of imposed rotation, the percentage of reduction in torsional stiffness increases. The conclusion is that, when performing tests with the posterior ski touring grip, special attention must be paid to the positioning of the 'pins' in the insert, because being a very localised constraint it is likely that small shifts are sufficient to vary the test results.

### 3.3 Conclusions

For ski boots, an important performance parameter is the boot mass, which must be reduced as much as possible. After weighing the shells, it was possible to calculate the specific torsional stiffnesses (dividing the torsional stiffnesses  $k$  by the mass of the shells  $m$ ) in order to determine which material makes the Markab shell more efficient.

$$Spec. tors. stiff = \frac{k}{m} \quad \text{Formula (3.6)}$$

The specific torsional stiffnesses are given in *table 3.5*.

Specific torsional stiffnesses, ambient temperature						
Material	Shell mass	Rotation	Hybrid configuration		Touring configuration	
			Tors. Stiff.	Spec. Tors. Stiff.	Tors. Stiff.	Spec. Tors. Stiff.
Laripur	0,637	5	2,876	4,518	1,125	1,768
		10	2,670	4,194	1,003	1,576
Grilamid	0,523	5	3,658	6,991	1,292	2,470
		10	3,349	6,401	1,264	2,415
Elastollan	0,636	5	4,772	7,505	1,471	2,312
		10	4,255	6,692	1,423	2,238
	kg	deg	Nm/deg	Nm/(deg*kg)	Nm/deg	Nm/(deg*kg)

Table 3.5: specific torsional stiffnesses obtained with the hybrid and ski touring configuration, at room temperature

As can be seen for the hybrid ski binding configuration, the most efficient shell is made of Elastollan, while for the ski touring configuration, the Grilamid shell offers the best performance due to its very low weight.



## Chapter 4: Numerical simulations of shell torsion tests

This chapter will present the numerical simulations performed, using the Finite Element Method (FEM), in order to replicate the tests performed on the torsion bench with the three shell of different materials and with the two grip configurations described in *chapter 3*. It will be explained how material properties were implemented from data obtained from characterisation tests performed at Tecnica, how the models described in *chapter 2* were imported, and how contacts, constraints and loads were set for the analysis. Finally, it will be explained how the torsional stiffness of the shells were derived and the results obtained from numerical simulations will be compared with those from experimental tests in the laboratory.

### 4.1 Numerical simulations of shell torsion with hybrid ski binding configuration

As seen in *chapter 2*, the component to be analysed consist of the polymer shell and the front and rear steel inserts. As a first step, in the programme used for numerical simulations (Ansys Workbench) it will be necessary to choose material behaviour models and set the required mechanical properties for the polymer of the shell and the steel of the inserts. Therefore, having created three components in Rhinoceros, these must be brought together in an assembly, with correct positioning of the parts in relation to each other. Then it is necessary to assign materials to the various components, impose boundary conditions that simulate those of the experimental test and set the parameters for creating the mesh. Finally, we choose the analysis settings and solve the FEM model, obtaining a torque at the constrained end of the shell, from which we derive the torsional stiffness, which will be compared with that obtained experimentally.

#### 4.1.1 Setting materials in Engineering data

From the data sheets in the company's database we know the elastic flexural modulus at 23°C (EFM) of Laripur and the Elastollan mixture, no data were available for the Grilamid mixture (*table 4.1*).

Elastic flexural modulus at 23°C	
Material	EFM (23°C)
Laripur 6650	340
Grilamid mixture	/
Elastollan mixture	590
	MPa

Table 4.1: elastic flexural moduli of the three shell materials, provided by the company's data sheets

Not having data available on the stress-strain curves of these materials, it was decided to start with numerical simulations by implementing a linear elastic material model.

To set up materials, after opening Ansys Workbench and dragging 'Static Structural' from the toolbox into 'Project Schematic' (figure 4.1), we have to double-click on 'Engineering Data'.

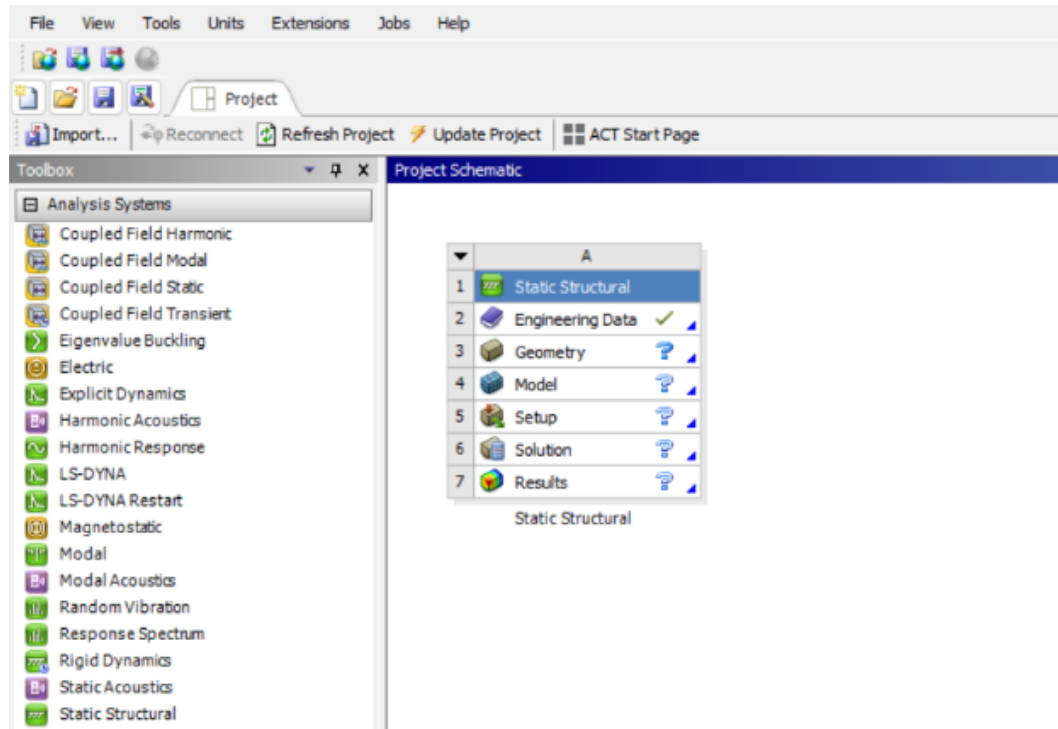


Figure 4.1: creating a 'Static Structural' analysis on Ansys Workbench

In the 'Engineering Data' window that opens, we create a new material and from the toolbox on the left we include in it only the properties related to 'Linear Elastic – Isotropic Elasticity'. Then the Young's modulus found in the data sheets (table 4.1) is entered and, as we have no Poisson's ratio data, a value of  $\nu = 0.33$  is assumed for all polymers.



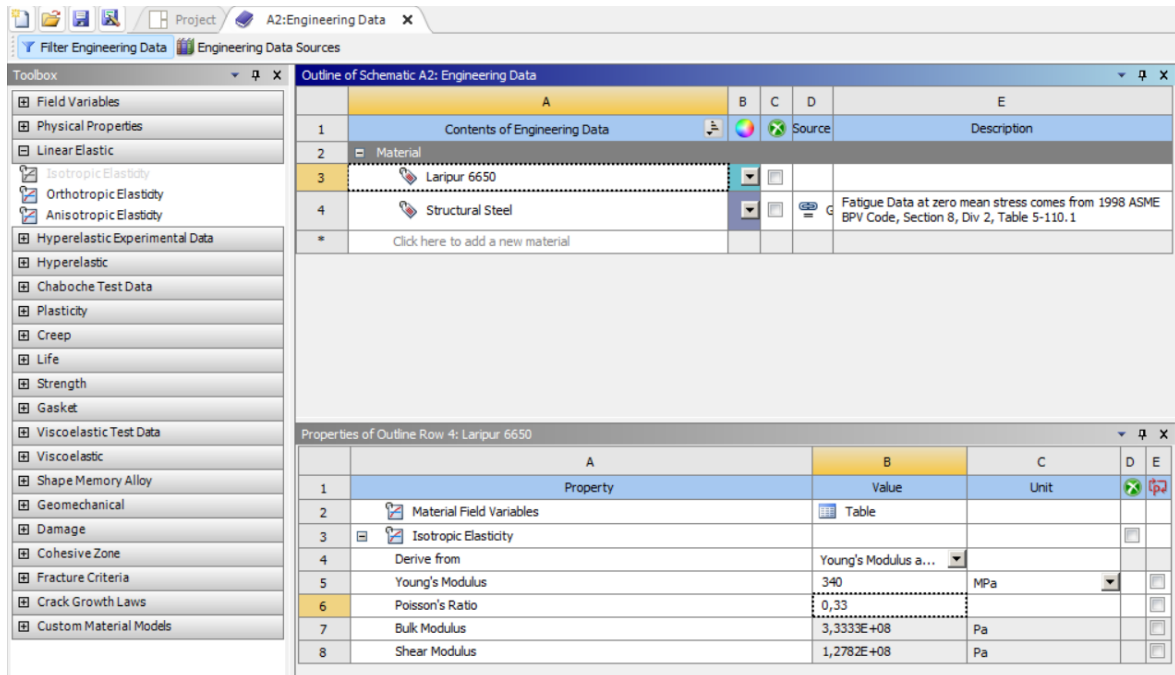


Figure 4.2: creation of the 'Laripur 6650' material in 'Engineering Data' and assignment of its mechanical properties

With regard to the inserts, the material of the front one is 34CrAlNi7, while material of the rear one is 18NiCrMo5; for both we will use the 'Structural Steel' already present in the Ansys library (*figure 4.2*), whose mechanical properties are a Young's modulus  $E = 200'000 \text{ MPa}$  and a Poisson's ratio  $\nu = 0.3$ .

#### 4.1.2 Creating an assembly on Ansys SpaceClaim

After setting the materials, return to the 'Project' window (*figure 4.1*), right-click on 'Geometry' and select 'New SpaceClaim Geometry...'. Once in SpaceClaim, open the Rhinoceros file of the shell obtained by the procedure described in *chapter 2*. At this point, using the '*Fill*' command in the '*Sketch*' window, we perform defeaturing operations on the C.A.S. and the Tecnica logos on the sides of the shell (*figures 4.3 and 4.4*), in order to make it easier to create the mesh in Ansys Mechanical.

Click an object. Double-click to select an edge loop. Triple-click to select a solid.

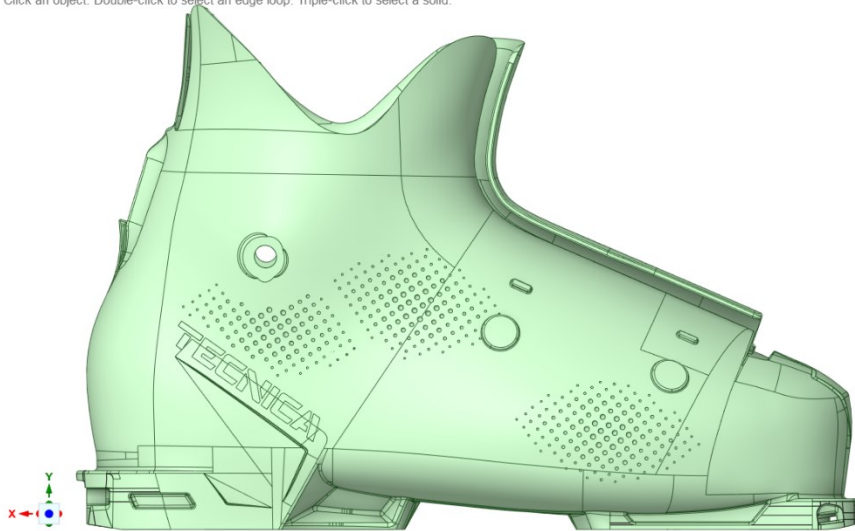


Figure 4.3: solid model of the shell imported into Ansys Workbench

Click an object. Double-click to select an edge loop. Triple-click to select a solid.

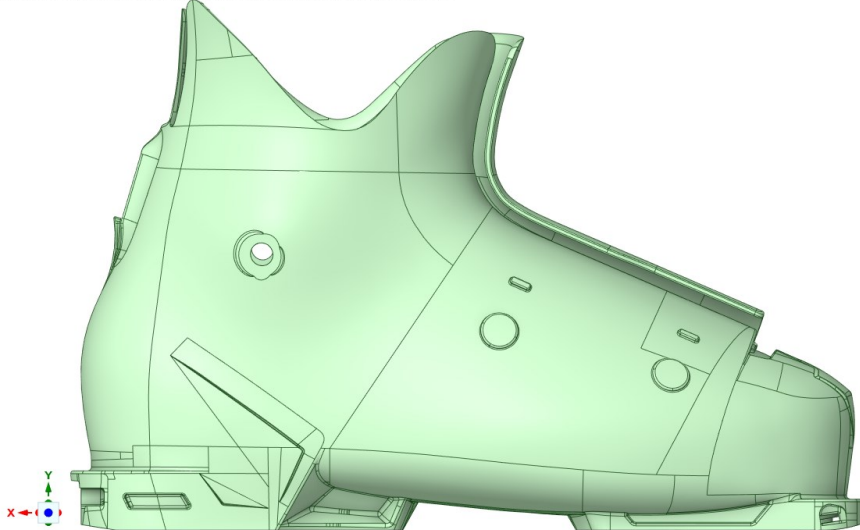


Figure 4.4: solid model of the shell after defeaturing operations

We then save this shell model in SpaceClaim format, as we will also need it for simulations with the ski touring binding configuration.

A further necessary operation to be carried out on the shell concerns the subdivision of the lower surface of the shell heel (*figure 4.5*).

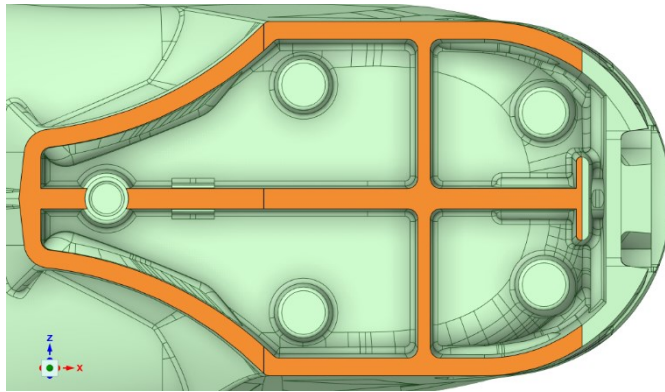


Figure 4.5: lower surface of the shell heel

In order to correctly simulate the rear downhill ski binding, it is in fact necessary to have a surface that corresponds to the area where the shell touches the supporting c-beam (figure 4.6).



Figure 4.6: zoom of the rear downhill ski constraint

Using the 'Split' command in the 'Design' window, first select the surface to be split and then the split line (to help position the line for subdividing the surface, a line was created on Rhinoceros, visible in figure 4.5); if more surfaces than desired are created, they can then be joined using the 'Merge Faces' command in the 'Repair' window.

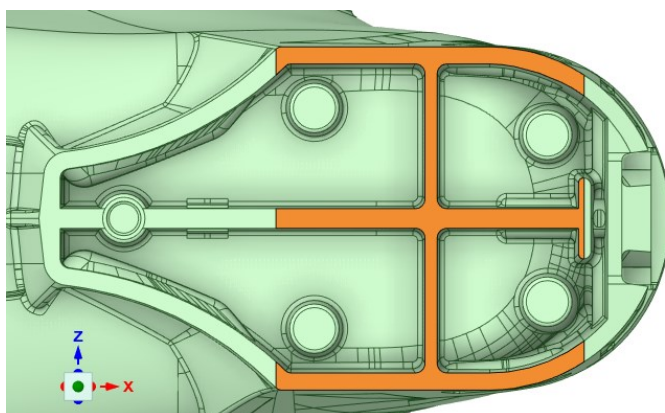
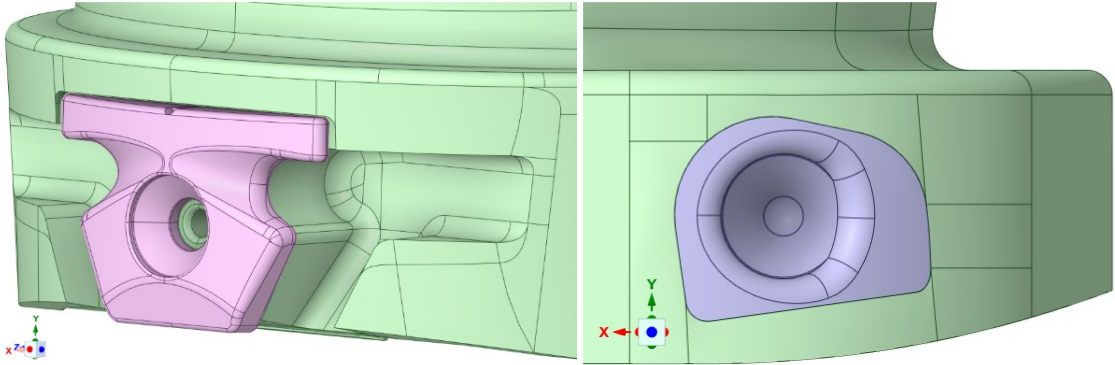


Figure 4.7: surface area corresponding to the heel area of the shell actually in contact with the supporting c-beam of the downhill ski binding

At this point the shell model is finished and we can go on to create an assembly using the *'File'* command in the *'Assembly'* window, which allows us to import the front and rear inserts. Since the inserts were already correctly positioned relative to the shell in Rhinoceros, no repositioning needs to be performed once they have been imported into Ansys SpaceClaim.



Figures 4.8-4.9: details of the front and rear inserts in the created assembly, for hybrid ski binding configuration

**4.1.3 Assembly management on Ansys Mechanical**

Once the assembly have been created, return to the 'Project' screen (figure 4.1), right-click on 'Model' and select 'Edit...'. Once Ansys Mechanical opens, on the left we can see the project tree shown in figure 4.10.

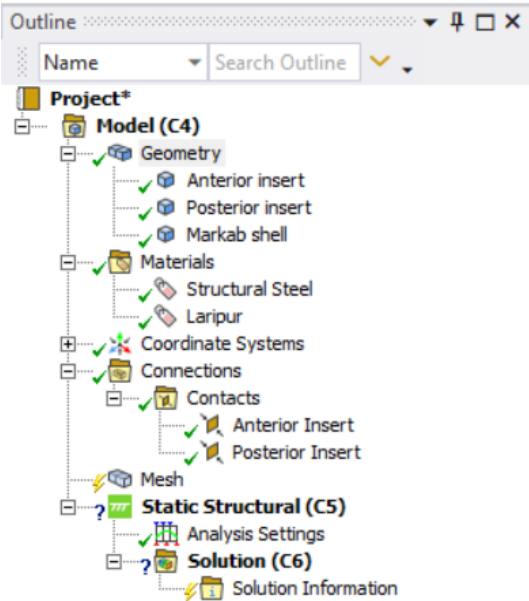
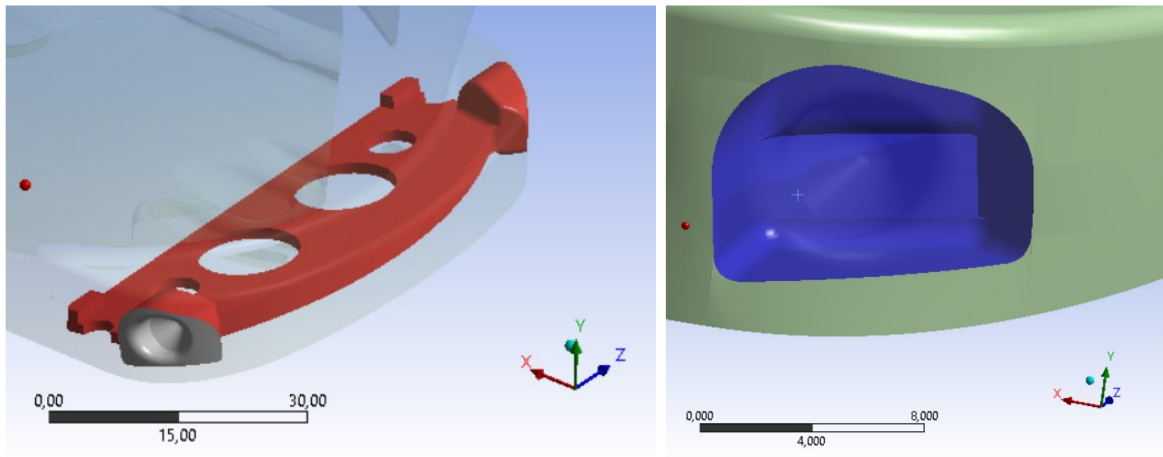


Figure 4.10: project tree in Ansys Mechanical

Under 'Geometry' we select the three components one at a time and assign each its material: polymer for the shell and steel for the inserts.

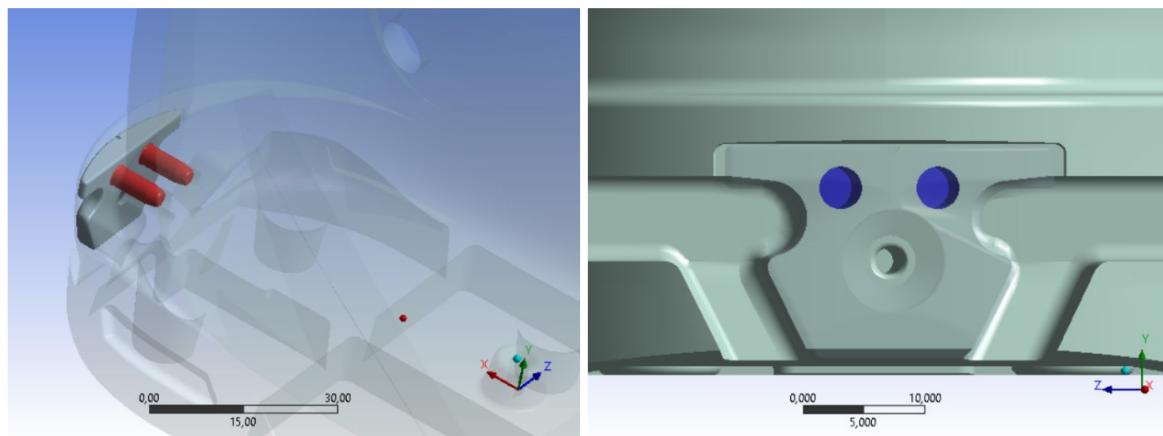
Under 'Contacts' for the anterior insert, the 'bonded' type of contact was chosen, and the faces affected by this type of contact were left as those automatically recognised by the software (figures 4.11 and 4.12). This is because the shell is

obtained by injection moulding and the front insert is placed inside the mould so that the polymer material adheres perfectly to it and we can assume that, therefore, there is no sliding between insert and shell.



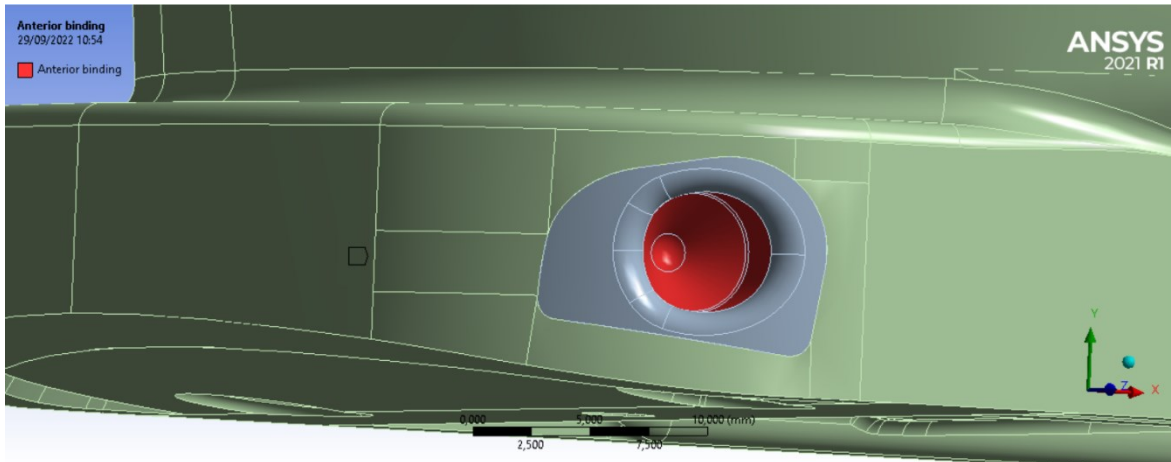
Figures 4.11-4.12: surfaces involved in bonded contact: in red those of the front insert, in blue those of the shell

The 'bonded' type of contact was also chosen for the contacts on the rear insert, but the selected surfaces were modified. In this case the two pins of the insert must be forced into the holes in the shell, having a larger diameter, and then the insert is secured with a screw. Leaving the contact type 'bonded' on all the faces identified by Ansys would excessively constrain the insert to the shell and, therefore, only the faces at the insert pins and holes on the shell were selected, as can be seen in figures 4.13 and 4.14.



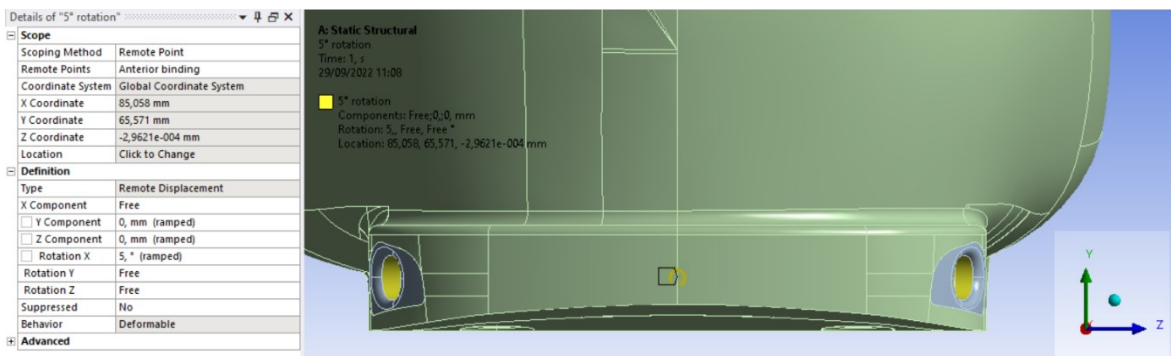
Figures 4.13-4.14: surfaces involved in bonded contact: in red those of the rear insert, in blue those of the shell

Constraints and loads must now be defined for the hybrid configuration of ski bindings. Starting with the loads, a rotation of five (or ten) degrees must be imposed on the front pin seats. To do this, create a remote point by right-clicking on 'Model' (figure 4.10) and then selecting 'Insert – Remote Point'. In 'Scope' of the remote point menu, as 'Geometry' all faces of both front pin seats are selected, as shown in figure 4.15. We then rename the remote point as 'Anterior binding'.



Figures 4.15: creation of the remote point called 'Anterior binding' by selecting all faces of both front pin seats

To apply the rotation, right-click on 'Static Structural' (*figure 4.10*) and select 'Insert – Remote Displacement'. Then, in the 'Scope' menu of the remote displacement (*figure 4.16*), 'Remote Point' is selected as 'Scoping Method' and 'Anterior binding' is selected as 'Remote Points'. Moving on to the 'Definition' menu, we then apply to the remote point a zero translation in the Y and Z directions and a rotation of five (or ten) degrees around the X axis (*figure 4.16*).

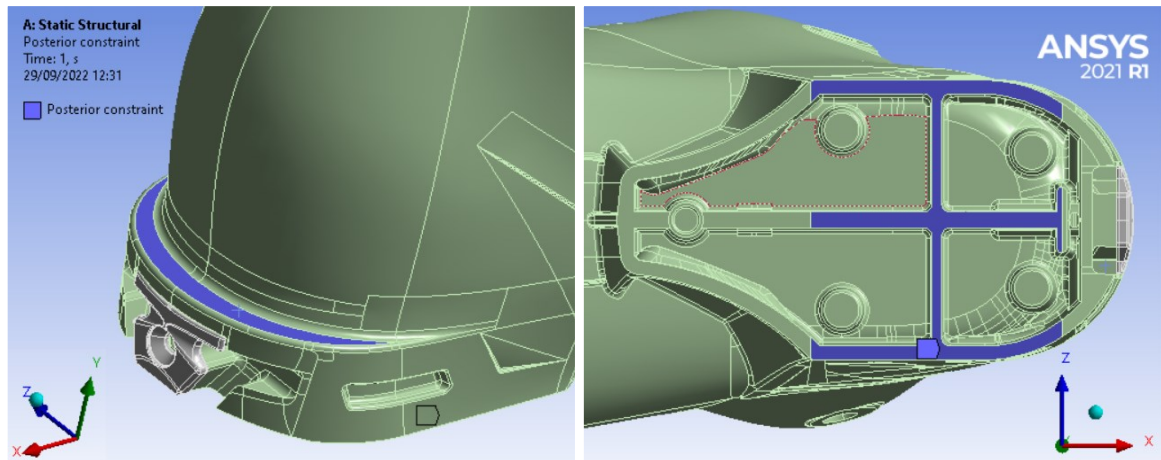


Figures 4.16: application of five-degree rotation to the front pin seats

Having used a remote, what we are doing is constraining the centre of gravity of the selected faces not to translate in the Y and Z directions and to rotate five degrees around the X axis. We are applying these boundary conditions because, in the experimental test, rotation is applied by the front grip, which rotates around the axis of rotation of the torsion machine head and cannot translate in the Y and Z directions. Translations in the X-direction is instead left free because, during the experimental test, the rear end of the torsion machine can translate in that direction to compensate any possible elongation or shortening of the component.

To complete the boundary conditions, it remains to apply the constraint corresponding to the rear downhill ski grip; to do so, right-click on 'Static Structural' and select 'Insert – Fixed Support'. As 'Scoping Method' we leave 'Geometry Selection' and select the two faces to be constrained: the upper one (*figure 4.17*) where the plate of *figure 3.5* rests, and the lower one (*figure 4.18*) where the shell

rests on the c-beam of *figure 3.4*. We then rename the fixed support as ‘Posterior constraint’.



Figures 4.17-4.18: faces on which the fixed support boundary condition is applied, for hybrid ski binding configuration

The boundary condition of ‘Fixed Support’ means that the selected faces do not translate or rotate in any direction; the possibility in the experimental tests for the rear grip to translate in the X-direction was taken into account in the application of the ‘Remote Displacement’ on the front pin seats.

Once the boundary conditions have been defined, we can move on to the definition of the mesh: by right-clicking on ‘Mesh’ (*figure 4.10*) we first select ‘Insert – Method’ and then ‘Insert – Sizing’. As regards the method, a mesh with tetrahedral elements (Tet10) has been chosen, while the size of the elements will be decided on the basis of the convergence diagram of the results.

In order to calculate the torsional stiffness of the shell, we need to output the torque applied in order to achieve the imposed rotation (as in the experimental tests where the torque was measured from the load cell). To do this, right-click on ‘Solution’ (*figure 4.10*) and select ‘Insert – Probe – Moment Reaction’; then, in the ‘Definition’ menu of the moment reaction probe, select ‘Posterior constraint’ as ‘Boundary Condition’. It is then sufficient to divide the reaction moment obtained by the imposed rotation to obtain the torsional stiffness.

Finally, after clicking on ‘Analysis Settings’, in the ‘Solver Controls’ menu we turn on ‘Large Deflections’. The inclusion of large deflections means that Ansys accounts for changes in stiffness due to changes in the shape of the part we are simulating [10]. At this point we can perform the FEM analysis and calculate the torsional stiffness we obtain as output.

#### 4.1.4 Convergence of numerical simulation

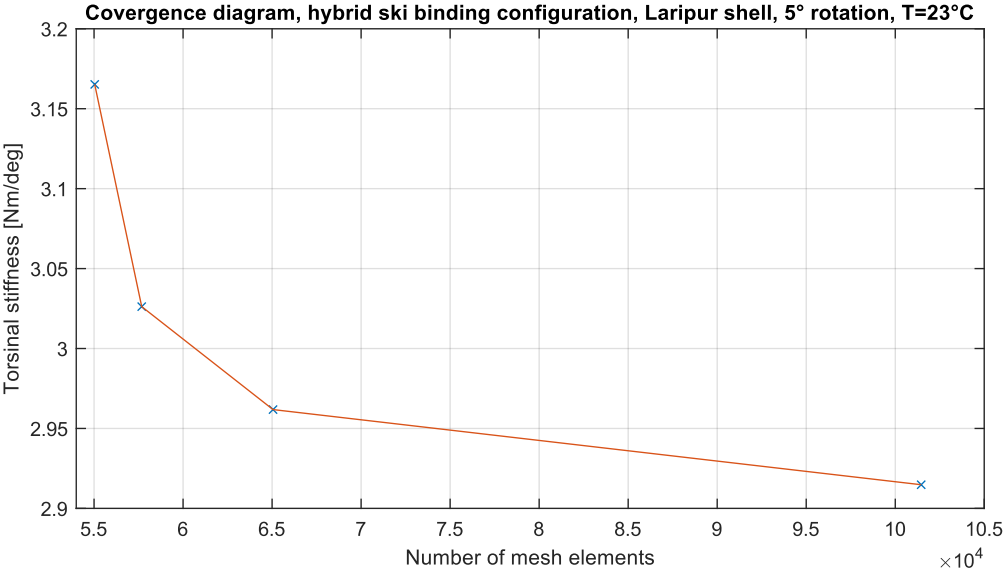
In order to choose an appropriate mesh density (sufficiently dense to obtain good results without making the analysis too onerous), a convergence study was carried out on the results obtained by varying the size of the mesh elements. We started

with a coarse mesh, with an element size of 19 millimetres and then the mesh was progressively thickened; the results obtained are shown in *table 4.2* and the convergence diagram is represented in *figure 4.19*.

$$Pct. \text{ var.} = \frac{k_{old} - k_{new}}{k_{new}} \cdot 100 \quad \text{Formula (4.1)}$$

FEM, hybrid ski binding configuration, Laripur shell, 5° rotation, T=23°C					
Element size	Number of elements	Moment reaction	Torsional stiffness	Pct var	Time sol.
19	55037	15,826	3,1652		128
14	57677	15,131	3,0262	4,6%	146
9	65053	14,809	2,9618	2,2%	263
5	101457	14,574	2,9148	1,6%	186
mm		Nm	Nm/deg		s

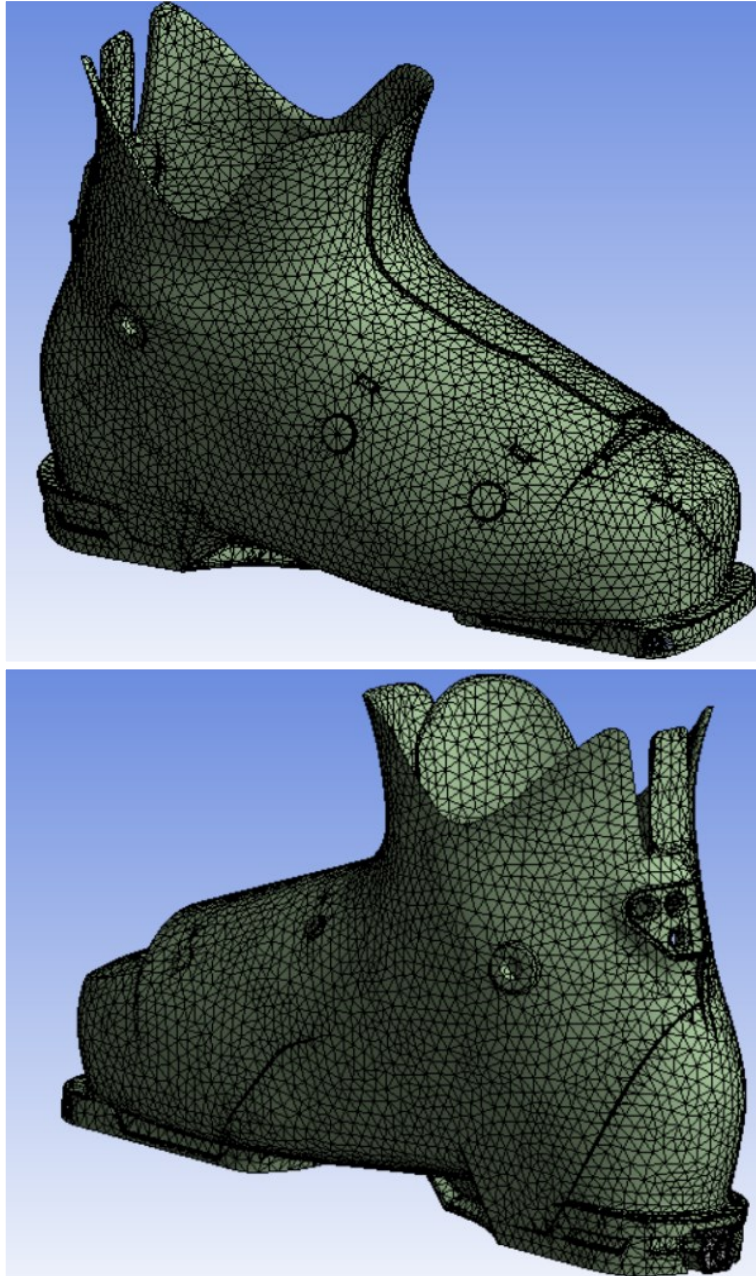
Table 4.2: stiffnesses obtained from numerical simulations for the Laripur shell by applying five degrees of rotation and progressively reducing the size of the mesh elements, for hybrid ski binding configuration



Figures 4.19: Laripur shell torsional stiffness convergence diagram for an imposed rotation of five degrees, for hybrid ski binding configuration

Observing the percentage variations in *table 4.2* and the convergence diagram in *figure 4.19*, we can assume that, with a mesh with five-millimetre elements, convergence is achieved. Similar diagrams were obtained for all three materials and for both five and ten degrees of rotation and, therefore, the mesh used for torsion numerical simulations with hybrid configuration of ski binding consist of tetrahedral elements (Tet10) with an element size of five millimetres (*figures 4.20* and *4.21*).

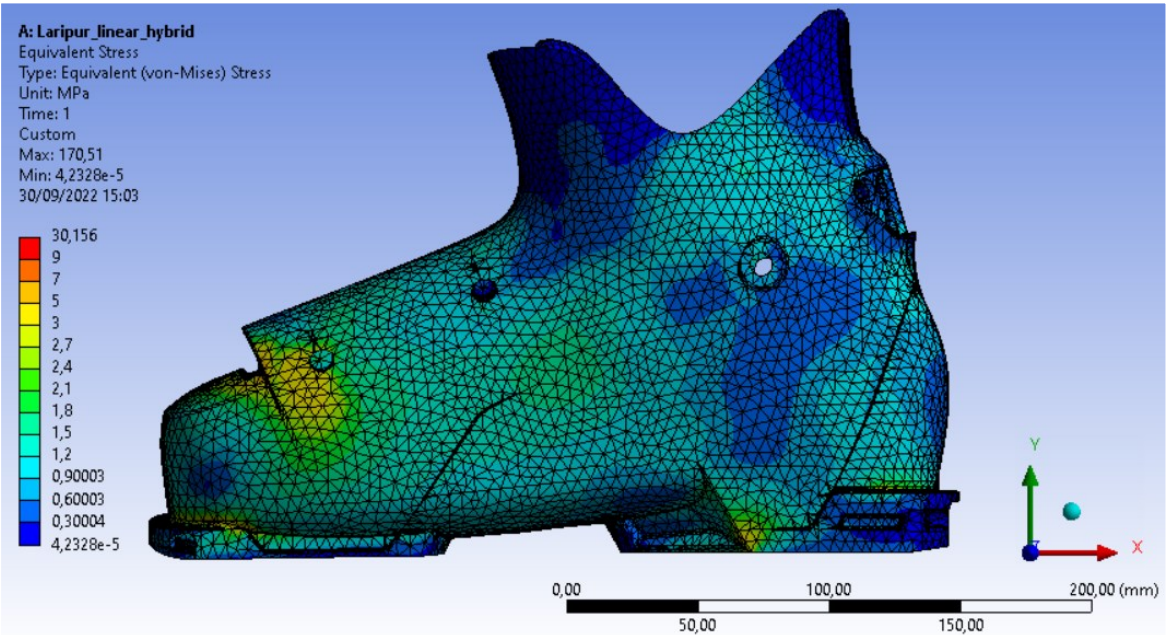
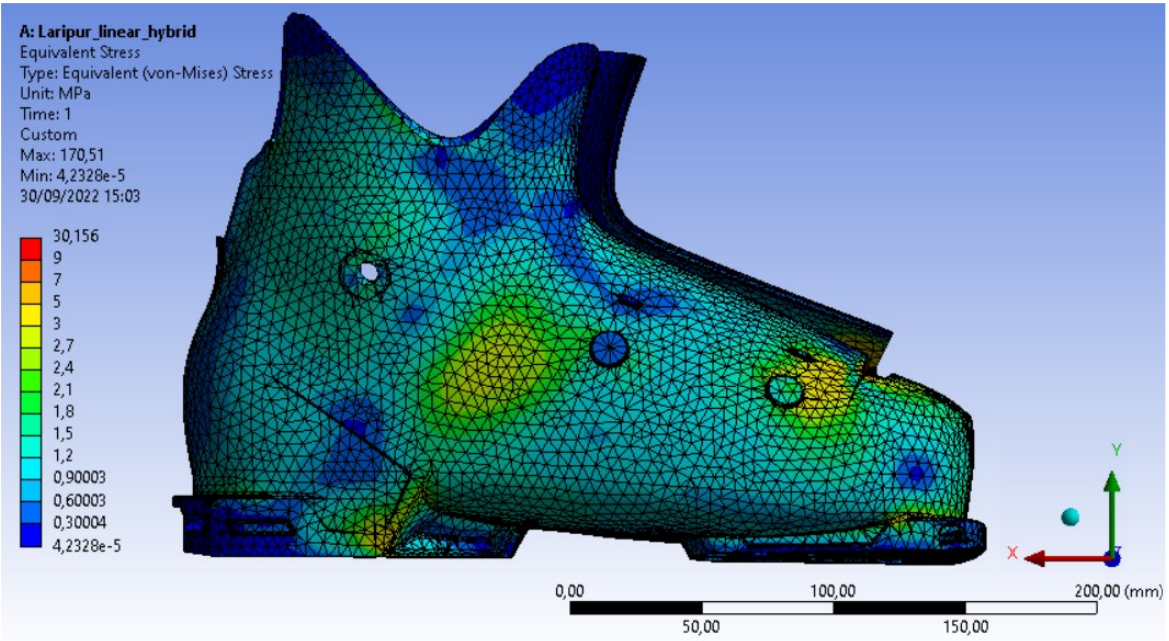




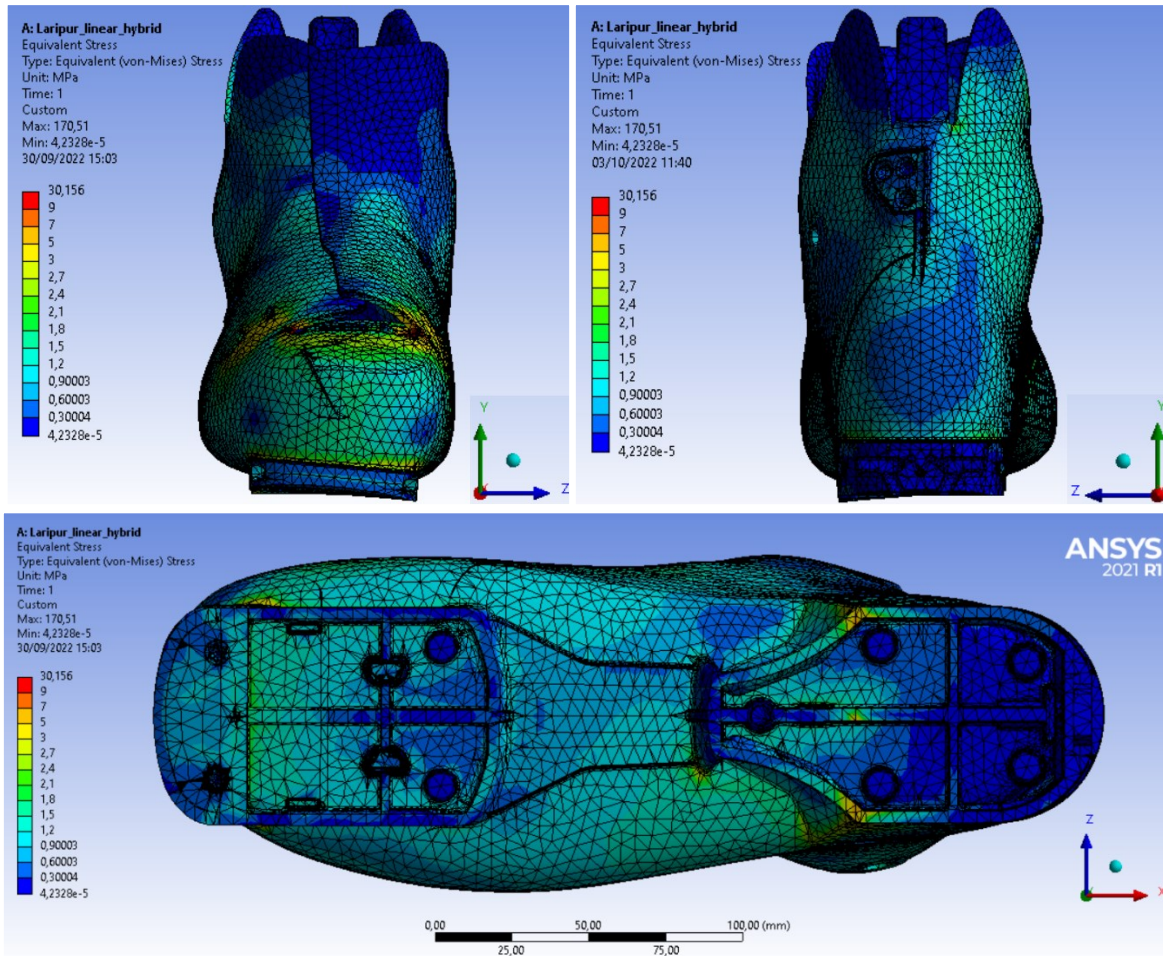
Figures 4.20-4.21: mesh used for FEM torsion analysis, for hybrid ski binding configuration: Tet10 elements with element size of 5 mm

#### 4.1.5 Result of numerical torsion simulations

With the procedure explained in the previous paragraph, imposing a rotation of five degrees on the shell in Laripur results in a reaction moment in the X-direction of  $14.574 \text{ Nm}$ , giving a torsional stiffness of  $2.915 \text{ Nm/deg}$ . To give an idea of the stress distribution, colour maps of the equivalent Von Mises stress are shown in the figures below (being a polymeric material, it is theoretically not correct to take into account the equivalent Von Mises stresses, but these colour maps nevertheless allow a visualisation of the most stressed areas of the shell).



Figures: 4.22-4.23: front and back view views of the colour map of Von Mises' equivalent stress for the Laripur shell, imposing a torsion of five degrees, for hybrid ski binding configuration



Figures: 4.24-4.25-4.26: other views of the colour map of Von Mises' equivalent stress for the Laripur shell, imposing a torsion of five degrees, for hybrid ski binding configuration

From this analysis on the Laripur on the shell for a torsion of five degrees, a significant influence of the front insert on the torsional stiffness obtained can be observed (8.1%), justifying the use of a separate steel component to be added to the assembly (torsion analysis without front insert is presented in *appendix C*).

The torsional stiffnesses obtained in numerical torsion simulations and the comparison with the experimental ones are shown in *table 4.3*.

$$Num. \text{ pct. var.} = \frac{k_{num} - k_{exp}}{k_{exp}} \cdot 100 \quad \text{Formula (4.2)}$$

Comparison of torsional stiffness, hybrid configuration, T=23°C				
Material	Rotation	Experimental	Numerical	Num pct var
Laripur	5	2,876	2,915	1,4%
	10	2,670	2,779	4,1%
Elastollan	5	4,772	4,962	4,0%
	10	4,255	4,732	11,2%
	deg	Nm/deg	Nm/deg	

Table 4.3: comparison of torsional stiffnesses obtained experimentally and numerically, for hybrid ski binding configuration

As can be seen, the results obtained numerically are very close to the experimental results for the Laripur shell and also for the Elastollan shell, for an imposed rotation of five degrees. For the Elastollan shell and an imposed rotation of ten degrees the difference between experimental and numerical torsional stiffness increases, but still remains in a good range.

It can be seen that the torsional stiffness estimated from numerical simulations is always higher than that derived from experimental tests, and that for both materials, going from five to ten degrees of imposed rotation, the difference increases. This could be due to the fact that in numerical simulations we considered the material as linear elastic, whereas in the experimental test non-linear elasticity phenomena of the polymer material could occur. By going from five to ten degrees of imposed rotation, the non-linear phenomena will be more pronounced and, consequently, the torsional stiffness decreases more in the experimental tests, as can be seen from the ratios in *table 4.4*.

$$Ratio = \frac{k}{k_{5^\circ}} \tag{Formula (4.3)}$$

Torsional stiffness ratio, hybrid configuration, T=23°C			
Material	Rotation (deg)	Experimental	Numerical
Laripur	5	1	1
	10	0,928	0,953
Elastollan	5	1	1
	10	0,892	0,954

Table 4.4: torsional stiffness compared to those obtained for five degrees of imposed rotation, for hybrid ski binding configuration

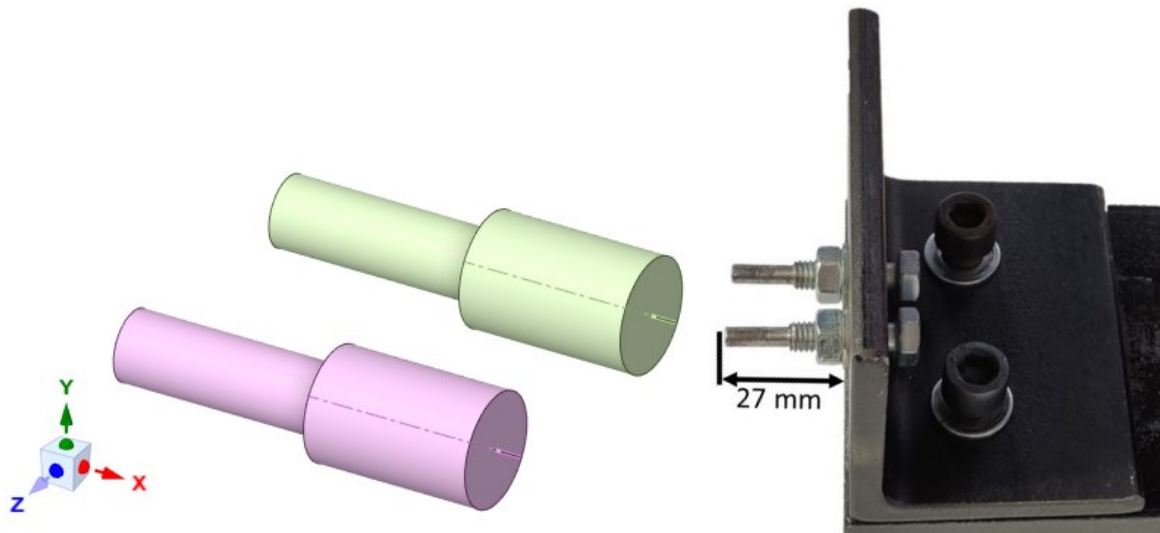
## 4.2 Numerical simulations of shell torsion with ski touring binding configuration

The numerical analysis will be set up in a similar way to what has already been explained in *subchapter 4.1*, with the only difference being that in this case the ‘pins’ of the rear ski touring grip will also be modelled and therefore we will have an additional element in the assembly and new contacts to manage. In particular in ‘Engineering Data’ the same materials as *section 4.1.1* will be set, since the screws simulating the rear pins are also made of steel, so the ‘Structural Steel’ material in the Ansys library will also be assigned to these elements.

### 4.2.1 Creating an assembly on Ansys SpaceClaim

As explained in chapter 3, with this configuration of ski touring bindings, the rear ‘pins’ are also stressed and must therefore also be modelled in order to perform a realistic numerical analysis. In fact, in FEM simulation in which the ‘pins’ were not modelled, and the rear constraint was applied directly on the rear insert, much higher torsional stiffnesses were obtained than in the experimental tests, in addition to the fact that it was complicated to choose which type of constraint to apply. For

this reason, two rear 'pins' were created in Rhinoceros, in order to position them correctly with respect to the posterior insert, and then imported into SpaceClaim (figure 4.27). In particular, the 'pins' were not modelled along their entire length, but only the portion protruding from the L-beam was considered (figure 4.28), at the end of which an interlocking constraint will be applied. A constant diameter of 7.5 millimetres was used to model the stem of the M8 screw (used to simulate the rear pins of the Dynafit binding) in the section that was not machined on the lathe.



Figures 4.27-4.28: posterior pins modelled in Rhinoceros and indication of the dimension from which their overall length was decided, for ski touring binding configuration

The assembly created in Ansys SpaceClaim for the hybrid configuration was then resumed and the posterior pins were imported as an additional element of the assembly. The ends of the pins were spaced two millimetres from the bottom of the cavity in the heel of the shell, to replicate the conditions under which the experimental tests were carried out.

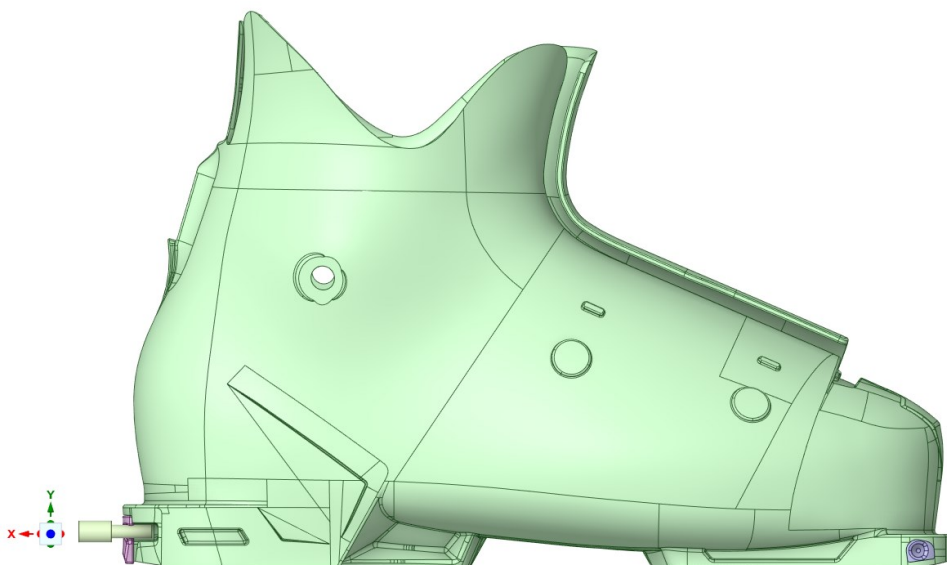
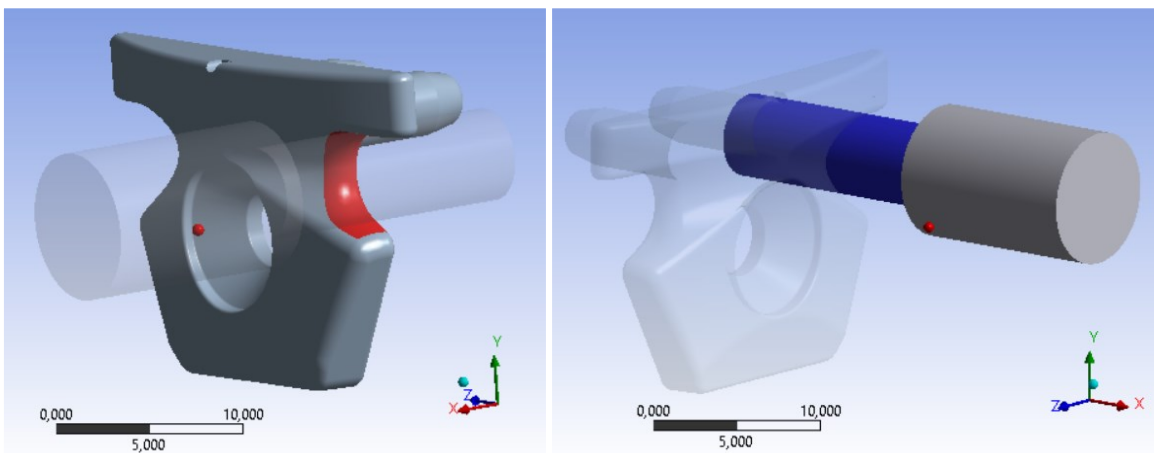


Figure 4.29: assembly created in SpaceClaim with the introduction of posterior pins, for ski touring binding configuration

## 4.2.2 Assembly management on Ansys Mechanical

Switching to Ansys Mechanical, materials are assigned as in the previous sub-chapter: the shell is assigned polymer material, while the inserts and rear pins are assigned structural steel.

Moving on to contact management, those between the two inserts and the shell were managed in the same way as described in *section 4.1.3* for the hybrid configuration, applying bonded contacts. With this ski touring binding configuration, the software detects two new contacts for each pin: the one between the pin and the posterior insert and the one between the pin and the heel of the shell. Since it was noted in the experimental tests that the posterior pins are only in contact with the rear insert and not with the heel of the shell, the contacts between pins and shell were suppressed in the FEM simulation. As regards the contacts between the pins and the posterior insert, a 'Frictional' contact with a friction coefficient of 0.6 has been set.



Figures 4.30-4.31: surfaces involved in frictional contact, for ski touring binding configuration: in red those of the rear insert, in blue those of the posterior pin

Moving on to definition of loads and constraints, rotation of five or ten degrees is always imposed via remote point to the front insert seats (as in *section 4.1.3*) while 'Fixed Support' in this case is applied to the rear faces of the pins (*figure 4.32*), in order to simulate the interlocking with which they are constrained on the L-beam.

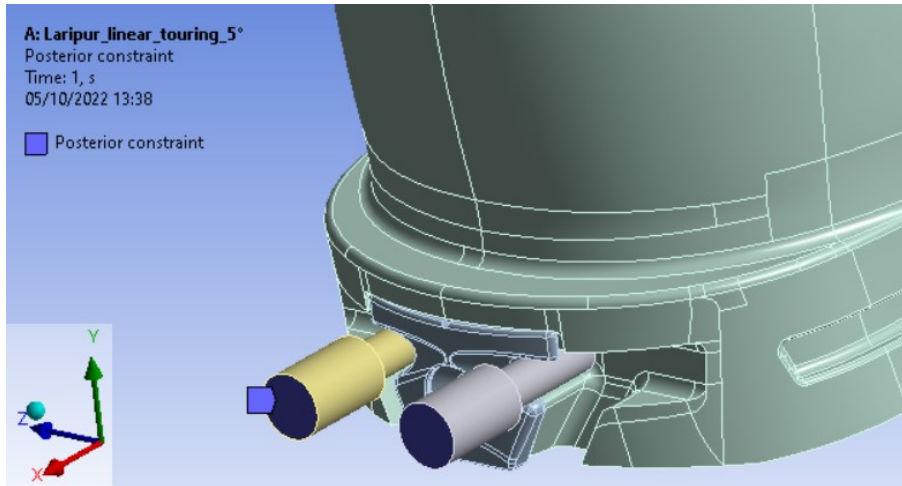


Figure 4.32: faces on which the fixed support boundary condition is applied, for ski touring binding configuration

Also in this case, the possibility of the rear grip to translate in the X-direction was taken into account by leaving the displacements in that direction free in the application of remote displacement.

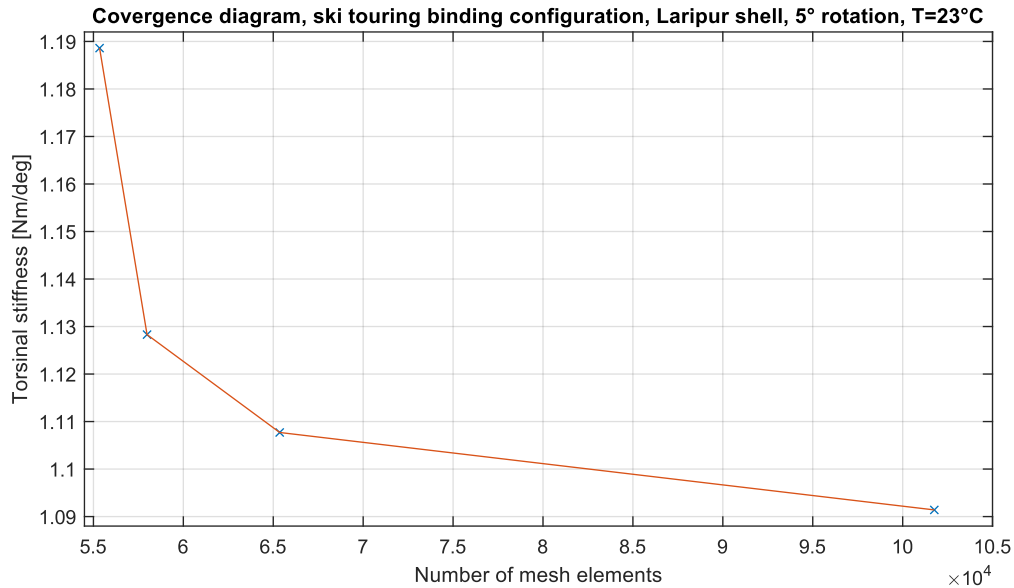
Also in this model, the mesh was set up with tetrahedral elements (Tet10), the torsional stiffness was calculated from the moment reaction probe applied to the 'Posterior constraint' (figure 4.32) and 'Large Deflection' were turned on in the analysis settings.

#### 4.2.3 Convergence of numerical simulation

A mesh convergence analysis was also carried out for this configuration of ski bindings, starting with an element size of 19 millimetres and progressively reducing it. The results obtained for the Laripur shell, applying a rotation of five degrees, are shown in table 4.5 and the convergence diagram is represented in figure 4.33. Formula 4.1 was used to calculate the percentage variation.

FEM, ski touring binding configuration, Laripur shell, 5° rotation, T=23°C					
Element size	Number of elements	Moment reaction	Torsional stiffness	Pct var	Time sol.
19	55342	5,943	1,1886		921
14	57982	5,641	1,1283	5,3%	1024
9	65358	5,539	1,1077	1,9%	1463
5	101762	5,457	1,0914	1,5%	1843
mm		Nm	Nm/deg		s

Table 4.5: stiffnesses obtained from numerical simulations for the Laripur shell by applying five degrees of rotation and progressively reducing the size of the mesh elements, for ski touring binding configuration



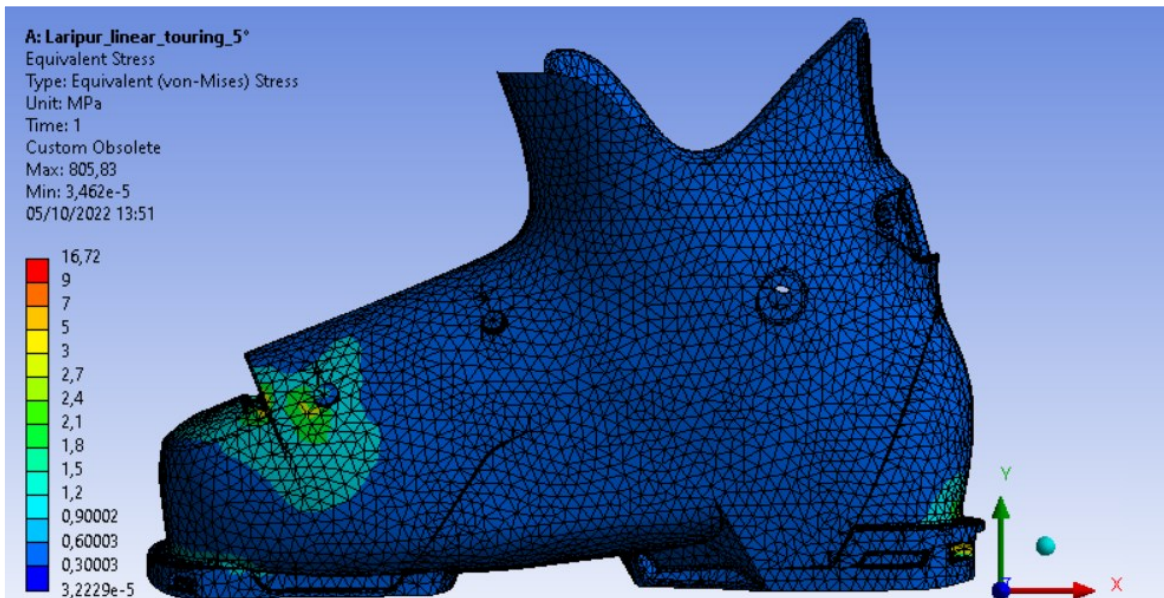
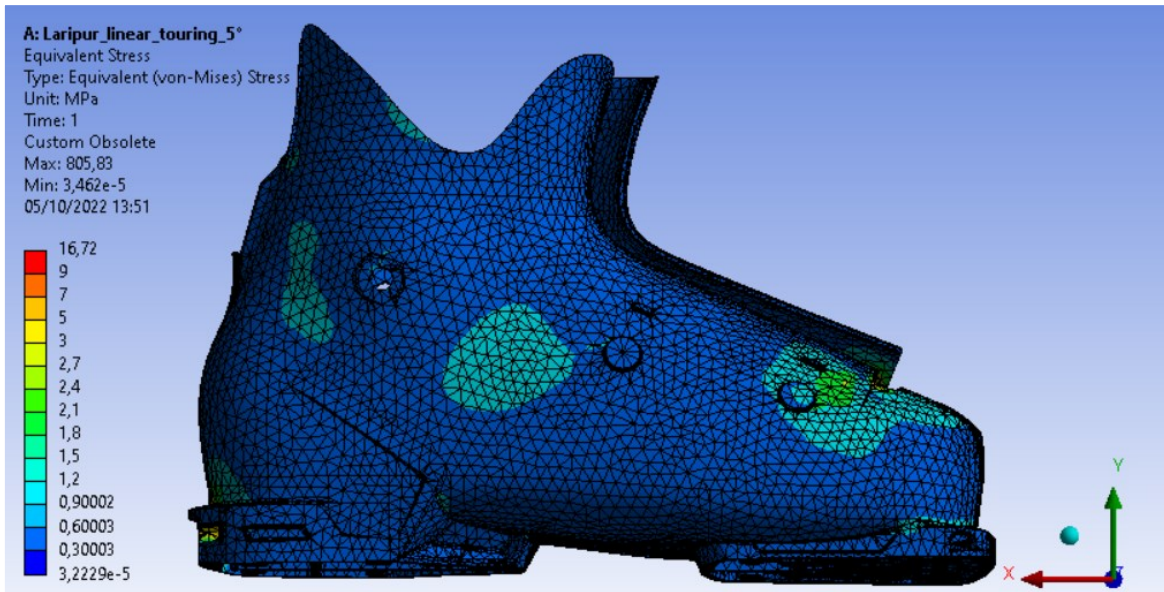
Figures 4.33: Laripur shell torsional stiffness convergence diagram for an imposed rotation of five degrees, for ski touring binding configuration

It can be concluded that, even with this configuration of ski bindings, convergence is achieved with a mesh element size of five millimetres (similar diagrams were obtained for all three materials and for both five and ten degrees of rotation). As a result, even for the FEM models relating to the configuration with ski touring bindings, the mesh used consist of tetrahedral elements (Tet10) with an element size of five millimetres.

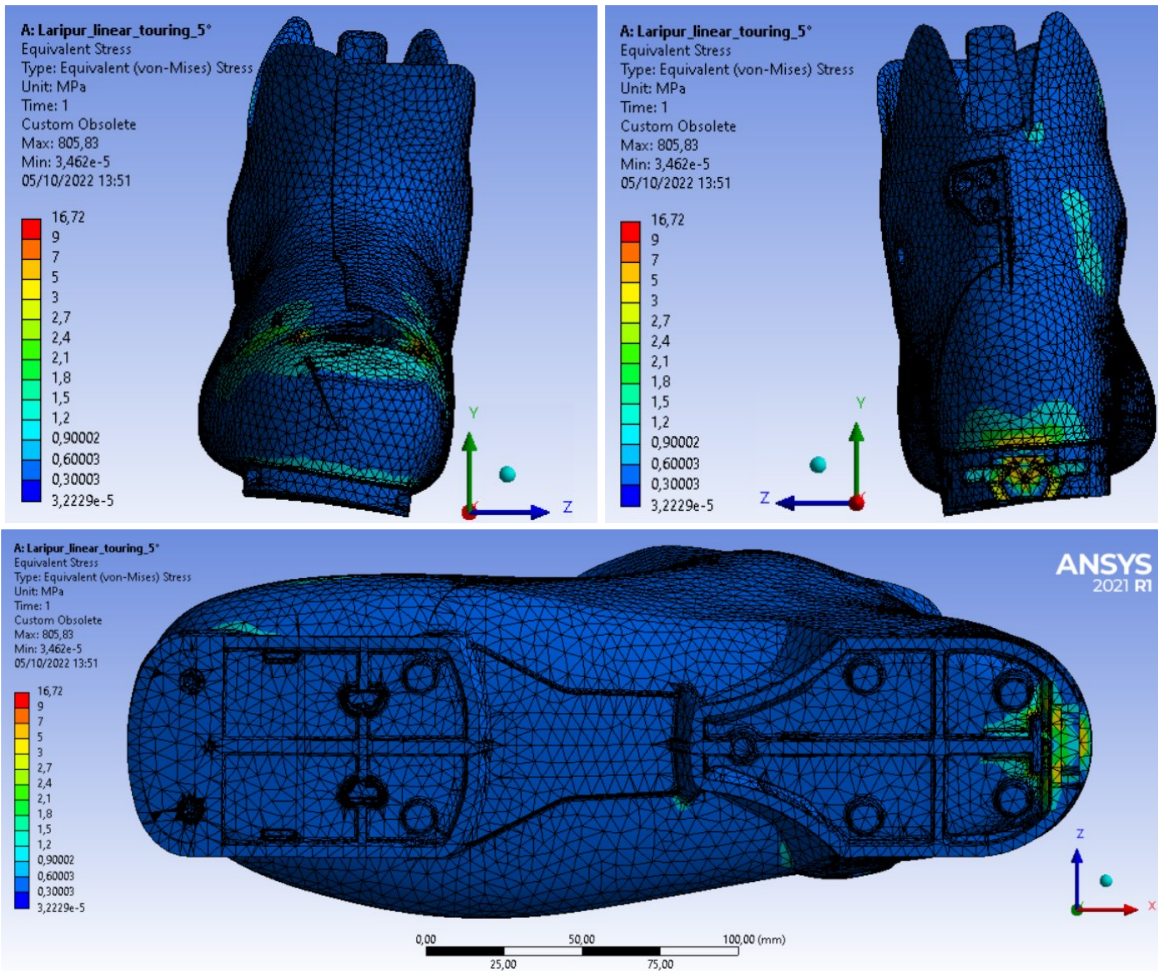
#### 4.2.4 Result of numerical torsion simulations

With the procedure explained in the previous paragraph, imposing a rotation of five degrees on the shell in Laripur results in a reaction moment in the X-direction of 5.501 Nm, giving a torsional stiffness of 1.100 Nm/deg. To give an idea of the stress distribution, colour maps of the equivalent Von Mises stress on the shell are shown in the figures below (being a polymeric material, it is theoretically not correct to take into account the equivalent Von Mises stresses, but these colour maps nevertheless allow a visualisation of the most stressed areas of the shell).





Figures: 4.34-4.35: front and back view views of the colour map of Von Mises' equivalent stress for the Laripur shell, imposing a torsion of five degrees, for ski touring bindings configuration



Figures: 4.36-4.37-4.38: other views of the colour map of Von Mises' equivalent stress for the Laripur shell, imposing a torsion of five degrees, for ski touring bindings configuration

A comparison of the Von Mises equivalent stress colour maps obtained with the two different ski bindings configurations shows that, with the ski touring configuration, the shell is less stressed overall (the same stress scales as the *figures 4.22, 4.23, 4.24, 4.25 and 4.26* of the previous sub-chapter were used). This is because the posterior ski touring constraint is less rigid and therefore allows greater rotation of the rear portion of the shell (as can be seen by comparing *figures 4.25 and 4.37*); consequently, in order to achieve five degrees of rotation around the X-axis, it will be necessary to apply less torque, so the stresses in the shell will also decrease.

If we compare *figures 4.26 and 4.38*, we can see the different position in which the stresses are concentrated due to the rear constraint; in particular, since the constraint is very localised in the case of the ski touring binding, there is a much greater concentration of stresses in the heel area of the shell where the rear insert is to be inserted. In fact, since the rear pins are the only constraint, and since they are only in contact with the posterior insert, it is logical to expect high stresses in this area, as can be seen in *figure 4.39*, where the rear pins and inserts have been activated (in the other figures, all the elements of the assembly except the shell had

been hidden in order to adapt the legend to the much lower stresses developed on the polymer material).

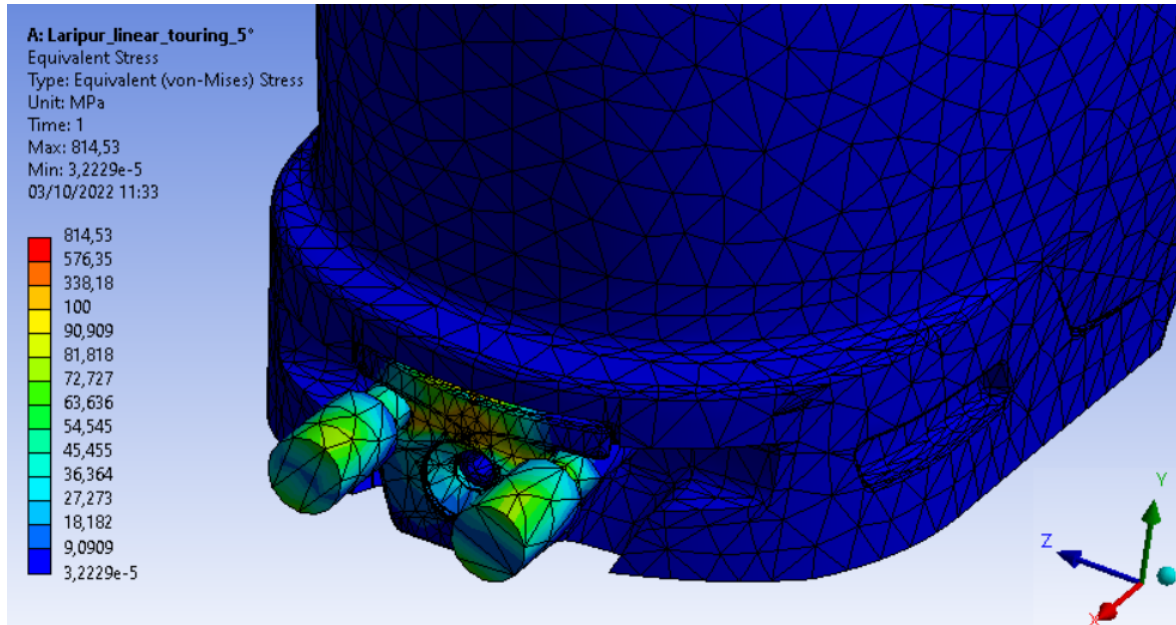


Figure 4.39: colour map of the stresses on the pins and rear insert in the case of ski touring constraint

The torsional stiffnesses obtained in numerical torsion simulations and the comparison with the experimental ones (*formula 4.2* was used to calculate the percentage variation) are shown in *table 4.6*.

Comparison of torsional stiffness, ski touring configuration, T=23°C				
Material	Rotation	Experimental	Numerical	Num pct var
Laripur	5	1,125	1,091	-3,0%
	10	1,003	1,108	10,4%
Elastollan	5	1,471	1,747	18,8%
	10	1,423	1,781	25,1%
	deg	Nm/deg	Nm/deg	

Table 4.6: comparison of torsional stiffnesses obtained experimentally and numerically, for ski touring bindings configuration

As can be seen, in this case the torsional stiffness obtained numerically for the Laripur shell is very close to that obtained experimentally, for an imposed rotation of five degrees, while the difference increases, although it remains good, for an imposed rotation of ten degrees. In the case of the Elastollan shell, on the other hand, it is observed that the difference between experimental and numerical results becomes greater and therefore the estimated stiffnesses are not as good, in particular for an imposed torsion of ten degrees.

Also in this case, as for the hybrid configuration of ski bindings, the differences between the experimental and numerical stiffnesses increase from five to ten degrees of imposed rotation. In particular, it can be seen from *table 4.7* (*formula 4.3* was used to calculate the ratio) that due to the non-linear effects present in the FEM

simulation (contacts between various elements of the assembly and large deflections), the stiffness obtained from the numerical simulations increases going from five to ten degrees of imposed rotation, instead of decreasing as in the experimental tests.

Torsional stiffness ratio, ski touring configuration, T=23°C			
Material	Rotation (deg)	Experimental	Numerical
Laripur	5	1	1
	10	0,892	1,015
Elastollan	5	1	1
	10	0,968	1,019

Table 4.7: torsional stiffness compared to those obtained for five degrees of imposed rotation, for ski touring bindings configuration

Once more, the difference in the behaviour of the FEM model from that of the real shell could be due to non-linear material behaviour, which could particularly involve the heel area of the shell, where there are higher stress concentrations.

#### 4.2.5 Comments on the results of numerical torsion simulations

Although the results for numerical torsion simulations with ski touring bindings deviate more from those obtained experimentally, we can observe from *table 4.8* that the numerically estimated changes in torsional stiffness when switching from the hybrid ski binding configuration to the ski touring configuration are similar to those measured experimentally.

$$\text{Stiffness reduction } (\Delta k) = \frac{k_{\text{tou}} - k_{\text{hyb}}}{k_{\text{hyb}}} \cdot 100 \quad \text{Formula (4.4)}$$

$$\text{Num. variation} = \frac{\Delta k_{\text{num}} - \Delta k_{\text{exp}}}{\Delta k_{\text{exp}}} \cdot 100 \quad \text{Formula (4.5)}$$

Comparison of torsional stiffness reduction, T=23°C				
Material	Rotation (deg)	Experimental	Numerical	Num Variation
Laripur	5	-60,9%	-62,6%	2,8%
	10	-62,4%	-60,1%	-3,7%
Elastollan	5	-69,2%	-64,8%	-6,4%
	10	-66,6%	-62,4%	-6,3%

Table 4.8: comparison of torsional stiffness reduction obtained from experimental tests and numerical simulations when switching from hybrid ski binding configuration to ski touring configuration

Therefore, even if they are not as accurate as the numerical simulations with the hybrid ski binding configuration, the simulations for the ski touring configuration are still realistic. The major differences between numerical simulations and experimental tests obtained for the ski touring configuration are probably due to the greater complexity of the rear constraint and the small clearances that are present between pin and posterior insert in reality.

In any case, it was necessary to carry out new experimental tests to also obtain the elastic modulus of the Grilamid mixture, and therefore tests were also repeated for the Laripur and Elastollan mixture.

### 4.3 Torsion numerical simulations with updated elastic moduli

New specimens were moulded for each of the three shell materials and the material characterisation tests were repeated. Numerical simulations were then performed by updating the elastic moduli in 'Engineering Data' and the torsional stiffnesses obtained were compared with those obtained experimentally

#### 4.3.1 Company testing of material properties

At the company, the mechanical properties of materials are obtained by means of three-point bending test performed in accordance with European standard EN ISO 178: *a test specimen of rectangular cross-section, resting on two supports, is deflected by means of a loading edge on the specimen midway between supports* [11]. The specimens nominally have a length  $l = 80 \text{ mm}$ , a width  $b = 10 \text{ mm}$  and a thickness  $h = 4 \text{ mm}$  and are placed on two supports placed at a distance  $L = 64 \text{ mm}$ .

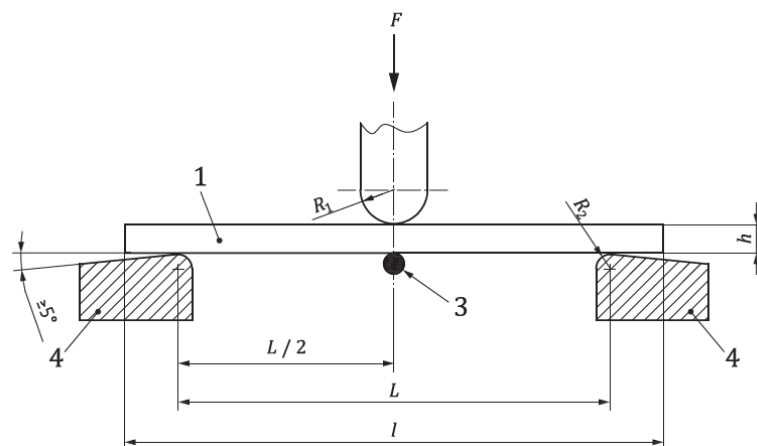


Figure 4.40: positioning of the test specimen (1) on the supports (4) for the three-point bending test according to EN ISO 178 [11]

Ten injection-moulded specimens are taken for each material and their actual dimensions are measured before placing them in the test machine. We then load the specimen with a loading edge, performing a test in deformation control at a speed  $v = 2 \text{ mm/min}$ .



Figure 4.41: testing machine used in the company for the three-point bending test

From the applied force and the displacement of the loading edge, the strain ( $\varepsilon$ ) and stress ( $\sigma$ ) of the specimen in the mid-section are derived:

$$\varepsilon = \frac{6 \cdot s \cdot h}{L^2} \quad \text{Formula (4.6)}$$

$$\sigma = \frac{3 \cdot F \cdot L}{2 \cdot b \cdot h^2} \quad \text{Formula (4.7)}$$

Where  $F$  is the applied force (in newton),  $L$  is the span (in millimetres),  $b$  is the width (in millimetres),  $h$  is the thickness (in millimetres) and  $s$  is the deflection (in millimetres).

Then the elastic flexural modulus (EFM) of the material is obtained by evaluating the stresses  $\sigma_1$  and  $\sigma_2$  present in the centre of the specimen for a strain  $\varepsilon_1 = 0.05\%$  and  $\varepsilon_2 = 0.25\%$ :

$$EFM = \frac{\Delta\sigma}{\Delta\varepsilon} = \frac{\sigma_2 - \sigma_1}{\varepsilon_2 - \varepsilon_1} \quad \text{Formula (4.8)}$$

For each material, the average of the elastic flexural moduli obtained from the ten specimens was calculated and the results are shown in *table 4.9*.

EFM at 23°C, testing date 04/07/22			
Material	Average EFM	Minimum EFM	Maximum EFM
Laripur 6650	291	281	299
Grilamid mixture	462	433	478
Elastollan mixture	633	586	674
	MPa	MPa	MPa

Table 4.9: average, minimum and maximum elastic flexural modulus for the three shell materials, obtained from three-point bending tests on 04/07/2022

To obtain an estimate of the elastic modulus of each material, the average of those obtained from ten specimens is calculated because injection moulding process causes a certain variability of mechanical properties between the various parts produced, even if they are nominally the same. This can be seen by observing, in *table 4.9*, the variations between the minimum and maximum values of elastic flexural modulus that were obtained for each material.

*Table 4.10* shows the comparison between the elastic flexural moduli obtained and those in the Tecnica data sheet.

$$\text{Percentage var.} = \frac{EFM_{new} - EFM_{datasheet}}{EFM_{new}} \quad \text{Formula (4.9)}$$

Comparison between average EFM at 23°C			
Material	EFM (data sheet)	EFM (07/07/22)	Percentage variation
Laripur 6650	340	291	-16,8%
Grilamid mixture	/	462	/
Elastollan mixture	590	633	6,8%
	MPa	MPa	

Table 4.10: comparison between the elastic flexural moduli provided by the previous Tecnica data sheets and those obtained through the new material characterisation tests

These variations in elastic modulus could be due to changes in the composition of the materials supplied or to different parameters of the injection moulding process of the specimens. Since we cannot know which of the two elastic modulus estimates is more correct, we take the last characterisation made as the correct one.

#### 4.3.2 Torsion numerical simulations with updated average elastic flexural moduli

The numerical torsion analyses from *sub-chapters 4.1* and *4.2* were resumed and the Young's moduli of the three polymer materials were updated in 'Engineering Data' (*figure 4.1*). Then the numerical analyses were re-executed, the reacting moments at the constrained surfaces were derived and the new torsional stiffnesses calculated (*tables 4.10* and *4.11*).

As can be seen from *table 4.11*, good results are obtained for the hybrid configuration of ski bindings for all three materials. In fact, there are percentage variations in torsional stiffness between numerical simulations and experimental

tests of less than 15% (calculated using *formula 4.2*), with the only exception for the ten-degree torsion of the Elastollan shell where the variation is a little higher, but still acceptable.

<b>Comparison of torsional stiffness, hybrid configuration, T=23°C</b>				
<b>Material</b>	<b>Rotation</b>	<b>Experimental</b>	<b>Numerical</b>	<b>Num pct var</b>
Laripur	5	2,876	2,508	-12,8%
	10	2,670	2,390	-10,5%
Grilamid	5	3,658	3,918	7,1%
	10	3,349	3,741	11,7%
Elastollan	5	4,772	5,311	11,3%
	10	4,255	5,067	19,1%
	deg	Nm/deg	Nm/deg	

Table 4.11: comparison of torsional stiffnesses obtained experimentally and numerically with updated average elastic flexural moduli, for hybrid ski binding configuration

Turning to *table 4.12*, it can be seen that, even for the ski touring binding configuration, good results are obtained from the numerical simulations for the Laripur and Grilamid shells: the percentage change in torsional stiffness compared to that obtained from the experimental tests is always less than 16%. For Elastollan shell, on the other hand, the results obtained are not good as the percentage variations are greater than 25% for both imposed rotations.

<b>Comparison of torsional stiffness, ski touring configuration, T=23°C</b>				
<b>Material</b>	<b>Rotation</b>	<b>Experimental</b>	<b>Numerical</b>	<b>Num pct var</b>
Laripur	5	1,125	0,952	-15,4%
	10	1,003	0,965	-3,8%
Grilamid	5	1,292	1,422	10,0%
	10	1,264	1,446	14,4%
Elastollan	5	1,471	1,853	26,0%
	10	1,423	1,889	32,8%
	deg	Nm/deg	Nm/deg	

Table 4.12: comparison of torsional stiffnesses obtained experimentally and numerically with updated average elastic flexural moduli, for ski touring binding configuration

Comparing *tables 4.11* and *4.12* with *tables 4.3* and *4.6* respectively, it can be observed that with the new elastic flexural moduli, the percentage variations between numerical simulations and experimental tests increased. This is due to the fact that, in particular, the elastic modulus of Laripur decreased significantly, while that of Elastollan increased (*table 4.10*).

In addition to these variations between different batches of specimens, even among the ten specimens of the last characterisation there is some variability in the elastic moduli due to the injection moulding process by which they are produced, as can be seen in *table 4.9*. As these variations in mechanical properties occur between specimens of the same batch, variations in torsional stiffness are likely to occur between several shells of the same material, as they suffer from the same variability



generated by the injection moulding process and have a much more complex shape than the specimens. For this reason, FEM simulations were repeated by entering the minimum and maximum values of the elastic flexural moduli and the result obtained are shown in *tables 4.13* and *4.14*.

<b>Comparison of torsional stiffness, hybrid configuration, T=23°C</b>					
Material	Rotation	Experimental	EFM assigned	Numerical	Num pct var
Laripur	5	2,876	min	2,425	-15,7%
			max	2,575	-10,5%
	10	2,670	min	2,311	-13,4%
			max	2,454	-8,1%
Grilamid	5	3,658	min	3,680	0,6%
			max	4,049	10,7%
	10	3,349	min	3,513	4,9%
			max	3,866	15,4%
Elastollan	5	4,772	min	4,929	3,3%
			max	5,643	18,2%
	10	4,255	min	4,701	10,5%
			max	5,385	26,6%
	deg	Nm/deg		Nm/deg	

Table 4.13: comparison of the torsional stiffnesses obtained from numerical simulations, including the minimum and maximum EFM values obtained, with those derived experimentally, for the hybrid ski binding configuration

<b>Comparison of torsional stiffness, ski touring configuration, T=23°C</b>					
Material	Rotation	Experimental	EFM assigned	Numerical	Num pct var
Laripur	5	1,125	min	0,923	-18,0%
			max	0,975	-13,3%
	10	1,003	min	0,936	-6,7%
			max	0,989	-1,4%
Grilamid	5	1,292	min	1,345	4,1%
			max	1,464	13,3%
	10	1,264	min	1,368	8,2%
			max	1,489	17,8%
Elastollan	5	1,471	min	1,737	18,1%
			max	1,951	32,7%
	10	1,423	min	1,771	24,4%
			max	1,991	39,9%
	deg	Nm/deg		Nm/deg	

Table 4.14: comparison of the torsional stiffnesses obtained from numerical simulations, including the minimum and maximum EFM values obtained, with those derived experimentally, for the ski touring binding configuration

### 4.3.3 Conclusions

Theoretically, the results obtained from the experimental tests should be intermediate between those obtained numerically with the minimum and the

maximum elastic modulus measured. This is not actually the case, but certain phenomena must also be considered:

- The first is that, just as the elastic modulus varies between the various moulded specimens, there will also be variability in the torsional stiffnesses between the various shells moulded from the same material. Hence, the torsional stiffnesses obtained experimentally for the three shells tested (one per material) could lie towards one or other end of the numerically estimated range. One possibility for further study would be to repeat the bench tests on several shells of the same material and see how much the obtained torsional stiffnesses vary.
- The second is that, since the shell has a much more complex geometry, it is difficult for the parameters of the injection moulding process to be the same as those of the test specimens and therefore there can be variations in the elastic modulus of the material between the test specimens and the shell.
- The third is that, since the shell has a complex geometry, extracting specimens in different areas would result in different elastic moduli because, during the injection moulding process, the temperatures, pressures and consolidation times of the molten polymer material will not be the same throughout the mould.
- The fourth is that there will be some uncertainty in the repeatability of the tests performed on the torsion bench, probably higher for the ski touring bindings configuration since the rear constraint is much more localised and complex, and therefore more sensitive to different 'pin' placements in the rear insert. One possibility for further study would be to carry out several tests with the same shell for both configurations of ski bindings and observe how much the obtained torsional stiffnesses vary.
- The fifth is that on the experimental tests, the shell material probably behaves in a non-perfectly linear way (since they are polymeric materials already at low deformations, they may switch from the linear elastic to the non-linear elastic section of the stress-strain curve), whereas in the numerical simulations linear elastic behaviour was set. This difference becomes more relevant as the deformation increases and could explain the larger deviations between numerical simulations and experimental tests for imposed rotations of ten degrees. To further the study, the entire stress-strain curves for each material could be obtained from the specimens and entered into the 'Engineering Data' window of the numerical simulations.
- The last is that there is an ineradicable difference between the results of numerical simulations and experimental results, especially considering the complexity of the shell geometry.

Taking all these observations into account, obtaining percentage differences of less than 15% between numerically and experimentally obtained torsional stiffnesses is a good result. Laripur is the material for which the results obtained are the least strong, but if the shell material had a modulus close to the minimum found in the characterisation tests, the result obtained would still be fair.

Finally, when comparing the reduction in stiffness that occurs when switching from hybrid to ski touring binding configuration (calculated using *formula 4.4* and *4.5*), it can be seen that the difference between numerical simulations (with the average flexural modulus) and experimental tests is always less than 6%, as shown in *table 4.15*.

<b>Comparison of torsional stiffness reduction, T=23°C</b>				
<b>Material</b>	<b>Rotation (deg)</b>	<b>Experimental</b>	<b>Numerical</b>	<b>Num Variation</b>
Laripur	5	-60,9%	-62,0%	1,9%
	10	-62,4%	-59,6%	-4,5%
Grilamid	5	-64,7%	-63,7%	-1,5%
	10	-62,3%	-61,3%	-1,5%
Elastollan	5	-69,2%	-65,1%	-5,9%
	10	-66,6%	-62,7%	-5,8%

Table 4.15: comparison of torsional stiffness reduction obtained from experimental tests and numerical simulations when switching from hybrid ski binding configuration to ski touring configuration



## Chapter 5: Shell tip impact test

This chapter will first present the company's standard for the tip impact resistance of shells and then move on to the tests performed at the drop tower to attempt to achieve shell fracture of all three materials, in order to obtain the limiting impact energy and the corresponding force, deformation and speed trends over time for each.

### 5.1 Company standard for shell tip impact resistance

In order to assess the tip impact resistance of a ski boot shell, a specific impact testing machine is used in Tecnica: a Fractovis Ceast (*figure 5.1*).



Figure 5.1: Fractovis Ceast machine for impact tests

The samples to be tested must have been produced at least *24 hours* earlier and must be appropriately conditioned according to the company's standard procedure. In the case of homologation tests, at least six samples per model, size and material shall be tested. In particular, since the Markab shells to be tested are adult and size 265, they will be subjected to an impact energy of *70 joules*.

Before testing, the samples must be refrigerated for at least six hours at  $-20^{\circ}\text{C}$  with the soles already screwed down (*figure 5.2*) and the shell clamping machine equipment must be set up correctly.



Figure 5.2: shell with the soles attached by screws

The inclination of the plane on which the sole of the shell will rest is  $65^\circ$  with respect to the horizontal (*figure 5.3*) and, using a shell at room temperature of the same model and size as those to be tested, the position of the heel bracket is adjusted by means of a specific screw (*figure 5.4*).

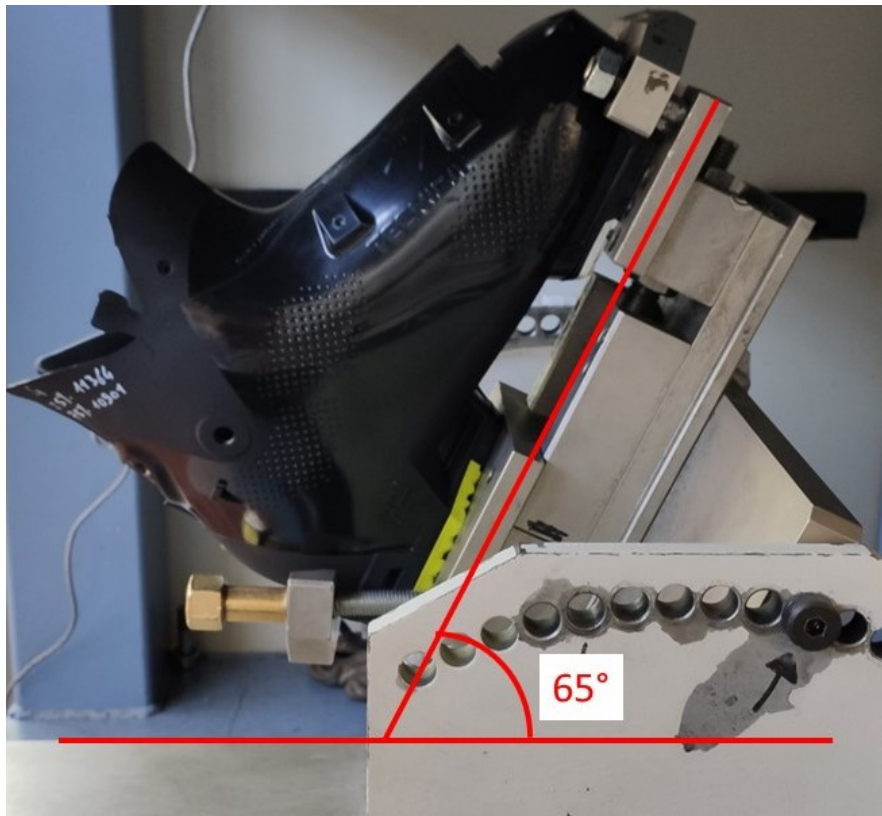
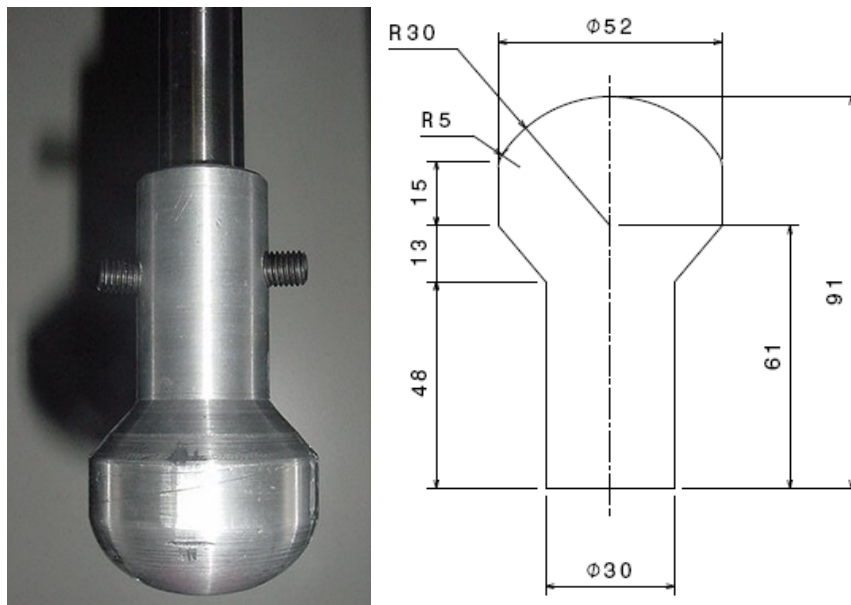


Figure 5.3: inclination of the plane on which the shell rests for the impact test



Figure 5.4: brackets that fix the tip and heel of the shell for the impact test; the red arrow indicates the screw that allows the distance between the two brackets to be adjusted to suit the length of the shell

The impactor used is made of aluminium and its geometry is shown in the figures below.



Figures 5.5-5.6: geometry of the impactor used for impact tests

Once the brackets have been adjusted according to the length of the shell to be tested, the impactor is slowly lowered until it comes into contact with the tip of the

shell. Then, laterally we check that the point of contact is at the apex of the curvature of the tip (*figure 5.7*) and frontally we check that the point of contact is central to the width of the tip (*figure 5.8*). If not, adjust the positioning of the base by unscrewing and retightening the screws that secure it.



Figures 5.7-5.8: the point of contact between impactor and shell is located laterally at the apex of the curvature of the tip and frontally at the centre of the width of the tip

It must therefore be ensured that to the mass of the sled ( $2.90\text{ kg}$ ), the stem ( $1.033\text{ kg}$ ) and the impactor ( $0.23\text{ kg}$ ),  $3\text{ kg}$  are added from additional weights (*figure 5.9*), so that by starting the impactor from  $1\text{ m}$  above the tip of the shell, the impact energy is approximately  $70\text{ joules}$ :

$$\begin{aligned} \text{Impact energy} &= m \cdot g \cdot h \\ &= (2.90 + 1.033 + 0.23 + 3) \cdot 9.81 \cdot 1 \\ &= 70.27\text{ J} \end{aligned} \quad \text{Formula (5.1)}$$



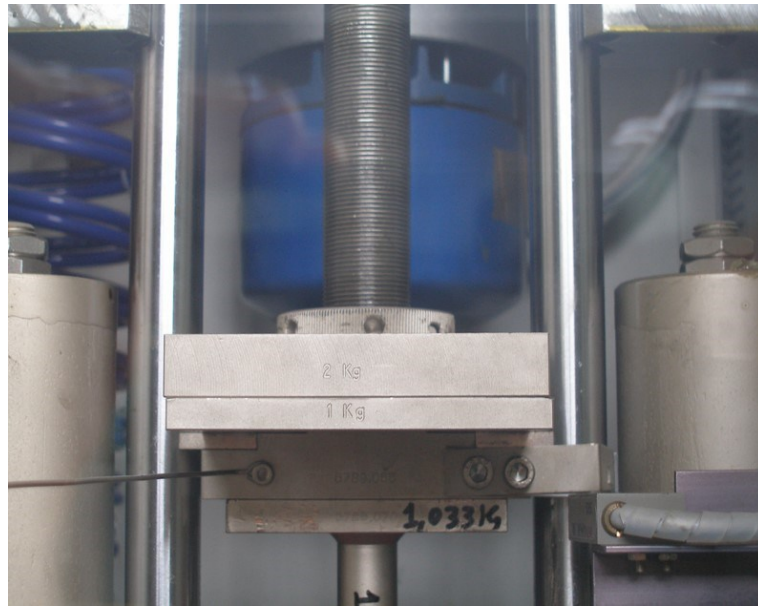


Figure 5.9: additional masses placed on the sled in order to achieve an impact energy of 70 joules

Once the equipment setup is correct, the first shell to be tested is taken from the freezer, the heel and then the toe are fixed in the appropriate brackets, and the test is carried out: the impactor is brought to a height of one metre and then dropped so that it impacts the tip of the shell in the predetermined position; it is then checked whether or not the shell has broken. The model can be homologated if the number of broken shells is less than 17%.

## 5.2 Instrumented impact tests on Fractovis

In order to carry out numerical simulations of impact tests, it is necessary to extract as many quantities as possible from the impact test, in particular the force transmitted by the impactor to the shell over time, the displacement of the impactor over time and the speed at which the impactor hits the tip of the shell. The impact speed and the force trend over time could be used to impose the load in the numerical simulation, while the displacement over time could be used to verify that the shell model, in the simulation, deforms in a similar way to what occurs in the real impact test.

### 5.2.1 Instrumented stem

In order to derive this data from the impact tests, the instrumented stem supplied with the Fractovis drop test machine was used (*figure 5.10*).



Figure 5.10: instrumented stem of Fractovis drop test machine

This stem is equipped with a load cell to output the force trend over time and, by integration of this signal, the trends in displacement and energy over time. The machine is also equipped with an optical fork to detect the speed of the impactor at the instant it makes contact with the shell and then, from this initial value, the speed trend over time is obtained by integration of the force signal detected by the load cell. As it had never been used before, the correct functioning of the stem sensors was verified by means of some pilot tests.

The aluminium impactor was then mounted on the instrumented stem and the tests were repeated with the same starting masses and heights as in the previous pilot tests (except for the 0.23 kg impactor mass). With this configuration, graphs were obtained for similar impact energies that were very different from the previous ones and it therefore seemed that there was some problem. When analysing the geometry of the instrumented stem and the impactor mounting system, it was observed that the grub screw (*figure 5.5*) was tightening the stem above the fifteen-millimetre end section (*figure 5.11*), where the sensors are positioned. As a result, part of the force was transferred above the load cell, and this generated the noted issues.



Figure 5.11: dimensions of the end of the instrumented stem

It was not possible to use the instrumented stem alone (without impactor) because it has a 10 *millimetre* radius at the end, as opposed to the 26 *millimetre* radius of the impactor, and therefore the test conditions would have been much more severe than those of the standard impact tests in the company. Consequently, a new steel impactor was designed (*figure 5.12*) in order to have an end radius that was similar to that of the aluminium one, and a fastening system by means of grub screws that would fix it to the stem in the 5 *millimetre* cylindrical section of the end portion (*figure 5.11*).



Figure 5.12: new steel impactor to be fixed above the instrumented stem

Pilot tests were carried out with this new impactor and it was observed that the graphs obtained were correct and similar to those obtained with the instrumented stem alone, although vibrations are generated as a result of the impactor mass

positioned at the end of the stem (it is like having a beam with a mass concentrated at the end which, due to the impact force, begins to vibrate axially).

The data obtained from the instrumented impact tests can be exported from the computer associated with the Fractovis machine in a TXT file and can then be processed using a Matlab script in order to obtain graphs of the various quantities over time.

### 5.2.2 Shell breaking impact tests

The ultimate aim of numerical simulations of impact tests will be to understand whether or not at 70 *joules* the rupture of a certain shell model occurs. The first step will therefore be to increase the impact energies to the point of breaking the shells of the Markab model we are studying in order to observe what the failure mechanisms are and to derive, by means of the instrumented stem, the force trend over time. The first simulations that will be carried out will be static and we will impose the peak force detected by the stem, for the impact energy that caused the shell to break. The peak stresses or strain obtained will be measured and an attempt will then be made to define a limit magnitude beyond which shell failure occurs. Subsequently, we must move on to dynamic impact simulations with a different software from the one used so far in this work.

Instrumented impact tests will then have to be carried out, the aim of which will be to find, as accurately as possible, the critical energy (the lowest energy that would break the shell of each of the three materials of the Markab model) and to derive information on the impact speed, the measured peak force and the deformation of the shell tip.

Six Markab size 265 shells of each material were then placed in the freezer at  $-20^{\circ}\text{C}$ , with the soles already attached, and the test machine was prepared as previously explained in *subchapter 5.1*, according to the company's standard procedure. Therefore, for the six shells of each material, the tests were carried out following the scheme in *figure 5.13*, in order to define the critical impact energy, which is the lowest energy for which shell rupture is achieved. Theoretically impact energies were calculated as the potential energy of the system consisting of sled, instrumented stem, impactor and additional masses, considering the height of the impactor relative to the tip of the shell:

$$Theo I.E. = mass \cdot gravity\ acceleration \cdot height \quad \text{Formula (5.2)}$$

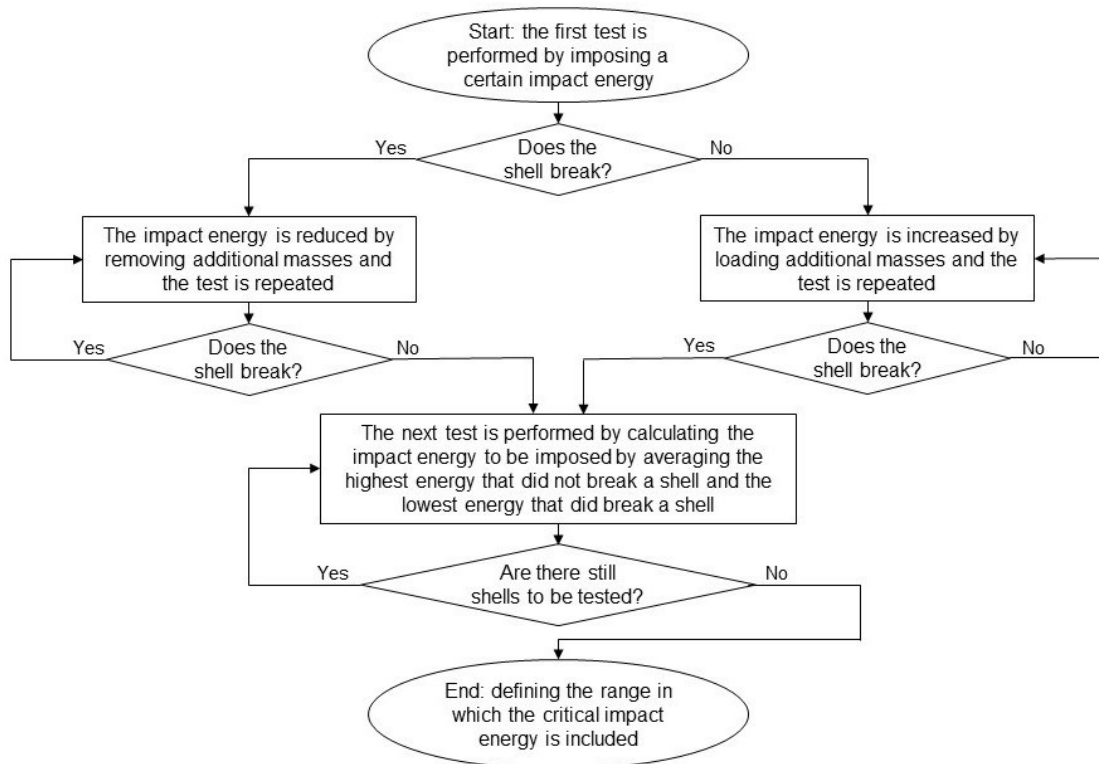


Figure 5.13: block diagram explaining the procedure followed to perform impact tests in order to identify the critical impact energy for each of the shell materials

The results obtained following this procedure are shown in the tables below.

Impact tests, Laripur shell, T=-20°C				
Test no.	Height	Mass	Theo. I. E.	Failure?
1	0,997	8,16	79,8	no
2	0,997	10,16	99,3	yes
3	0,997	9,16	89,6	no
4	0,997	9,63	94,2	no
5	0,997	9,63	94,2	yes
6	0,997	9,63	94,2	no
	m	kg	J	

Table 5.1: impact tests performed on Laripur shells

Impact tests, Grilamid shell, T=-20°C				
Test no.	Height	Mass	Theo. I. E.	Failure?
1	0,997	29,16	285,1	yes
2	0,997	19,16	187,3	no
3	0,997	24,16	236,2	yes
4	0,997	22,16	216,7	yes
5	0,997	20,16	197,1	no
6	0,997	21,16	206,9	no
	m	kg	J	

Table 5.2: impact tests performed on Grilamid shells

Impact tests, Elastollan shell, T=-20°C				
Test no.	Height	Mass	Theo. I. E.	Failure?
1	0,997	13,16	128,7	no
2	0,997	15,16	148,2	no
3	0,997	19,16	187,3	no
4	0,997	24,16	236,2	no
5	0,997	29,16	285,1	no
6	/	/	/	/
	m	kg	J	

Table 5.3: impact tests performed on Elastollan shells

As can be seen from *table 5.1*, for the Laripur shells, the critical impact energy should be around 94.2 *joules*, since in the three tests performed with that energy, the shell broke once and remained intact the other two times (it was not possible to perform the fifth test for an intermediate impact energy between 94.2 and 99.3 *joules* because additional available masses did not allow this). For Grilamid shells, on the other hand, as can be seen from *table 5.2*, the critical impact energy is between approximately 207 and 217 *joules*. For Elastollan shells, finally, we were not able to break any shells, even using all the additional masses available (in addition, for an impact energy of 285.1 *joules* the peak force values were close to the full scale of the load cell); therefore the critical impact energy will be more than 285 *joules*.

Once the critical fracture energies have been determined, safety coefficients can also be defined, safety factors can also be defined with respect to the company standard, which stipulates an impact energy of 70 *joules*:

$$\text{Safety factor} = \frac{\text{critical impact energy}}{\text{standard impact energy}} \quad \text{Formula (5.3)}$$

The safety factors obtained for each material are given in *table 5.4*.

Safety factors for impact test, T=-20°C			
Material	Critical I. E.	Standard I. E.	Safety factor
Laripur	94,2	70	1,3
Grilamid	≈ 211,8	70	≈ 3,0
Elastollan	> 285,1	70	> 4,1
	J	J	

Table 5.4: safety factors obtained for each shell material for tip impact tests

As can be seen from the table above, for the Laripur shell a safety factor of 1.3 is obtained, while for the other two materials very high safety factors are obtained: around 3 for Grilamid and more than 4.1 for Elastollan. This means that the Grilamid and Elastollan shells are excessively oversized for the company's safety standard for tip impacts, and the geometries could therefore be modified, compared to the current Markab model, in order to reduce thicknesses to make the shell lighter and therefore more performing (the weight of the shell is an important parameter). For this purpose, numerical impact simulations would be essential, which would make it

possible to verify that the new shell geometry with lightened thicknesses would break for impact energies of more than 70 joules with a certain safety factor.

Obviously, if the shell thicknesses were to be reduced, it would then be necessary to analyse the new performance of the modified models in terms of torsional and flexural stiffness (other important parameters expressing the performance of ski boots), which would certainly be reduced. A process of topological optimisation of the shells for materials with excessively high impact safety factors could then be implemented:

- The cad model of the shell is modified, reducing the thicknesses, particularly in the front area. Numerical impact simulations are then carried out with the new model to assess the impact energy that will break the shell. The model is then iteratively modified until a desired safety factor is obtained, compared to the 70 joules required by the standard impact test.
- Static torsion and bending simulations are carried out, similarly to what was done in Chapter 4, to assess the torsional and bending stiffness of the shells with the new geometry. If the stiffnesses are not sufficiently high, they will have to be increased appropriately by modifying the cad model and adding veins and other reinforcing elements where necessary.
- Finally, moulds must be made for injection moulding some prototypes of the new model, in order to experimentally verify that the impact resistance and torsional and flexural stiffnesses are as desired

This iterative process would then make it possible to obtain higher-performance shells, as they have lower weights for the same flexural and torsional stiffness and are able to pass safety standards for impact resistance.

This topological optimisation scheme should be effective in theory, but we must also take into account the costs associated with injection moulding: with this iterative process, a different shell geometry would be obtained for each material and therefore a customised mould would have to be made for each one, with all the associated costs (also taking into account all boot sizes). It is precisely for this reason that at the moment Markab shells in Laripur, Grilamid and Elastollan are all made with the same geometry, and since Laripur is the least performing material, it is an obvious consequence that for Grilamid and Elastollan, high impact safety factors are obtained. One solution could be to divide the materials into families according to mechanical properties and to use the same mould for a whole family of materials.

### **5.2.3 Analysis of data from impact tests**

At the end of each impact test, it is possible to export from the test machine a TXT file containing data relating to the force measured by the load cell and the energy, speed and displacement of the impactor, starting from the instant of first contact with

the tip of the shell. These data must then be processed using a Matlab script (given in *appendix B.2*) in order to obtain the graphs shown in the following figures (as an example, the graphs of the fourth test performed with the shell in Laripur, for an impact energy of 94.2 joules, are shown).

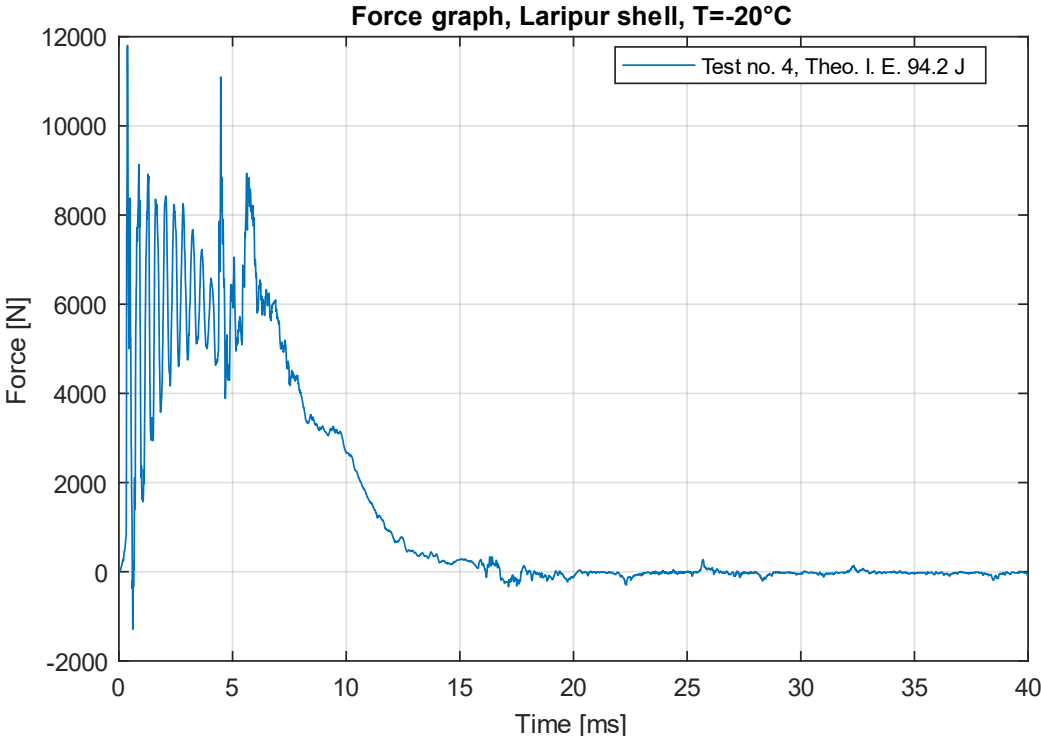


Figure 5.14: force graph for the fourth test performed on shells in Laripur

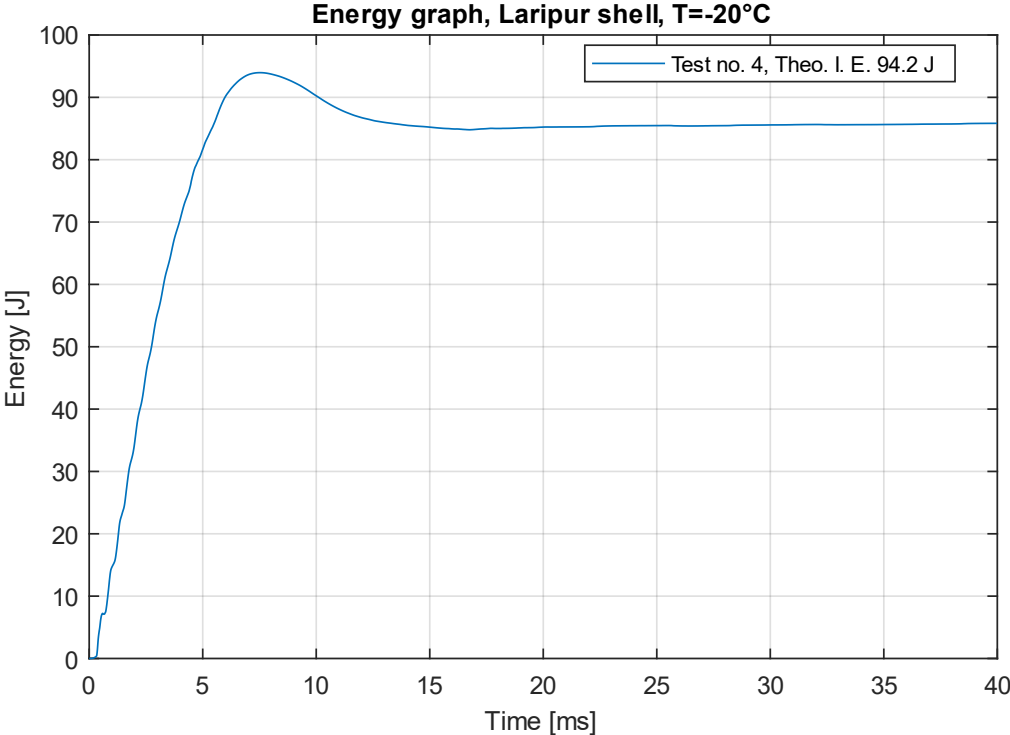


Figure 5.15: impactor energy graph for the fourth test performed on shells in Laripur



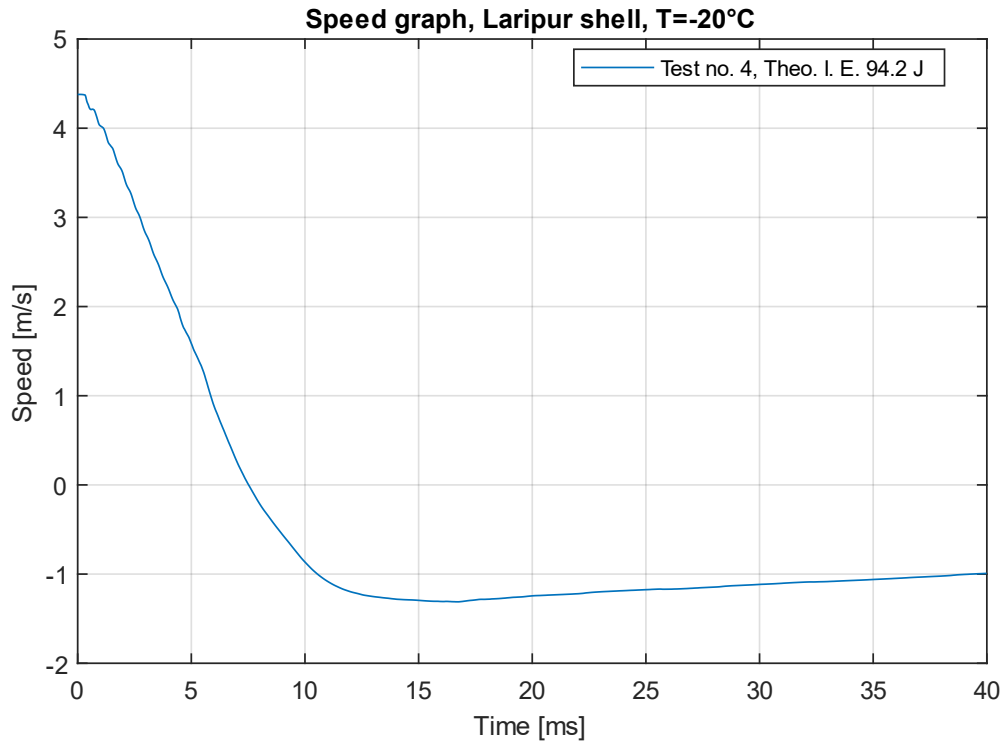


Figure 5.16: impactor speed graph for the fourth test performed on shells in Laripur

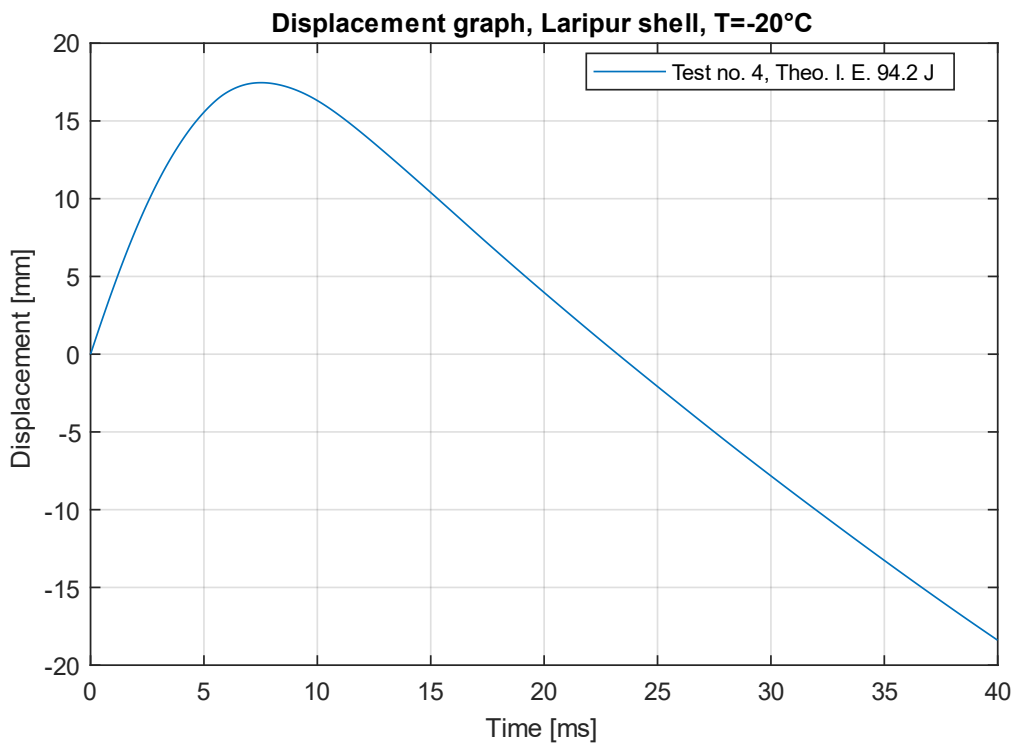


Figure 5.17: impactor displacement graph for the fourth test performed on shells in Laripur

It can be seen that all the graphs are fairly smooth, except for that of the force (*figure 5.14*), where it is possible to note considerable oscillations in the signal, particularly in the instants immediately following the start of contact between the shell and the impactor. If we zoom in on the graph (*figure 5.18*), we can see that the force

measured by the load cell has a first peak at  $0.37\text{ ms}$ , then it begins to oscillate and its value decreases, before reaching a second peak at  $4.48\text{ ms}$ .

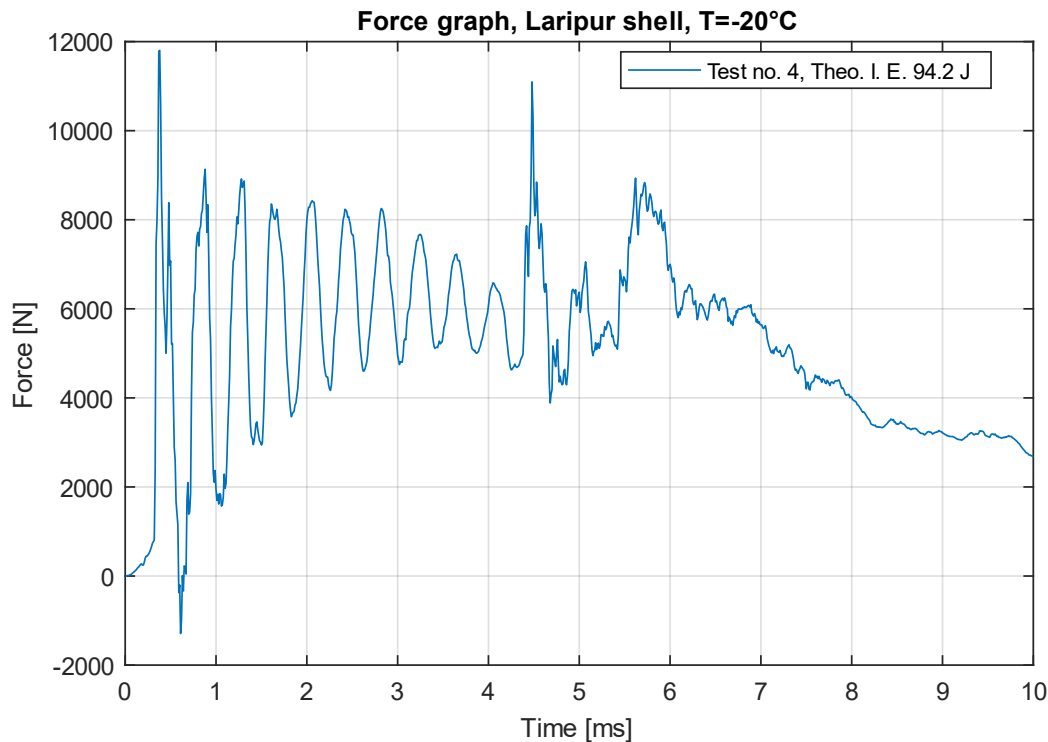


Figure 5.18: zoom of force graph for the fourth test performed on shells in Laripur

Watching the video of the impact at a slowed speed, it can be seen that after the impactor hits the shell, the tip of the shell begins to deform downwards very quickly and the contact force between the shell and the impactor then decreases. This phase lasts for about up to  $4\text{ milliseconds}$ , when the shell returns to offer greater resistance to the progress of the impactor and there is then a new increase in the contact force (*figure 5.18*); as a result the progress of the impactor is slowed down until it is blocked at about  $7.5\text{ seconds}$  (*figure 5.17*), when its speed becomes zero (*figure 5.16*).

The system consisting of impactor and stem then undergoes an initial force peak and is then subjected to lower contact forces and consequently begins to vibrate according to its natural pulsation. In the period of time between the two peaks, it can be seen that the force trend is very similar to the damped free vibrations of a mass-spring-damper system, where the mass is the impactor, the spring is the stem, and the damping is provided by the stem material.

It will therefore be necessary to filter the force signal, using a suitable band-stop filter, in order to eliminate the effect of these vibrations. Observing the graph in *figure 5.18*, it can be seen that there are approximately 2.3 oscillations every millisecond, which corresponds to a frequency of  $2300\text{ hertz}$ , but to be more precise, the Fourier transform of the force signal was carried out; the graph of the modulus of the transform is shown in *figure 5.19*.

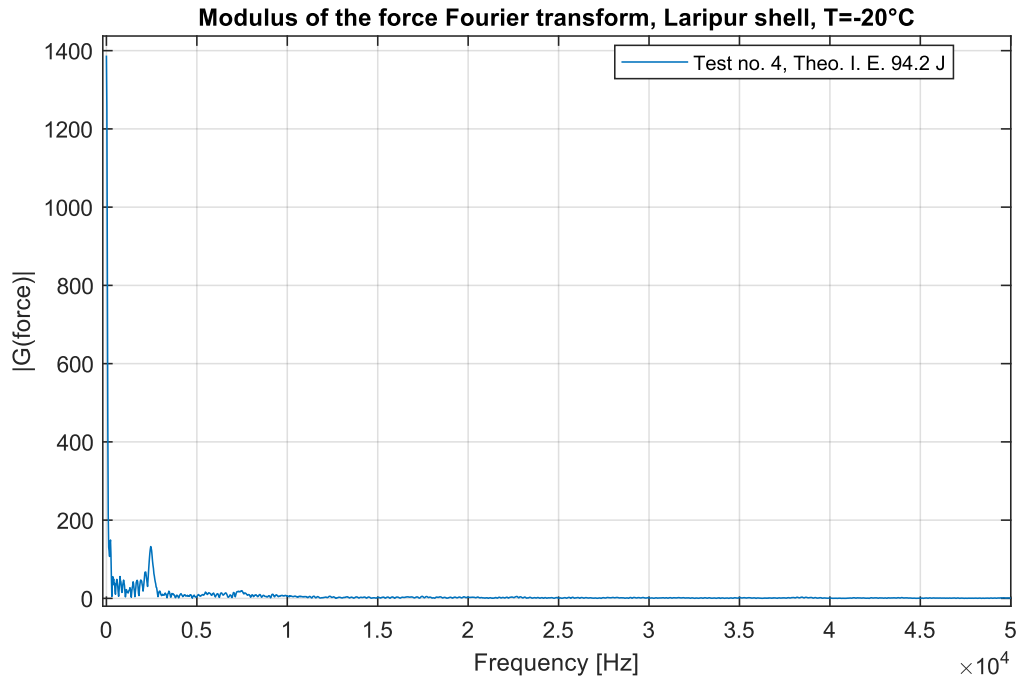


Figure 5.19: graph of the modulus of the Fourier transform of the force, for the fourth test performed on shells in Laripur

As can be seen more precisely in the zoom of *figure 5.20*, the modulus of the transform increases considerably for frequency values between 2000 and 3000 *hertz*, so this will be the frequency range to be filtered.

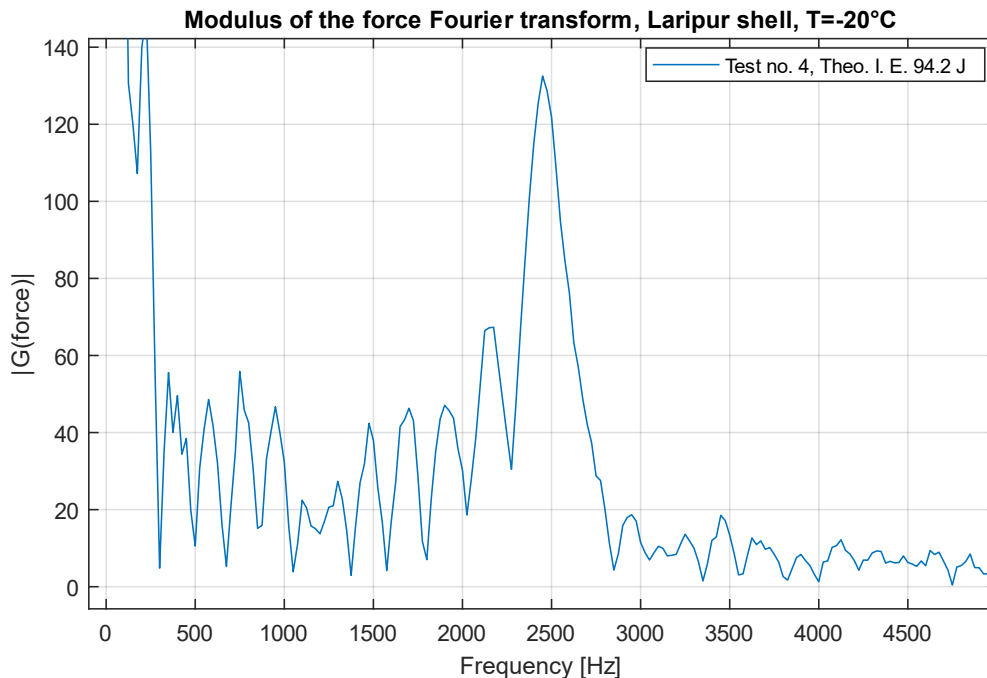


Figure 5.20: zoom of the graph of the modulus of the Fourier transform of the force, for the fourth test performed on shells in Laripur

With this indication, a band-stop filter was applied to the force signal for frequencies between 1500 and 4000 *hertz* (because the range 2000 – 3000 *Hz* was too small

for the filter to be effective), resulting in the graph and corresponding transform shown in figures 5.21 and 5.22.

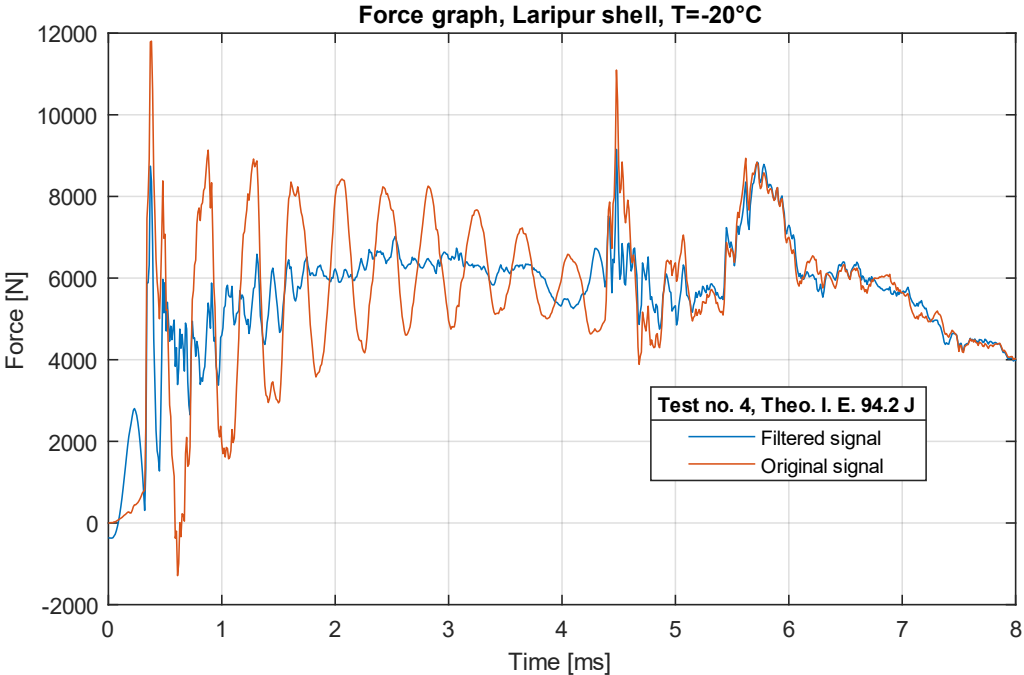


Figure 5.21: filtered force graph for the fourth test performed on shells in Laripur

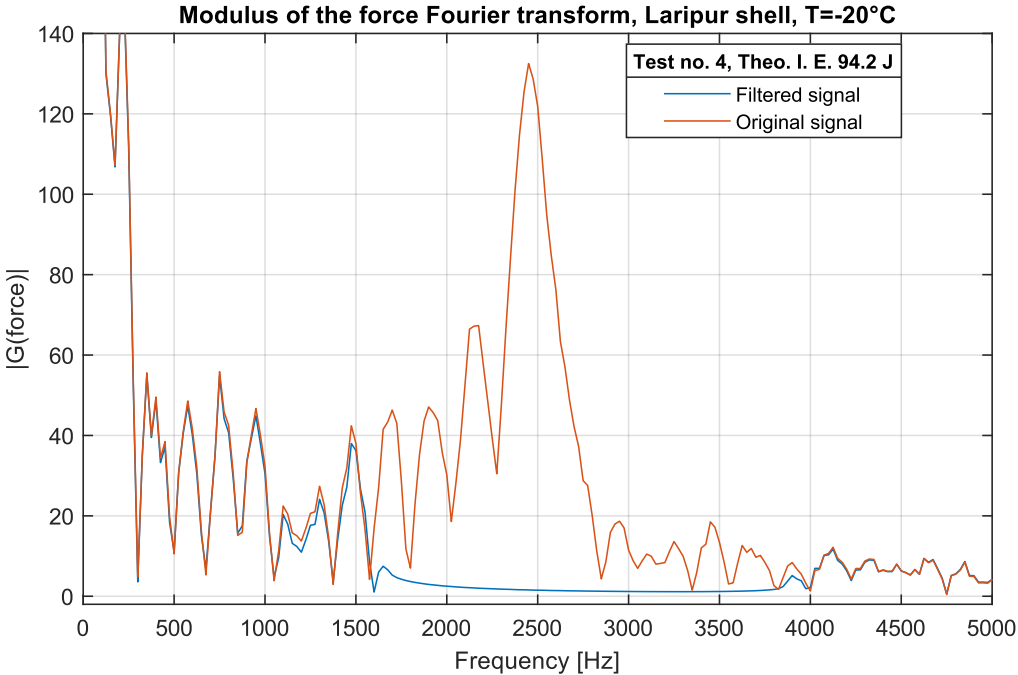


Figure 5.22: graph of the modulus of the Fourier transform of the filtered force, for the fourth test performed on shells in Laripur

After filtering the force signals in this way, the maximum values could be identified, and the results obtained for the three materials are then shown in the tables below.

Impact tests, Laripur shell, T=-20°C						
Test no.	Theo. I. E.	Failure?	Meas. I. E.	Peak Force	I. speed	Max displ.
1	79,8	no	78,0	8,184	4,34	14,13
2	99,3	yes	100,0	9,442	4,39	19,34
3	89,6	no	89,2	11,615	4,38	15,91
4	94,2	no	94,0	9,152	4,38	17,46
5	94,2	yes	94,1	10,093	4,38	55,35
6	94,2	no	92,9	12,980	4,36	16,62
	J		J	kN	m/s	mm

Table 5.5: quantities measured from impact tests performed on Laripur shells

Impact tests, Grilamid shell, T=-20°C						
Test no.	Theo. I. E.	Failure?	Meas. I. E.	Peak Force	I. speed	Max displ.
1	285,1	yes	278,5	14,520	4,46	75,47
2	187,3	no	193,3	12,280	4,43	27,12
3	236,2	yes	244,8	12,263	4,43	31,61
4	216,7	yes	218,0	11,648	4,46	66,89
5	197,1	no	202,2	13,606	4,42	28,25
6	206,9	no	214,1	14,839	4,43	30,04
	J		J	kN	m/s	mm

Table 5.6: quantities measured from impact tests performed on Grilamid shells

Impact tests, Elastollan shell, T=-20°C						
Test no.	Theo. I. E.	Failure?	Meas. I. E.	Peak Force	I. speed	Max displ.
1	128,7	no	131,1	12,099	4,42	21,05
2	148,2	no	151,2	12,881	4,42	22,29
3	187,3	no	192,8	14,939	4,43	24,44
4	236,2	no	244,0	15,919	4,43	28,05
5	285,1	no	296,2	16,233	4,43	33,95
6	/	/	/	/	/	/
	J		J	kN	m/s	mm

Table 5.7: quantities measured from impact tests performed on Elastollan shells

As can be seen from these tables, for each of the three materials, the test with the highest impact energy that did not break a shell, results in a higher peak energy than the test with the lowest impact energy that did break a shell. This is probably because, in tests where the shell does break, at some point the material collapses and therefore offers less resistance to the advancing impactor, resulting in a lower peak force. In static numerical simulations, it would thus make more sense to apply the maximum force values recorded without breaking the shells in order to search for a limiting magnitude (tension or deformation) beyond which the shell would be declared to have broken.

At the same time, the fact that the peak forces are greater in tests where there is no shell rupture may also cast some doubt on whether this is the correct quantity to impose. It may therefore make more sense to apply an imposed displacement and, in particular, the displacement obtained for the test with the highest impact energy

that did not cause a shell to break. in fact, the maximum displacements, of course, increase with increasing impact energy and are greater in tests where there is shell rupture.

As a final observation, looking at the marks left by the impactor on the shells that did not break (*figure 5.23*) and the break initiation points on the broken shells (*appendix D*), it is clear that the impactor initially strikes the apex of the toe curvature, but then, due to the deformation of the shell, slides towards the sole and puts more stress on the area below.



Figure 5.23: mark left by the impactor on the tip of the Laripur shell in test number 4

Consequently, in numerical simulations of impact we will have to take this phenomenon into account and try, if possible, to replicate it.

### 5.2.3 Conclusions

Even in the case of impact tests, shell properties normalised to their mass can be calculated. Critical specific impact energies were then calculated to assess which material makes the Markab shell more efficient for impact resistance.

$$\textit{Specific Critical I. E.} = \frac{\textit{Critical I. E.}}{\textit{Shell mass}} \quad \text{Formula (5.4)}$$

<b>Specific critical impact energies, T=-20°C</b>			
<b>Material</b>	<b>Shell mass</b>	<b>Critical I. E.</b>	<b>Specific Critical I. E.</b>
Laripur	0,637	94,2	148,0
Grilamid	0,523	≈ 211,8	≈ 404,8
Elastollan	0,636	> 285,1	> 448,3
	kg	J	J/kg

Table 5.8: Specific critical impact energies

As can be seen from *table 5.8*, by normalising the critical impact energies to the shell mass, Elastollan turns out to be the material that makes the Markab shell more efficient for tip impact resistance.





## Chapter 6: Introduction to numerical impact simulations

This chapter will then discuss the mechanical characterisation of the three materials used for the Markab shell model and then explain how static numerical simulations will be carried out; the validation of these static simulations and the transition to dynamic simulations will be the future development of this work.

### 6.1 Characterisation of polymeric materials at high strain rates and low temperatures

After performing the experimental impact tests, in order to study the constraint and loading conditions and obtain useful data to validate the numerical simulations, the next step is to characterise the mechanical properties of the materials used for the three versions of the Markab shell, under conditions similar to those occurring during the impact test and, therefore, for high deformation speeds and a material temperature of  $-20^{\circ}\text{C}$ .

#### 6.1.1 Charpy impact tests on specimens

In order to characterise materials under conditions similar to those of impact tests, an initial idea was to apply strain gauges to specimens of each material and, after leaving them in a freezer at  $-20^{\circ}\text{C}$ , extract them and subject them to a Charpy test.



Figure 6.1: machine used for Charpy impact tests

In particular, the strain gauges were to be glued to the test specimens on the side opposite the side that is hit by the Charpy hammer, in order to observe the increasing strain rate up to the ultimate strain at break, for high strain rates. The specimens used are those in the shape of a rectangular parallelepiped already used

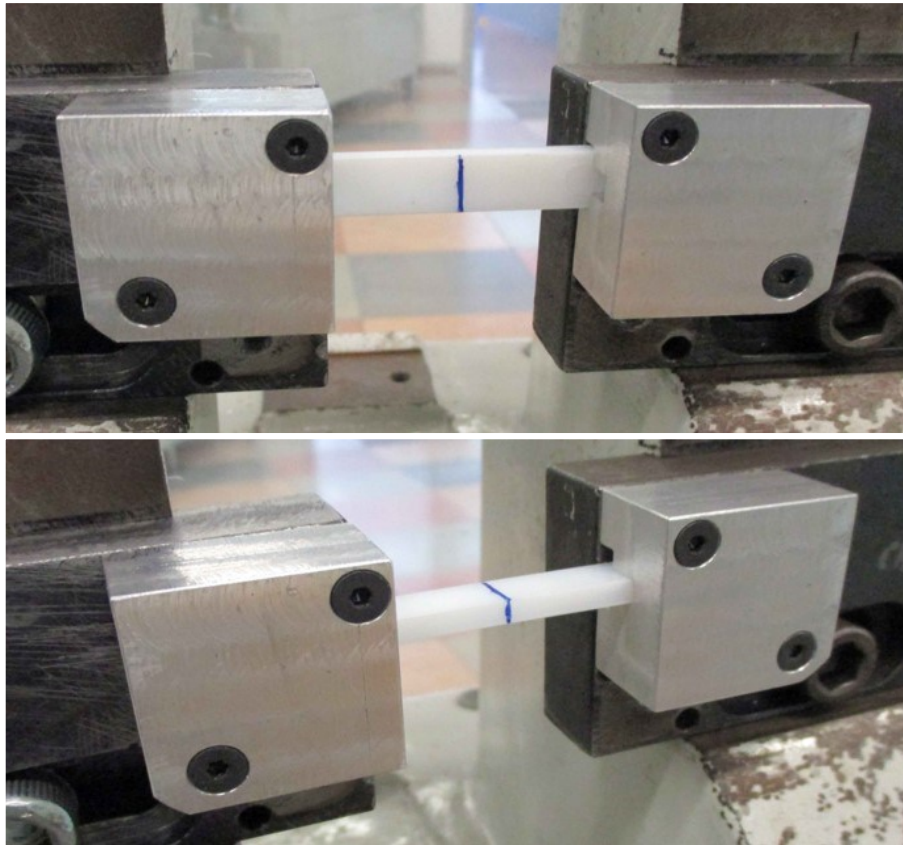
for the three-point bending tests, having a length  $l = 80 \text{ mm}$ , a width  $b = 10 \text{ mm}$  and a thickness  $h = 4 \text{ mm}$

However, as the materials are very ductile (at room temperature the tensile elongation at break is 686% for Laripur, 356% for Grilamid and 425% for Elastollan), under the test conditions specified in UNI EN ISO 179-1, the specimens at  $-20^{\circ}\text{C}$  did not break because they deformed to the point that they came out of the support plates and remained intact. We also tried to tighten the supporting plates of the test specimens as much as the width of the Charpy hammer would allow, and to hit them on both the side with a thickness of  $4 \text{ millimetres}$  and the side with a width of  $10 \text{ millimetres}$ , but in both cases we were unable to break them.



Figures 6.2-6.3: specimen plastically deformed but intact as a result of a Charpy impact test in which the hammer hit it on the  $4 \text{ millimetres}$  thick side

Observing the deformation of the test specimens, it was also hypothesised that the problem might be related to the fact that they were too loosely constrained and that the possibility of moving upwards helped them to move out of the support plates. Two plates were then screwed onto the support plates in order to keep the test specimens in the correct position throughout the test (*figures 6.4 and 6.5*).



Figures 6.4-6.5: plates to be fixed on the support plates for holding the specimens in the correct position during Charpy impact tests

However, even using the 50 joule mallet (the largest in the company's laboratory), and impacting the specimens on both sides (*figures 6.4 and 6.5*), we were unable to achieve any breakage: in all cases the specimens deformed to the point of coming out of the support plates without breaking, except in the case of the Elastollan specimens impacted on the 4 millimetre thick side, in which the specimens did not break and did not come out of the support plates, but bounced back the Charpy hammer.

Consequently, since it was necessary to study the behaviour of materials up to failure, it was decided to switch to other types of tests to try to characterise the behaviour and failure of these materials at  $-20^{\circ}\text{C}$  and at high strain rates.

### **6.1.2 Tensile tests at high strain rates**

It was therefore decided to perform tensile tests on dumbbell specimens of the three polymeric materials, imposing the maximum strain rate of the machine available in the company.



Figure 6.6: tensile tests at high strain rates in the company's traction machine

The procedure followed is set out below:

- The dumbbell specimens were placed in the freezer at  $-20^{\circ}\text{C}$  approximately twenty-four hours before the test.
- The tensile machine was set to perform the tests at its maximum strain rate, which is  $1500\text{ mm}/\text{min}$ ;
- The specimen to be tested is taken out of the freezer and quickly mounted on the grips of the tensile machine.
- The sensor arm extensometer is positioned, and the test is started.
- Once the specimen breaks, the test is finished and the data on the strain measured by the extensometer and the force measured by the load cell are exported to a file

These data are then processed using a Matlab script and the stress-strain curves obtained for each of the three materials are shown in *figure 6.7*.

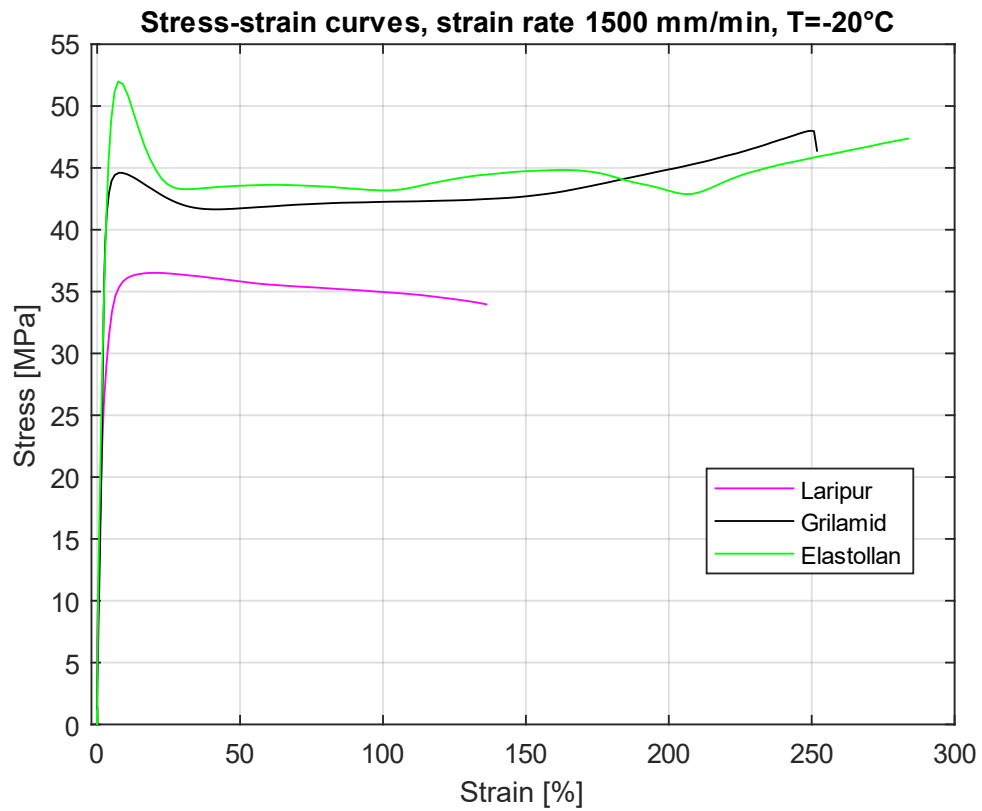


Figure 6.7: stress-strain curves obtained for the three material specimens at -20°C and a strain rate of 1500 mm/min

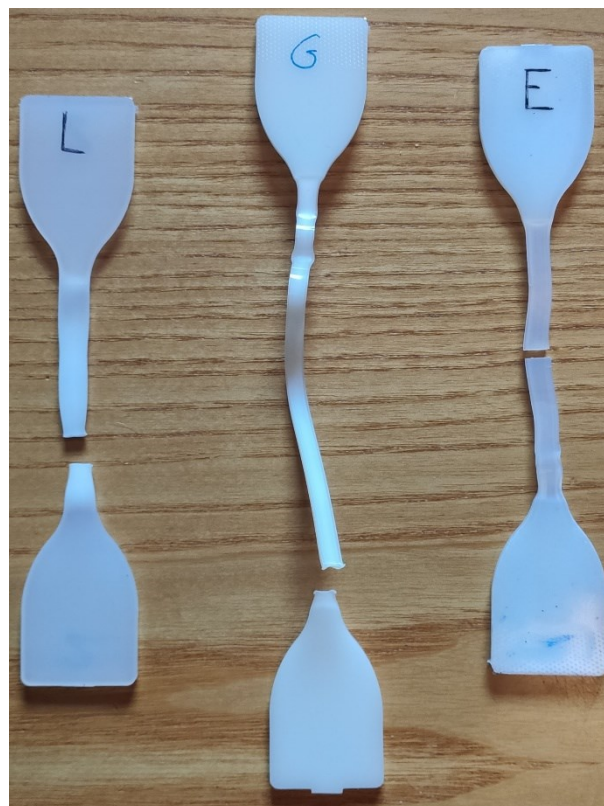


Figure 6.8: broken specimens at the end of the tensile test at a strain rate of 1500 mm/min and T=-20°C

It will be necessary to understand whether this deformation rate is sufficient to characterise the materials because, as can be seen from the tensile curves (*figure 6.7*) and photos of the broken specimens (*figure 6.8*), in these tests the materials have yielded and undergone plastic deformations, whereas in the impact tests on the shells, the breakage at the tip seems to be brittle (*appendix D*).

## 6.2 Static impact simulations

The next step would then be to carry out static numerical simulations by imposing the maximum force or displacement of the impactor measured by the instrumented stem in the experimental tests and attempting to define a limiting magnitude (peak stress or strain) beyond which the shell of a given material breaks.

### 6.2.1 Assembly management on Rhinoceros

In this simulation, having to tilt the shell by  $65^\circ$ , it is more convenient to create the assembly of the various elements directly in Rhinoceros. Consequently, the CAD models of the shell, front insert and soles are imported into a single file and, after selecting all four, an assembly is created with the 'Group' command. At this point, it is possible to rotate this assembly by  $65^\circ$  to bring it into the same position as in the real test, in order to make it easier to model the impactor and the subsequent application of the load (force or displacement), which in this way will have a vertical direction.

The point on the hull was then identified, at the apex of the curvature and halfway along the width of its tip, where the impactor theoretically strikes the shell. From here, the semi-sphere of radius 26 millimetres was constructed to simulate the end portion of the impactor that will be used to apply the load.

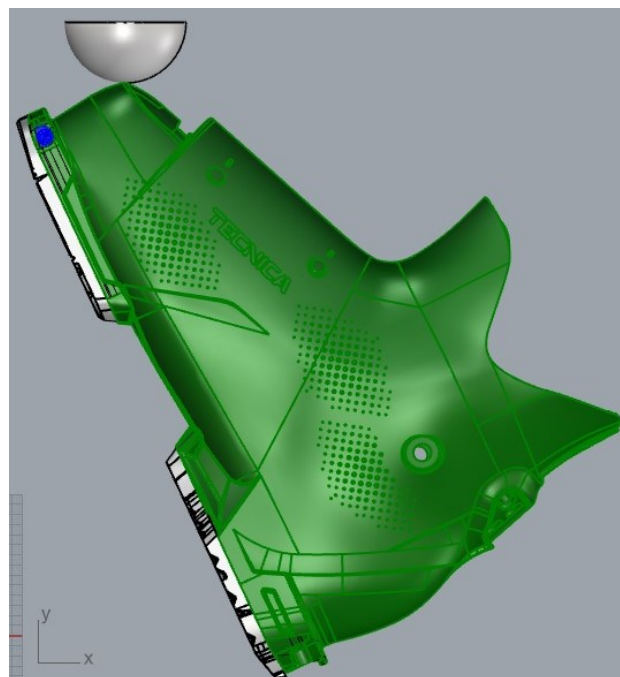


Figure 6.9: shell assembly and impactor positioning in Rhinoceros

### 6.2.2 Static impact simulations on Ansys Workbench

At this point, it will be necessary to:

- Set the material properties of the shell and soles at  $-20^{\circ}\text{C}$ , making the appropriate assessments as to whether it is appropriate to import the curves obtained from the tensile tests at strain rates of  $1500\text{ mm/min}$  or whether it is more appropriate to model the material as linear elastic until failure (in the latter case, it must be defined for what level of tension or deformation failure occurs).
- Import the CAD model of the assembly made in Rhinoceros, including the impactor, and assign each element its material (the impactor is made of steel).
- Decide how to handle contacts: those between the soles and the shell and between the front insert and the shell can be set as 'Bonded', but the type of contact between the impactor and the shell tip must also be defined.
- Choose a size and type of mesh elements: the idea was to continue with tetrahedral elements and initially make a coarse mesh and then have Ansys automatically refine it using the adaptive refinement of the mesh.
- Set constraints: at the heel a 'Fixed Support' could be imposed, while on the lower surfaces of the soles a support with a certain coefficient of friction (or without friction, since the shell being at  $-20^{\circ}\text{C}$  has a thin layer of moisture that makes it very slippery) could be applied; On the tip, we need to consider how to replicate the constraint formed by the clamping because in fact it is not very binding, as the front of the shell lowers due to the deformation caused by the impactor impact.
- Setting the load: It must be decided whether to apply the highest measured value, on a shell that has not broken, of peak force or peak downward displacement. In both cases, it will be necessary to apply this load via the modelled impactor and it will be necessary to prevent the impactor from moving in other than vertical directions via a constraint.
- In the analysis settings, it should be considered whether or not to activate the option for 'Large Deflections'.
- In the solutions, it will be possible to determine the maximum stress and the maximum strain, and it will be necessary to decide which of the two quantities to use as a limit reference to define whether the shell has broken or not.

Then simulating an impact test for a critical impact energy value will result in a limiting magnitude (a limiting stress or deformation). If the geometry of the shell is modified and increasing impact energies are simulated, the shell will be considered as broken when the defined limit magnitude is exceeded.

### 6.2.2 Conclusions and future developments of the work

Once these static impact simulations have been carried out, it will be possible to assess whether or not the proposed method for defining shell rupture, based on the application of a static load and the definition of a limit size beyond which rupture occurs, is effective.

In any case, it will probably be necessary to move on to dynamic impact simulations using a different software than Ansys, where the initial impact velocity can be applied to the impactor and a polymeric material criterion can be used to numerically define whether or not rupture has occurred. The results of these simulations will then have to be validated on the basis of experimental tests, and once realistic numerical impact simulations can be carried out, it will be possible to develop the process of topological optimisation of a shell shown in the diagram in Figure 6.10.

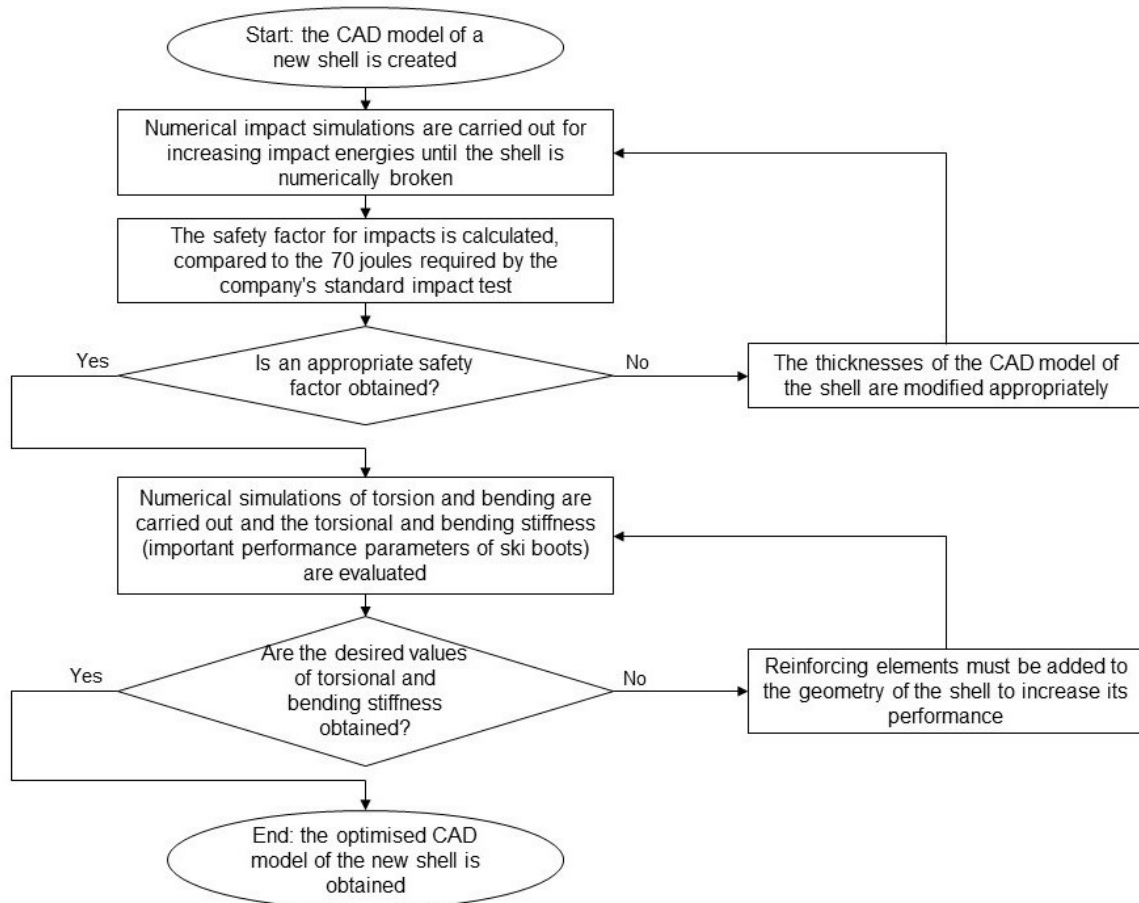


Figure 6.10: diagram of the topological optimisation of a shell, based on numerical simulations of the shell's behaviour in torsion, bending and impact resistance

Finally, moulds must be made for injection moulding some prototypes of the new model, in order to experimentally verify that the impact resistance and torsional and flexural stiffnesses are as desired.







## Appendix A: CAD drawings of torsion test bench grips

### A.1 Grip simulating the anterior ski touring binding

Figure A.1 shows the CAD model of the c-beam to be fixed to the torsion machine head.

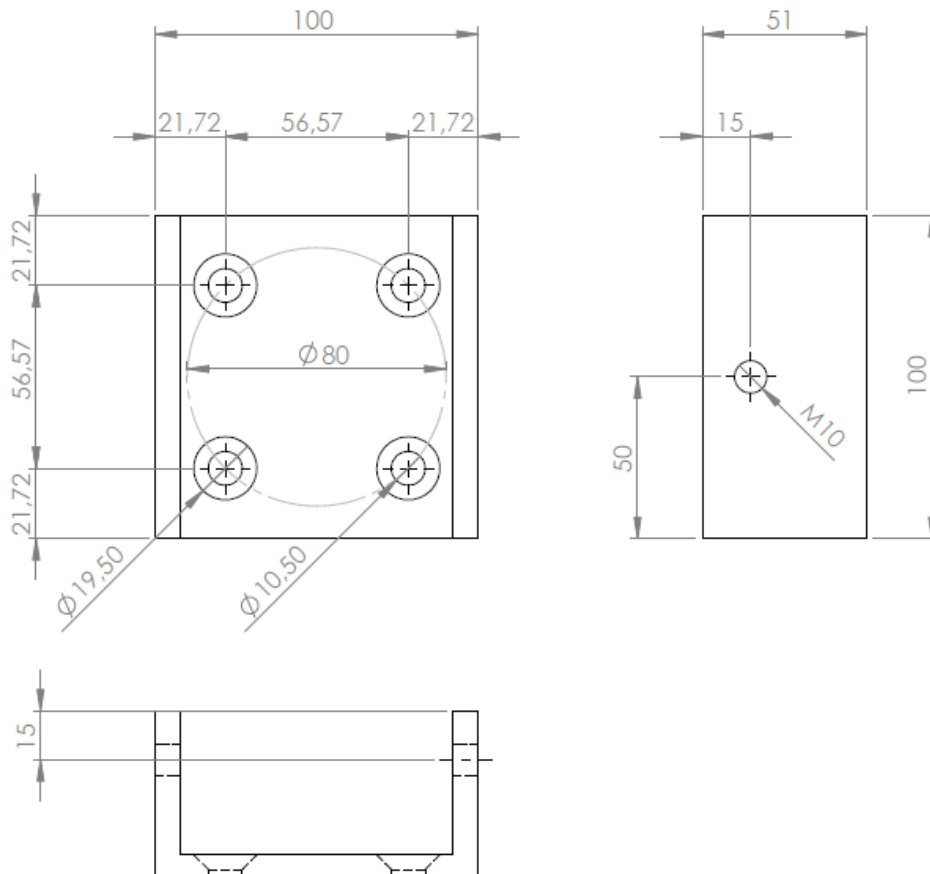


Figure A.1: CAD model of the c-beam

Figure A.2 shows the CAD model of the two screws simulating anterior ski touring binding pins.

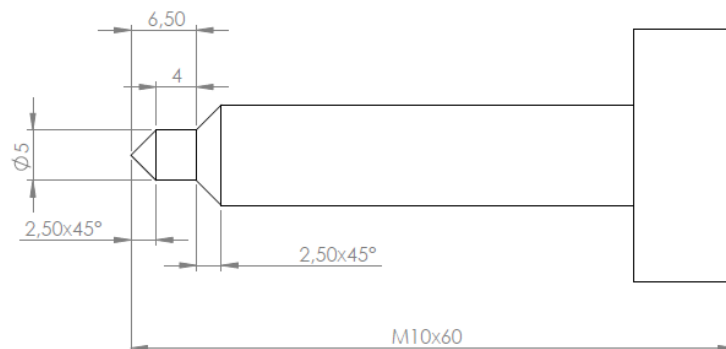


Figure A.2: CAD model of the two screws simulating anterior ski touring binding pins

## A.2 Grip simulating the posterior downhill skiing binding

Figure A.3 shows the CAD model of the c-beam on which the heel of the shell rests.

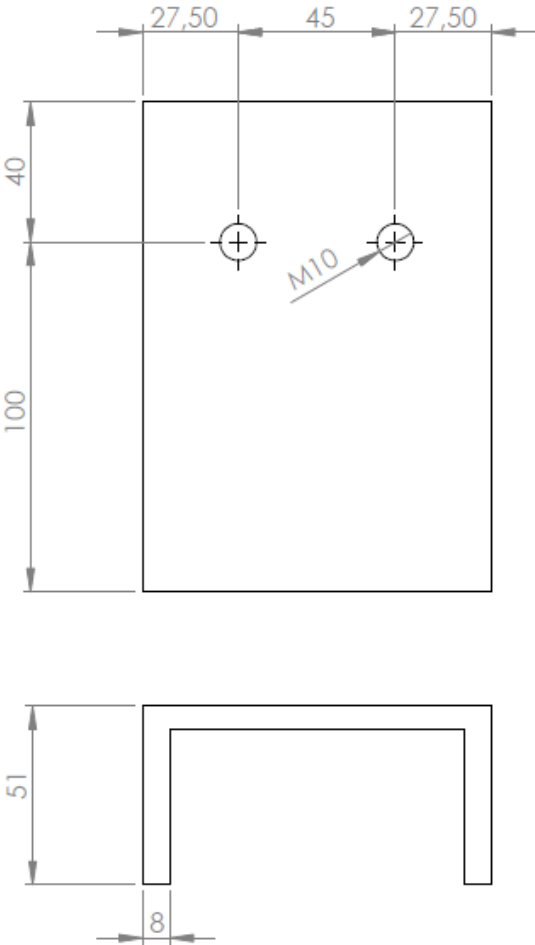


Figure A.3: CAD model of the c-beam on which the heel of the shell rests

Figure A.4 shows the CAD model of the vertical plate to be fixed to the torsion machine head with three screws.

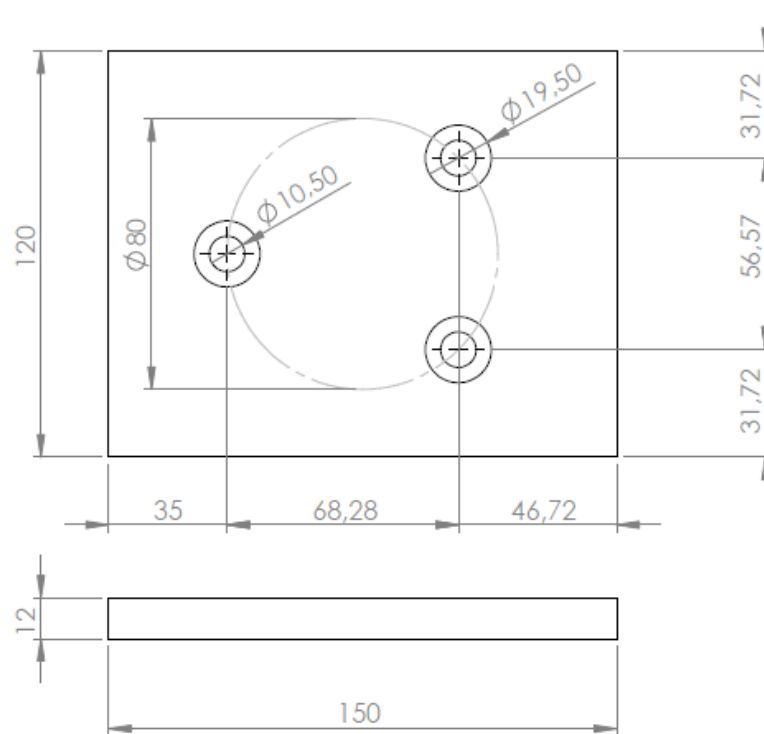


Figure A.4: CAD model of the vertical plate to be fixed to the torsion machine head  
 The c-section beam was welded to the vertical plate with the positioning shown in figure A.5.

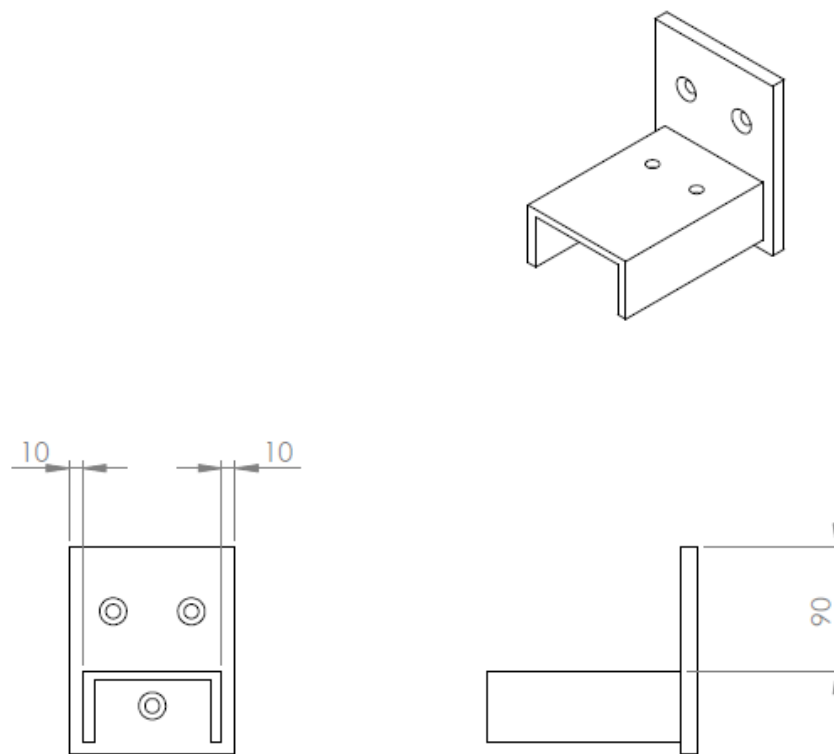


Figure A.5: CAD model of the c-beam welding with vertical plate

Figure A.6 shows the CAD model of the plate designed to fasten the shell heel, simulating the downhill ski binding required by the ISO 23223 standard.

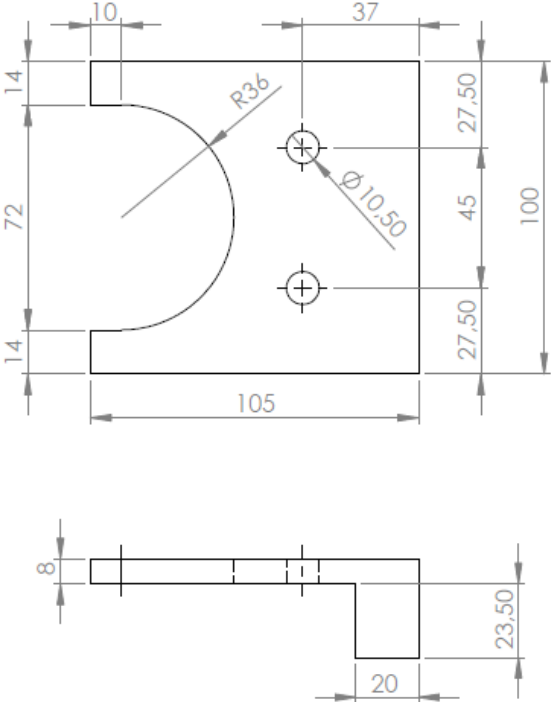


Figure A.6: CAD model of plate designed to fasten the shell heel

### A.3 Grip simulating the posterior ski touring binding

Figure A.7 shows the CAD model of the L-beam to be fixed to the welded structure of figure A.5.

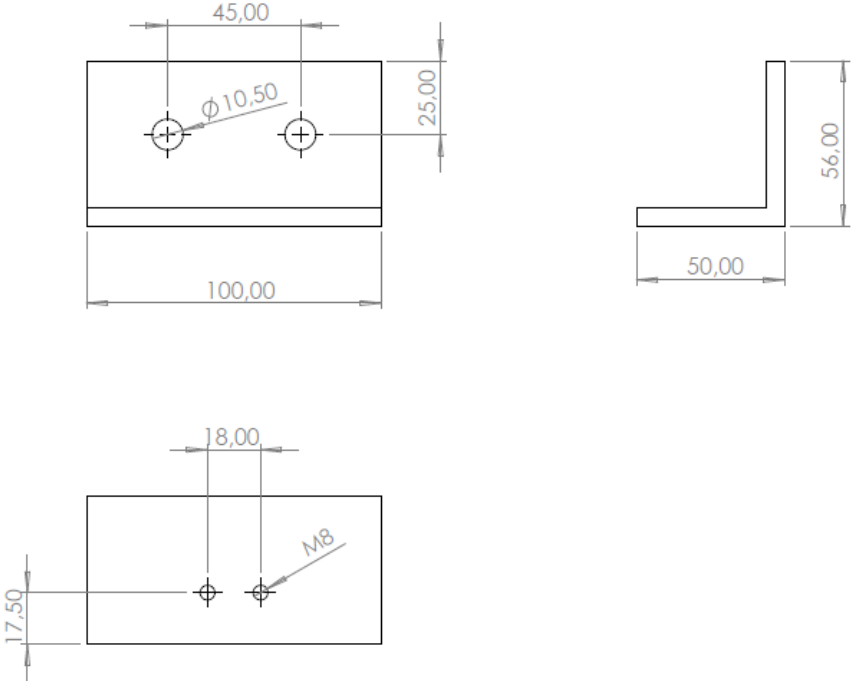


Figure A.7: CAD model of the L-beam to be fixed to the welded structure of figure A.5.

Figure A.8 shows the CAD model of the two screws simulating posterior ski touring binding pins.

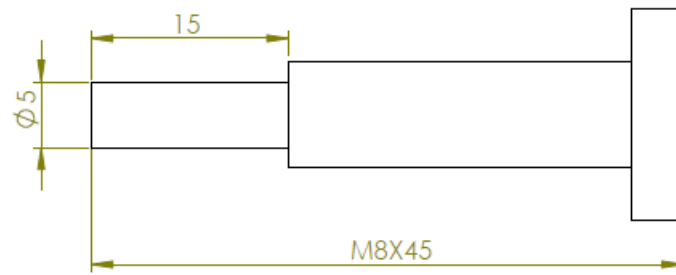


Figure A.8: CAD model of the two screws simulating posterior ski touring binding pins





## Appendix B: Scripts used for data analysis with Matlab

### B.1 Script for data analysis of torsion bench tests

Below is reported the script used to analyse the data contained in the DAT file produced as output by the torsion machine at the end of each test:

```
-----  
%% Section 1: Clearing the environment  
clc  
clearvars  
close all  
  
%% Section 2: Set up the Import Options and import the data  
% Creates the object with the number of variables specified in numVars.  
opts=delimitedTextImportOptions("NumVariables",3);  
  
% Specify range and delimiter  
opts.Delimiter="\t";  
  
% Specify column names and types  
opts.VariableNames = ["Time_s", "Angle_deg", "Torque_Nm"];  
opts.VariableTypes = ["double", "double", "double"];  
  
% Specify file level properties  
opts.ImportErrorRule = "omitrow";  
opts.MissingRule = "omitrow";  
opts.ExtraColumnsRule = "ignore";  
opts.EmptyLineRule = "read";  
  
%Import the data from dat file  
datatable=readtable("la_hyb_5.dat",opts);  
  
%transition from a table to a matrix  
datamatrix=datatable{:,:};  
  
%% Section 3: Creating an average angle vector  
% Creating a vector of angles with all relevant data  
% Since the first cycle could be one of adjustment, we start taking data from  
the second  
Angle=datamatrix(102:1901,2);  
  
% In this case, there are no errors in the txt file so that all relevant data  
can be selected in a single operation  
  
% Correction of angle vector  
m=mean(Angle);  
Angle_corr=Angle-m;  
  
% Creation of an empty vector  
Angle_summ=[];  
  
% Creating a summation vector  
a=(length(Angle_corr)/100)-1;  
for i=1:100
```

```

    summ=0;
    for j=0:a
        summ=summ+Angle_corr(i+j*100,1);
    end
    Angle_summ(i,1)=summ;
end

% Operation only useful for closing hysteresis cycles in graphs
Angle_summ(101,1)=Angle_summ(1,1);

% Creation of an average angle vector
c=length(Angle)/100;
Angle_mean=Angle_summ/c;

%% Section 4: Creating an average torque vector
% Creating a torque vector with all relevant data
Torque=datamatrix(102:1901,3);

% In this case, there are no errors in the txt file so that all relevant data
can be selected in a single operation

% Creation of an empty vector
Torque_summ=[];

% Creating a summation vector
for i=1:100
    summ=0;
    for j=0:a
        summ=summ+Torque(i+j*100,1);
    end
    Torque_summ(i,1)=summ;
end

% Operation only useful for closing hysteresis cycles in graphs
Torque_summ(101,1)=Torque_summ(1,1);

% Creating an average torque vector
Torque_mean=Torque_summ/c;

%% Section 5: Hysteresis cycles graph
% Graph creation
figure(1)
plot(Angle_corr,Torque)
xlabel('Angle [deg]')
ylabel('Torque [Nm]')
title('Hysteresis cycles, ambient temperature')
grid on
legend('Laripur 5° rotation','Location','best')
title(legend,'Hybrid ski binding configuration')

%% Section 6: Graph of mean hysteresis cycle and regression line
%Linear regression of the mean hysteresis cycle
X=[ones(length(Angle_mean),1) Angle_mean];
b=X\Torque_mean;
Slope=X*b;

% Graph creation
figure(2)

```



repeated twice. In fact, in this case, about 1,3 second of data acquisition was lost and thus 13/10 of a hysteresis cycle is missing.

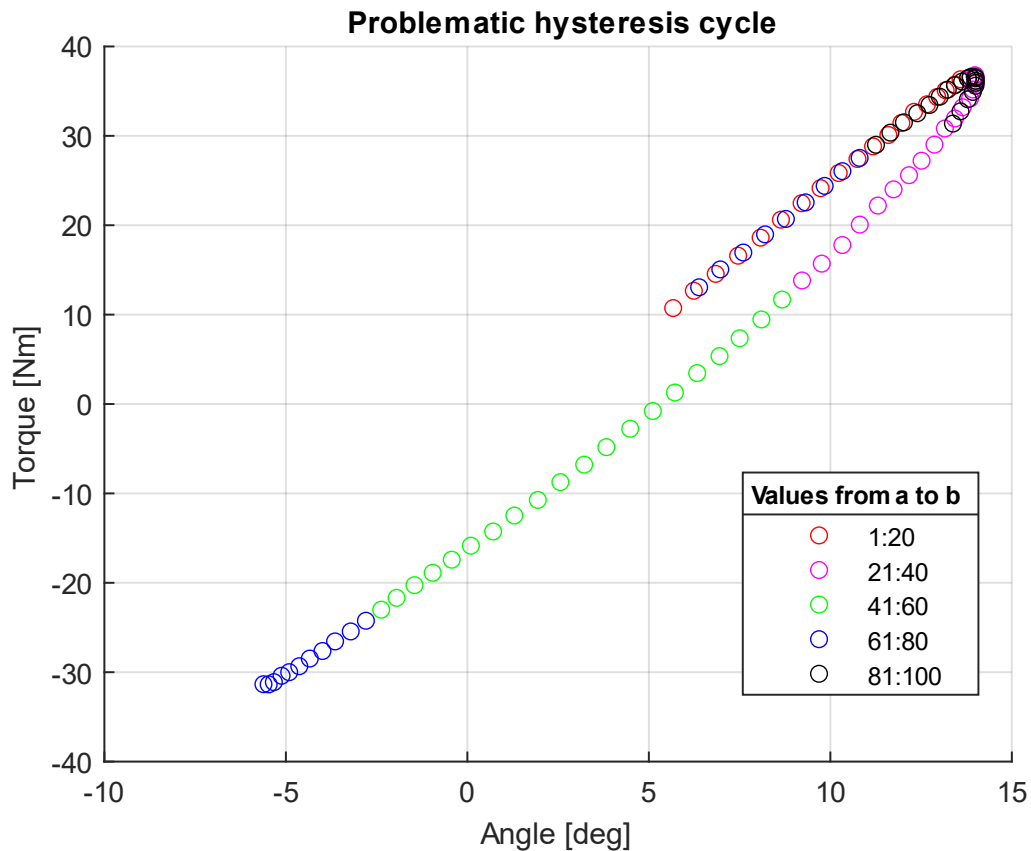


Figure B.2: as can be seen in the range of blue dots, we move from the lower to the upper part of the hysteresis cycle

This is a problem because the average hysteresis cycle is calculated and these missing data dephase the cycles with the risk of producing wrong results. Consequently, before executing the script, it is necessary to check that there are no errors in the DAT file and, if there are, it will be necessary to modify it appropriately in order to consider only complete hysteresis cycles. For example, in the case of *figure B.1*, when selecting the relevant data, the script was modified as follows:

[...]

```

%%% Creating an average angle vector
% Creating a vector of angles with all relevant data
% Since the first cycle could be one of adjustment, we start taking data from
the second
Angle=datamatrix(104:703,2);

```

```

% Addition of other relevant values in case of errors in the machine output
file
Angle(601:1600,1)=datamatrix(774:1773,2);

```

[...]

```

%% Creating an average torque vector
% Creating a torque vector with all relevant data
Torque=datamatrix(104:703,3);

% Addition of other relevant values in case of errors in the machine output
file
Torque(601:1600,1)=datamatrix(774:1773,3);

[...]

```

---

## B.2 Script for impact test data analysis

In order to analyse the data contained in the TXT file generated by the Fractovis drop tower computer, a Matlab script was written in the following way:

- The first section serves to clean the environment: the command used delete all text from the 'Command Window', remove all variables from the 'Workspace' and close all open figure windows.
- Section two is used to import the data from the table in the TXT file into a matrix and, thus, to create a vector with all the data for each measured quantity (time, force, energy, speed and displacement).
- Section three is used to create graphs of each of the measured quantities from the instrumented stem over time.
- Section four is used to perform a frequency analysis of the force signal: the Fourier transform is performed, and the modulus of the transform is plotted in order to understand the natural pulsation of the system consisting of impactor and stem.
- Section five is used to filter the force signal in order to eliminate the disturbance related to the damped free vibrations of the impactor-stem system and to create the filtered force signal graph.
- Section six is used to output on the 'Command Window' the maximum values of force, velocity, energy and displacement obtained in the graphs.

The script used is given below:

```

%% Section 1: Clearing the environment
clc
clearvars
close all

%% Section 2: Importing data and creating vectors for each measured quantity
% The data in the txt file are imported into a matrix
matrix=readmatrix("e_5_285.txt");

% The matrix is transposed to have the data organised in columns

```

```

data=transpose(matrix);

% Creation of time, force, energy,velocity and displacement vectors
time=data(:,5); %ms
force=data(:,1); %N
energy=data(:,2); %J
speed=data(:,3); %m/s
displacement=data(:,4); %mm

%% Section 3: Graphs of measured quantities from the instrumented stem
% Creation of the force over time graph
figure(1)
plot(time,force)
xlabel('Time [ms]')
ylabel('Force [N]')
xlim([0 10])
title('Force graph, Laripur shell, T=-20°C')
grid on
legend('Test no. 4, Theo. I. E. 94.2 J','Location','best')

% Creation of energy graph over time
figure(2)
plot(time,energy)
xlabel('Time [ms]')
ylabel('Energy [J]')
title('Energy graph, Laripur shell, T=-20°C')
grid on
legend('Test no. 4, Theo. I. E. 94.2 J','Location','best')

% Creation of velocity graph over time
figure(3)
plot(time,speed)
xlabel('Time [ms]')
ylabel('Speed [m/s]')
xlim([0 7.5])
title('Speed graph, Laripur shell, T=-20°C')
grid on
legend('Test no. 4, Theo. I. E. 94.2 J','Location','best')

% Creation of displacement graph over time
figure(4)
plot(time,displacement)
xlabel('Time [ms]')
ylabel('Displacement [mm]')
title('Displacement graph, Laripur shell, T=-20°C')
grid on
legend('Test no. 4, Theo. I. E. 94.2 J','Location','best')

%% Section 4: Analysis of force development over time
% Time vector
t=time/1000; %s
% Sampling frequency
fs=1/(t(2)-t(1)); %Hz
% Sampling interval
dT=1/fs; %s
% Number of samples
N=length(force);
% Time window

```

```

T=dT*N;
% Frequency resolution
f1=1/T;
% Fast Fourier transform
G=fft(force)/N;
% Frequency vector
f=[0:f1:fs-f1]; %Hz

% Fourier transform graph
figure(5)
plot(f(1,1:N/2+1),abs(G(1:N/2+1,1)))
grid on
xlabel('Frequency [Hz]')
ylabel('|G(force)|')
xlim([-0.2e3 fs/2])
ylim([-20 max(abs(G(1:N/2+1,1)))+50])
title('Modulus of the force Fourier transform, Laripur shell, T=-20°C')
legend('Test no. 4, Theo. I. E. 94.2 J','Location','best')

%% Section 5: Filtering of the force vector
% Definition of the frequency range to be filtered
fpass=[1500,4000];

% Force filtering with a band-stop filter
f_f=bandstop(force,fpass,fs);

% Filtered force diagram
figure(6)
plot(time,f_f)
xlabel('Time [ms]')
ylabel('Force [N]')
xlim([0 8])
title('Force graph, Laripur shell, T=-20°C')
grid on
hold on
plot(time,force)
legend('Filtered signal','Original signal','Location','best')
title(legend,'Test no. 4, Theo. I. E. 94.2 J')

% Fourier transform of the filtered force
G_f=fft(f_f)/N;

% Graph of the Fourier transform of the filtered force
figure(7)
plot(f(1,1:N/2+1),abs(G_f(1:N/2+1,1)))
grid on
xlabel('Frequency [Hz]')
ylabel('|G(force)|')
xlim([0 5000])
ylim([-2 140])
title('Modulus of the force Fourier transform, Laripur shell, T=-20°C')
hold on
plot(f(1,1:N/2+1),abs(G(1:N/2+1,1)))
legend('Filtered signal','Original signal','Location','best')
title(legend,'Test no. 4, Theo. I. E. 94.2 J')

%% Section 6: Output in the command window
% Peak force

```

```
Peak_f=max(f_f)/1000;
formatSpec='The maximum value of force is %5.3f kN \n';
fprintf(formatSpec,Peak_f);

% Peak speed
Peak_s=max(speed);
formatSpec='The maximum value of speed is %4.3f m/s \n';
fprintf(formatSpec,Peak_s);

% Peak energy
Peak_e=max(energy);
formatSpec='The maximum value of energy is %5.3f J \n';
fprintf(formatSpec,Peak_e);

% Peak energy
Peak_d=max(displacement);
formatSpec='The maximum value of displacement is %5.3f mm \n';
fprintf(formatSpec,Peak_d);
```

---



## Appendix C: Influence of the steel front insert in the torsional stiffness of the shell obtained from numerical simulations

The first numerical simulation had been performed using the CAD model obtained at the end of the *section 2.2.3*, in which the shell was a single element material and the front pin seats had simply been introduced. The analysis was set up in the same way as those performed in *subchapter 4.1*, with a few differences:

- In this case there is a single body, which is assigned Laripur ( $E = 340 \text{ MPa}$ ,  $\nu = 0.33$ ) as material, and consequently there will be no contact between various part to handle.
- In the definition of the remote point 'Anterior binding' the same faces will be selected as the front pin seats, only in this case they are made of polymeric material. Precisely for this reason in the 'Definition' menu of the remote point 'Rigid' will be chosen as 'Behaviour', in order to make the analysis more adherent to reality, where the insert seats are made of steel.

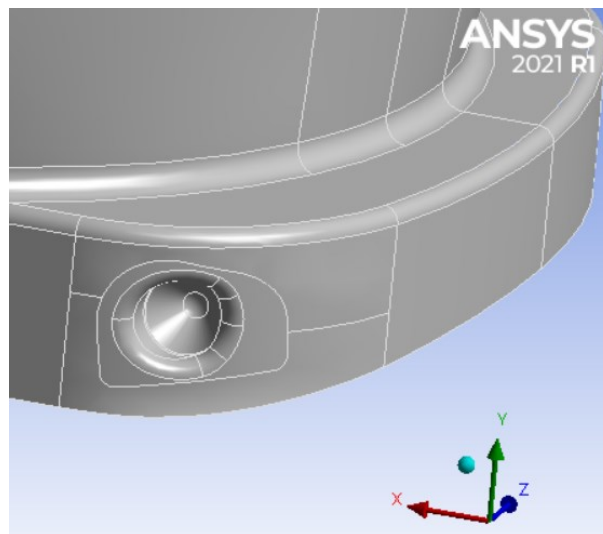


Figure C.1: zoom of the shell tip; it can be seen that in this case the model is a single body by the fact that the pin seats are the same colour as the rest of the shell

As can be seen in *table C.1*, the FEM simulation of the assembly results in a torsional stiffness of  $2.915 \text{ Nm/deg}$ , while that of the single body gives as output a torsional stiffness of  $2.680 \text{ Nm/deg}$ ; since the difference between the two stiffnesses is 8.1%, the presence of the steel insert has been considered relevant and for this reason in *chapter 4* it has been included as an additional element of the assembly.

$$Pct. variation = \frac{k_{assembly} - k_{single body}}{k_{assembly}} \cdot 100 \quad \text{Formula (C.1)}$$

<b>Comparison of FEM models of the Laripur shell, T=23°C</b>				
<b>Model</b>	<b>Rotation</b>	<b>Moment react</b>	<b>Torsional stiff</b>	<b>Pct variation</b>
Single body	5	13,398	2,680	
Assembly	5	14,574	2,915	8,1%
	deg	Nm	Nm/deg	

Table C.1: influence of the steel front insert in the torsional stiffness of the Laripur shell obtained from numerical simulations

## Appendix D: photos of shells broken during impact tests

Below are photos of shells broken during impact tests.



Figure D.1: Laripur shell broken during test number 2, performed with an impact energy of *99.3 joules*



Figure D.2: Laripur shell broken during test number 5, performed with an impact energy of *94.2 joules*



Figure D.3: Grilamid shell broken during test number 1, performed with an impact energy of 285.1 *joules*



Figure D.4: Grilamid shell broken during test number 3, performed with an impact energy of 236.2 *joules*



Figure D.5: Grilamid shell broken during test number 4, performed with an impact energy of 216.7 joules



## Bibliografia

- [1] <https://www.tecnicagroup.com>
- [2] [https://it.wikipedia.org/wiki/STL\\_\(formato\\_di\\_file\)](https://it.wikipedia.org/wiki/STL_(formato_di_file))
- [3] [https://en.wikipedia.org/wiki/STL\\_\(file\\_format\)](https://en.wikipedia.org/wiki/STL_(file_format))
- [4] <https://docs.mcneel.com/rhino/6/help/en-us/commands/showedges.htm>
- [5] <https://docs.mcneel.com/rhino/7/mac/help/en-us/commands/networksrf.htm>
- [6] <https://docs.mcneel.com/rhino/7/help/en-us/commands/extractisocurve.htm>
- [7] <https://docs.mcneel.com/rhino/7/help/en-us/commands/joinedge.htm>
- [8] <https://docs.mcneel.com/rhino/7/help/en-us/commands/splitedge.htm>
- [9] <https://www.blizzard-tecnica.com/it/it/cas-alpine>
- [10] <https://www.mechead.com/what-is-large-deflection-in-ansys/>
- [11] <https://www.blizzard-tecnica.com/global/en/cas-alpine>
- [12] ISO 23223
- [13] UNI EN ISO 178
- [14] UNI EN ISO 179-1